Cytoskeletal dynamics in confined cell migration: experiment and modelling

Sophia Anna Schaffer

München 2021

Cytoskeletal dynamics in confined cell migration: experiment and modelling

Sophia Anna Schaffer

Dissertation
at the Faculty of Physics
at the Ludwig-Maximilians-Universität
Munich

handed in by
Sophia Anna Schaffer
from Eggenfelden

Munich, June 18th 2021

First Referée: Prof. Dr. Joachim Rädler
Second Referée: Prof. Dr. Erwin Frey
Day of Oral Exam: July 26th 2021

Zytoskelettdynamik in räumlich begrenzter Zellmigration: Experiment und Modellierung

Sophia Anna Schaffer

Dissertation
an der Fakultät für Physik
der Ludwig-Maximilians-Universität
München

vorgelegt von
Sophia Anna Schaffer
aus Eggenfelden

München, den 18. Juni 2021

Erstgutachter: Prof. Dr. Joachim Rädler
Zweitgutachter: Prof. Dr. Erwin Frey
Tag der mündlichen Prüfung: 26. Juli 2021

Zusammenfassung

Der Migration von Zellen kommt eine Schlüsselrolle in vielen physiologischen Kontexten wie Embryogenese, Immunreaktion und Metastasenbildung zu. Trotz der intensiven Forschung der letzten Jahrzehnte haben Krebs-assoziierte Erkrankungen noch immer einen wesentlichen Anteil an Todesfällen in den Industrienationen, was mitunter auf die äußerst vielfältigen Ausprägungen des Krankheitsverlaufs einer Krebserkrankung zurückzuführen ist. Um in diesen Prozess mit spezifischen Therapien eingreifen zu können, bedarf es eines vollständigen Verständnisses der verschiedenen Interaktionsnetzwerke einer Zelle mit ihrer Umgebung. In der vorliegenden Arbeit wurden mikrostrukturierte Oberflächen verwendet, um Zellmigration auf standardisierte, zelladhäsiven Strukturen zu beschränken, die parallelisierte, reproduzierbare Experimente ermöglichen. Insbesondere wurden verschiedene Geometrien konstruiert, um unterschiedliches Zellverhalten auszulösen und die resultierende Dynamik des Zytoskeletts zu beobachten. Die Abstraktion dieser Bewegung auf quantitative Observablen ermöglichte die Anpassung theoretischer Modelle und den Vergleich mit denselben.

In einem ersten Projekt wurde das Zellverhalten in Streifen verschiedener Länge und Enden unterschiedlicher Krümmung untersucht. Für alle untersuchten Streifenlängen und -krümmungen konnte eine einheitliche Umdrehzeit festgestellt werden. Diese Dauer, in der die Zelle erst depolarisiert um dann stochastisch in die Gegenrichtung zu polarisieren, wurde zu etwa 100 Minuten bestimmt. Dieses allgemeine Verhalten konnte von einem zellulären Potts Modell reproduziert werden.

Um Zellmigration auf ein Minimalmodell zu abstrahieren, wurde in einem zweiten Projekt eine Methode etabliert die Parameter eines zellulären Potts Modells auf systematische Weise an reales Zellverhalten anzupassen. Hierfür wurden geometrische Mikrostrukturen verwendet, die charakteristische Formen der Zellbewegung auslösen. Die daraus erfassten Observablen wurden eins zu eins in Verbindungen mit den Parametern des Modells gesetzt. Das auf diese Weise vollständig angepasste Modell konnte auf quantitativer Ebene alle zuvor verwendeten Geometrien reproduzieren und in qualitativer Übereinstimmung das Zellverhalten auf neuen Geometrien prognostizieren.

Um Zellpersistenz und räumliches Gedächtnis zu quantifizieren, wurden in einem weiteren Projekt Zellen auf Labyrinthe beschränkt. Der Vergleich mit verschiedenen Erinnerungsmodellen zeigte, dass ein Modell, das verstärkende Rückkopplung und ein Verblassen der Erinnerung mit der Zeit berücksichtigt, die höchste Übereinstimmung erzielte.

Ein bereits etablierter Aufbau wurde verwendet, um den Einfluss verschiedener Zellsignalmoleküle auf die Interaktion zweier Zellen genauer zu untersuchen. Das Blockieren der E-Cadherine führte zu invasiverem Verhalten, charakterisiert durch vermindertes Zurückziehen der Zellen bei Kontakt und einen beschleunigenden Reibungsterm.

Zuletzt wurde die kollektive Migration von Zellen durch Kanäle mit Verengung betrachtet. Ein charakteristisches Geschwindigkeitsprofil mit verminderten Geschwindig-

keiten vor der Engstelle entwickelte sich mit fortschreitender Zellfront, was auf sogenanntes Zell-jamming zurückgeführt wurde. Hier ergab der Vergleich mit einem zellulären Potts Modell allerdings ausgeprägte Verhaltensdifferenzen.

Insgesamt trägt diese Arbeit zu einem besseren Verständnis der Zytoskelettdynamiken der Zellmigration auf Mikrostrukturen bei. Zusätzlich zu den Beobachtungen auf phänomenologischer Ebene, ebnet der quantitative Vergleich mit theoretischen Modellen in dieser Arbeit den Weg für weitere Untersuchungen auf quantitativ-abstrahierender Ebene.

Summary

Cell migration plays an important role in many physiological processes, including embryogenesis, immune response and cancer metastasis. Despite intensive research in recent decades, cancer-associated diseases still account for a significant proportion of deaths in industrialized nations due to the highly diverse process of cancer progression. To specifically target this process by therapeutics, the different variations of cellular interaction with the surrounding need to be disentangled and understood. In this thesis, microstructured surfaces were applied to confine cell migration to standardized adhesive arrays. Various geometries were designed to evoke different cellular behaviours and observe the resulting cytoskeletal dynamics. The abstraction to quantitative observables allowed for tuning of and comparison with theoretical models.

In a first project, the influence of curvature on cell reversal was investigated confining cells to stripes of four different lengths and presenting four different tip geometries. For all lengths, as well as positive and negative curvatures analyzed, no change in cell depolarization time was detected. The overall reversal time for a cell to depolarize in the tip of the stripe and stochastically repolarize was determined to generalize to about 100 min. This general behaviour could be reproduced by a cellular Potts model.

To describe cell migration by a minimal model and presenting a systematic way to optimize model parameters, the parameters of a cellular Potts model were calibrated in a second project. Here, adhesive geometries were used to extract characteristic observables and connect them to the parameters of the model in a one-to-one relation. The fully calibrated model was capable of quantitative reproduction of all geometries with one set of parameters and allowed qualitative prediction for novel geometric designs.

Cellular persistence and spatial memory were accessed by confinement of cells to maze-like structures. We compared cell behaviour to different models of memory and found a model including a reinforcing term and a term for memory degradation over time to achieve best fit.

For a closer look at cell-cell interaction, a previously proposed platform for probing of two-cell interaction was used to investigate the change in cellular behaviour under blocking of cell-cell signalling. We observed the blocking of E-cadherin to lead to a more invasive cell phenotype with reduced reversal upon contact and positive, i.e. accelerating, friction coefficient.

Finally, collective invasion into a channel with constriction was investigated. We found a characteristic velocity profile with reduced velocities establishing ahead of the constriction, which was attributed to the phenomenon of cell jamming. The comparison with a cellular Potts model showed qualitatively very different behaviour.

Taken together, this thesis contributes to a better understanding of cytoskeletal dynamics of migrating cells in confinement. In addition to the insights the phenomenological observations in this work could provide, the abstraction of complex signalling networks to theoretical models provides a quantitative basis for further investigation.

Publications and manuscripts

P1 **Quasi-periodic migration of single cells on short microlanes**
Fang Zhou, Sophia A. Schaffer, Christoph Schreiber, Felix J. Segerer, Andriy Goychuk, Erwin Frey and Joachim O. Rädler
In: *PLOS ONE*, apr 2020, doi:10.1371/journal.pone.0230679

P2 **How to calibrate in-silico (CPM) cells using in-vitro migration assays**
Sophia A. Schaffer, Andriy Goychuk, Erwin Frey and Joachim O. Rädler
To be submitted to: *PLOS Computational Biology*, 2021

M1 **Quantifying Two-Cell Interaction**
Georg Ladurner*, Sophia A. Schaffer*, David B. Brückner*, Tom Brandstätter, Chase P. Broedersz and Joachim O. Rädler
In preparation

M2 **Cellular memory in maze structures**
Theresa-Maja E. Reitz*, Sophia A. Schaffer*, David B. Brückner*, Chase P. Broedersz and Joachim O. Rädler
In preparation

Earlier Work

P0a **Effects of Stochasticity and Division of Labor in toxin Production on Two-strain Bacterial Competition in *Escherichia coli***
Benedikt von Bronk, Sophia A. Schaffer, Alexandra Götz and Madeleine Opitz
In: *PLOS BIOLOGY*, may 2017, doi:10.1371/journal.pbio.2001457

P0b **Boosting Functional Response Models for Location, Scale and Shape with an Application to Bacterial Competition**
Almond Stöcker, Sarah Brockhaus, Sophia A. Schaffer, Benedikt von Bronk, Madeleine Opitz and Sonja Greven
In: *Statistical Modelling*, jun 2020, doi:10.1177/1471082X20917586

* authors contributed equally to the work

Contents

1. Introduction

Die Zelle, einmal gebildet, wächst durch ihre individuelle Kraft fort, wird aber dabei durch den Einflufs des ganzen Organismus so geleitet, wie es der Plan des Ganzen erfordert. Diefs ist das Grundphänomen der ganzen thierischen und pflanzlichen Vegetation.

Theodor Schwann
"Mikroskopische Untersuchungen über die Uebereinstimmung in der Struktur und dem Wachsthum der Thiere und Pflanzen"
Berlin, 1839

Although the first cells were discovered as early as 1665 by Robert Hooke when looking at a thin slice of cork with a microscope, only in 1839 Theodor Schwann first published the theory that all living beings, plants and animals, have cells as their smallest building blocks [1, 2]. During this time, Joseph Récamier had already coined the term metastasis and observed tumor growth and spreading in his patients [3].

Today, the observation of locomoting cells still presents a fascinating field of interdisciplinary research as it is involved in many different processes such as wound healing, immunoresponse and embryogenesis [4, 5, 6]. Cell migration is involved in disease as well, presenting a key process in cancer metastasis causing 25% of deaths in Germany in 2019 [7, 8]. Depending on its environment, metastasis can involve various signalling pathways, adhesion mechanisms and cytoskeletal dynamics making it a highly diversified process [9]. Before a process this complex can be manipulated by therapeutics, the different variations of how cells interact with their surrounding have to be disentangled and understood.

The very start of migration is the polarization of a cell i.e. the establishment of a chemical imbalance across the cell. This polarization can have various reasons such as external chemical or geometrical stimuli, migration in a collective, cell division during wound healing or embryogenesis. Or cells can polarize through stochastic fluctuations. A temporal classification of stochastic polarization can yield insights into the responsiveness of cells, especially when the influence of geometric stimuli can be quantified as well.

With polarization, a complex regulatory machinery starts to activate mechanical processes that lead to physical deformations of the cell [10]. Although the three key players Rac1, RhoA and Cdc42 have been identified to establish, maintain and organize cell polarization and migration, they are entangled in a highly interconnected network [11, 12]. Disentangling this system proves an ambitious task regarding the sheer number of involved molecules and variability in response for different cells or environmental conditions.

In biological settings, cells never appear completely isolated but rather in a context of surrounding tissue, proteins and other cells. During metastasis, trains of invading

cells have been observed to originate from the primary tumour into the neighbouring tissue in a highly adapted process [13]. Here, the analysis and description of collective cell movement as active matter shows various behaviours of cells described as fluids in some cases but rigid solids in others [14, 15]. The transition from fluid to rigid, termed jamming transition, presents an interesting feature already known from foams and rigid spheres and the description in the context of cell migration could lead to findings of generic behaviours such as phase transitions or characteristic instabilities [16]. Also, an investigation of the impact of various signalling molecules onto cell-cell interaction with single cell resolution could help to deepen the understanding of collective invasion from the biological side.

To access the trigger, regulatory network, maintenance mechanism and way of communication of single cell migration and neighbouring cells, artificial *in vitro* systems prove beneficial. By confining cells to well-defined geometries, experiments can be conducted in a reproducible assay enabling high-throughput measurements and easy observation over several days on a microscope. Hereby, different geometric constraints can mimic various cellular environments that lead to the emergence of distinct migratory responses. While cells in 3D environments mainly show amoeboid-like migration, restricting cell migration to locomotion on adhesive 2D-surfaces typically leads to a mesenchymal migration type. This type of migration is characterized by elongated cell shapes with actin rich protrusions at the cell front and tappered tails at the back. Since cell migration in this mesenchymal mode relies on the formation of focal adhesions for spatial displacement, geometric patterns of cell adhesive proteins can confine and direct cell migration. Prominent examples are cell adhesive patterns which have been frequently used to observe collective invasion [17, 18], cytoskeletal organization [19, 20] or speed and persistence of individual cells [21, 22]. Other purposefully designed patterns open the floor for challenges such as ratchets, non-adhesive gaps, narrow bridges or pillars that probe particular aspects of migration [23, 24, 25, 26, 27]. Such micropatterning techniques that create defined areas for cell adhesion allow for reduction of the natural spatio-temporal complex dynamics and enable better statistics due to unified conditions in arrays. This enables the extraction of meaningful observables despite the naturally high cell heterogeneity.

Such observables are a suitable basis for models [28]. Finding general laws describing the motion of cells can allow the prediction of intrinsic generic behaviours that can be a basis for future experiments, for instance for collective movement at various densities [29, 30]. In this way, physical models can be used to predict potentially interesting phenomena or vice versa when biological systems are employed to explore physical questions. Furthermore, such models can be able to disentangle stochasticity and deterministic terms, allowing direct access to the underlying dynamics veiled by fluctuations [26]. More descriptive physical models such as cellular Potts models are a versatile tool to construct a minimal reproductive system abstracting from highly complex biochemical networks and scalable from single cells to huge collectives [31, 32, 33].

This reduction allows to investigate the relative importance of the different cellular processes and the exploration of dominating signalling pathways without the phenomenon of compensation present in biology. Although cellular Potts models rely on parameters for all implemented mechanisms and are computationally rather expensive, a systematic parameter determination could be used to greatly reduce the computational time needed for calibration.

In this thesis, we investigate cytoskeletal dynamics of cells on microstructures from different perspectives. Additionally to phenomenological observations, we compare our findings with theoretical models to open the way for quantitative abstraction of complex signalling networks.

This thesis is structured in the following way:

Chapter 2 introduces the fundamental concepts behind major components of this thesis. It discusses the basic process of cell migration both on a single cell and a collective level with special emphasis on the regulation of cell polarization and involved proteins. In addition, an overview of different modelling approaches for cell migration from collectives to single cells is given. Finally, the chapter presents different methods for the fabrication of adhesive geometries for cell confinement.

In chapter 3, single cell migration in stripes is studied under varying lengths and tip geometries. Reversal times and velocities are investigated. A common reversal time and velocity distribution is uncovered that neither depends on the length of the stripe nor the curvature at the stripe ends. Interestingly, this contrasts to curvature-induced polarization reported earlier as we could report no influence of curvature on reversal times and thus possibly on depolarization. The experimental findings could be reproduced by a cellular Potts model. The results of this chapter are recorded in publication P1.

In chapter 4, we propose a systematic method to stepwise calibrate a cellular Potts model by establishing one-to-one relations to experimental observables extracted from single cell migration on different adhesive geometries. We could obtain a full set of parameters that is able to simultaneously reproduce all geometries used for calibration and allows qualitative predictions for untrained structures. The results of this chapter will be submitted for publication shortly.

In chapter 5, migrational persistence of single cells in maze structures is investigated. Discretizing decisions, we could show subsequent cellular choices not to be a Bernoulli process but to be clearly biased towards previous choices. Furthermore, a one parameter model was not able to reproduce the bias in relative frequency of choices observed in experiment. We could show a two parameter model accounting for a modification in choice preference and a temporal degradation thereof of qualitatively describe the observed behaviour. This shows cell migration in a maze to be a process rich in phenomenology rather than spatial inertia.

In chapter 6, the transmission of polarization upon contact of two cells is examined in

a dumbbell-shape that provokes heads-on collisions of cells. In expansion to a previous study characterizing two-cell motion in this confinement [34], we analysed the influence of functionally blocking E-Cadherin on invasiveness and could determine a clear change to more invasive behaviour in this geometry for the two cell lines compared. Thereby, we manage to disentangle the influence of cell-cell signalling proteins on the coupling of polarization and the resulting migratory behaviour in quantitative terms of repulsion and friction coefficients.

In chapter 7, collective flow of cells through channels with a constriction is investigated. Cells show the development of a characteristic velocity profile along the direction of invasion with reduced velocities prior to the constriction and an increase therefrom towards the cell front. This suggests a rise in cell number and density to lead to a jamming of cells in front of the constriction, a phenomenon contrasting the description of cells as a Newtonian fluid in channels without constriction. Results from experiments are compared to a cellular Potts model and found to show quantitatively very different behaviour.

Chapter 8 summarizes the ideas and results of this thesis and gives an outlook onto reasonable further experiments. Additional expansions and improvements to the presented assays are discussed that could further deepen the understanding of cell polarization. Appendixes A and B contain a brief description of experimental procedures such as cell culture and experimental setup, as well as the data analysis developed in the course of this thesis.

2. Concepts - Cell Migration and Modelling

To facilitate the discussion of experimental approaches and their results, this chapter briefly reviews the background information. It introduces the fundamental concepts of cell migration and gives a short introduction to different modelling approaches of migrating cells.

2.1. Cell Migration

While details of migration may vary a lot between different types of cells, in general, cells go through five different steps during migration that repeat cyclically. These phases are polarization, extension of the membrane in the front, attachment of the protrusion to the substrate, building of forces resulting in displacement and release of old attachments at the back [35]. This cycle is illustrated in Fig 2.1 and differs greatly in overall duration, length and peculiarity of the phases between cell types. Thus migration persistence as well as speed are broadly distributed for different cell lines [36].

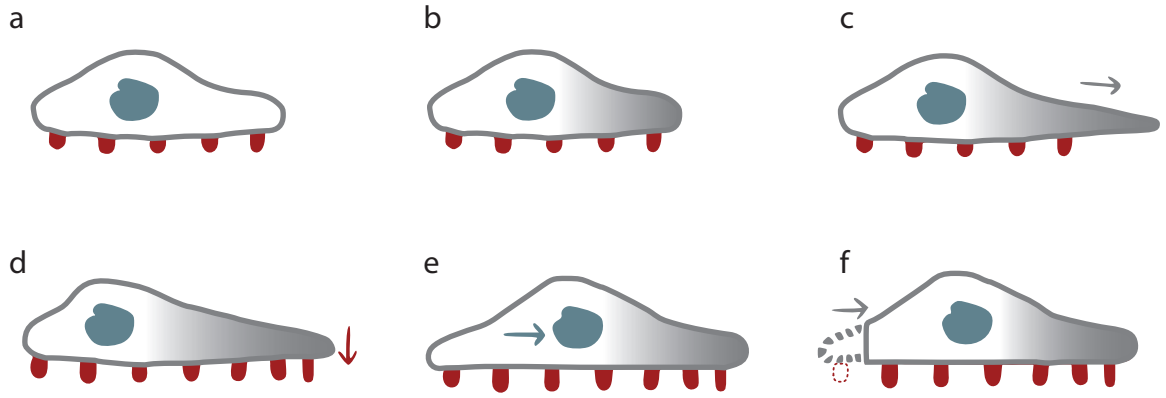

Figure 2.1.: Cyclic process of cell migration. **(a)** A not oriented cell **(b)** polarizes, **(c)** a protrusion in the direction of polarization is formed and **(d)** attached to the substrate, **(e)** traction forces are build resulting in a displacement of the nucleus and **(f)** old adhesions to the substrate are released. Then the cell either depolarizes (a), repolarizes into a new direction (b) or forms another protrusion in the same direction (c).

Taking a look into the intracellular processes, the actin machinery can be identified as driving factor [37, 38]. The actin cytoskeleton is one of the three stabilizing skeletal components present all over the cell, next to microtubuli and intermediate filaments. The actin network is attached to trans-membrane molecules such as integrins and connects the cell to its surroundings [39]. It plays a major role in cell migration [38]. Even the actin bundles enveloping the cell nucleus influence migration [40]. Actin itself is already a polarized, directed filament, as new monomers are quickly added at the barbed end and slowly removed at the pointed end, resulting in a preferred elongation in the

direction of the barbed end. Protrusions as depicted in Fig 2.1c are pushed forward by actin filaments deforming the cell membrane. In lamellipodia, i.e. large broad protrusions, the filaments are branched by Arp2/3 and cross-linked, thus leading to a dense actin network inside cells [38, 41]. In filopodia, i.e. small finger-shaped protrusions at the very front of lamellipodia, actin is organized into bundles [42]. All these processes such as actin branching, actin nucleation, integrin activation in adhesion and building of stresses resulting in displacement are orchestrated by complex signalling networks [10, 43]. The conductors in this signalling orchestra are the Rho GTP-ases, above all Rac1, RhoA and Cdc42 [44]. These key players will be discussed in more detail below in the context of cell polarization.

2.2. Cell Polarization

In the very first step of cell migration, the previously existing symmetry inside the cell is broken and a molecular gradient is established, a process referred to as cell polarization.

2.2.1. Keys to Polarization

Polarization in migrating cells spans over several orders of magnitude. In collectively migrating cells, velocity is coordinated over multiple cell diameters on the range of 200 μm [45], whereas in single cells, polarization is sensitive to small curvatures in the size of 60 nm [46]. This requires a complex network for regulation and communication on the intra- and intercellular level.

A cell can process many different external signals to decide for one specific direction of migration. Cells can be guided by chemical gradients, e.g. growth factors, a process called chemotaxis [47] that is even more sensitive if cells "sense" collectively [48]. In contact with the surrounding matrix, they can move into the direction towards stiffer substrates, called durotaxis [49], or into the direction that allows more adhesions to the ground, called haptotaxis [50]. Depending on the shape of protrusions of single cells, also specific adhesive geometries surrounded by repellent surface, called micropatterns, can induce a preferred movement direction [24]. Or cells can simply polarize into any direction by stochastic fluctuations.

2.2.2. Intracellular Polarization

During the process of polarization, the cell turns from a previously symmetric to an unsymmetric state. This desymmetrization evolves through all intracellular levels, started by small proteins activating signalling cascades that amplify the chemical asymmetry. This stimulates mechanical processes that start to physically deform the cell via actin protrusions. The now polarized cell starts migrating as described before in Fig 2.1.

Rac1, RhoA and Cdc42

Inside a cell, three key players have been identified to establish, maintain and spatially organize polarized protrusions: Rac1, RhoA and Cdc42 [44, 11]. First proposed in 1992 [51, 52], up to today a highly interconnected and complex regulatory network has been discovered [12]. Rac1, RhoA and Cdc42 are all members of the Rho GTPase family, a group of enzymes that can hydrolyse and bind to guanosine triphosphate (GTP). Guanine nucleotide exchange factors (GEFs) activate Rho GTPases, GTPase-activating proteins (GAPs) deactivate them [53]. And guanine nucleotide dissociation inhibitors (GDIs) extract them from the cell membrane, thus altering their location and mobility [54]. This classical interaction scheme is depicted in Fig 2.2.

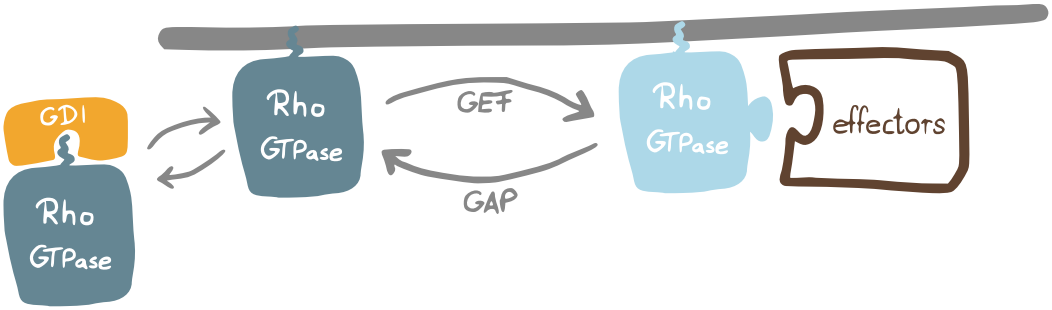

Figure 2.2.: Switching cycles of Rho GTPases. Extraction from membrane by GDIs, activation by GEFs, deactivation by GAPs and interaction of active form with effector target proteins.

Depending on their localization, the Rho GTPases can have different functions. At the front of a polarized cell, **Rac1** can be found in lamellipodia and in membrane ruffles [52]. In neutrophils, it was discovered to be crucial for retraction and localized at the back of cells [55]. **Cdc42** was reported to be necessary for directed polarization towards a chemical attractant [56], as well as formation of filopodia [57] and orientation of the microtubuli organizing center (MTOC), a frequent measure of polarization [58]. At first, **RhoA** was discovered to initiate stress fibre formation by activating actin-myosin contractility at the trailing edge of cells [51]. With advances in imaging and biosensor development, this rather simple picture of distribution has been complemented by discoveries of RhoA impact on stabilizing microtubuli at the cell front [59], as well as the temporarily and spatially extremely precise localization at the very tip of a lamellipodium, reaching back only 2 μm for 40 s [60].

These quite distinct roles in polarization of RhoA can be explained by looking at the regulatory network of Rho GTPases. Although this network by itself is quite simplistic, compare Fig 2.2, over 60 GEFs and 70 GAPs have been identified for the whole Rho GTPase family [61, 62]. Furthermore, orchestrating all intracellular processes for migration with respect to the current cell environment requires much more sophisticated regulation of Rho GTPases rather than simple activation by GEFs, binding to an effector protein and deactivation by GAPs. Hence, there have been studies investigating

the potential of GEFs to form complexes [12], the post-translational modifications of Rho GTPases [54], and how GEFs and GAPs directly regulate each other [63]. This leads to a highly complex and intertwined network around the key players Rac1 and RhoA with several interconnected layers of regulation as shown in Fig 2.3.

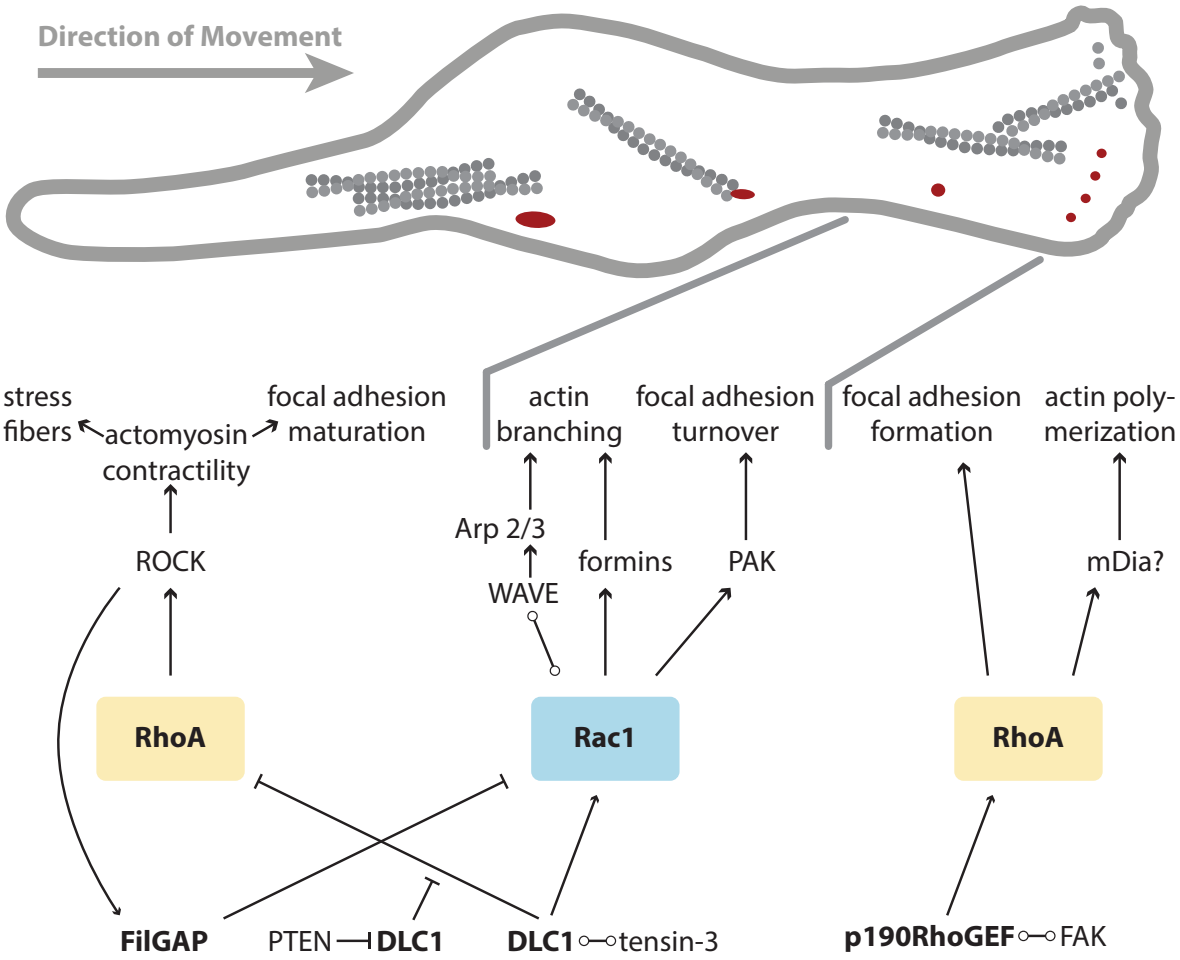

Figure 2.3.: Highly reduced regulatory network for Rho GTPase signalling in a migrating cell. Focal adhesions are depicted in red. Starting with many nascent adhesions, some are turned over, i.e. removed, others are preserved and mature under mechanical stress to larger adhesions that are finally dissolved at the rear. The actin-cytoskeleton is depicted in grey. Single actin strands are polymerized at the leading edge, branched in the lamellipodium and bundled and reinforced into stress fibers in the cell body. Rac1 and RhoA signalling pathways for regulation of adhesion and actin-cytoskeleton are depicted below. Arrows indicate activation, blunt ends indicate blocking or deactivation and circles stand for co-localization. Exemplary GEFs and GAPs are indicated by bold letters.

In the figure, the cell is subdivided into three segments governed by distinct Rho GTPase dynamics, the leading edge, the lamellipodium and the cell body. At the cell front, new adhesions to the substrate are formed and single actin filaments are polymerized, leading to a forward pushing of the membrane. These two processes can be mediated by

RhoA, that is activated at the leading edge [64]. The activation of mDia by RhoA at the leading edge has been suggested but not been proven so far [65]. The protein mDia is part of the formin family, that is involved in actin nucleation, elongation and bundling [66]. RhoA itself can be activated by many different GEFs, of which p190RhoGEF has been reported to initiate the formation of focal adhesions upon binding to focal adhesion kinase (FAK) in fibroblasts [67].

In the lamellipodium, cell migration is dominated by Rac1-based signalling. As a fine balance between adhesion and actin polymerization is needed for cell migration driven by lamellipodia, actin is branched and some primary focal adhesions are turned over, i.e. dissolved, in this part of the cell [65]. For the activation of Rac1 for focal adhesion turnover, several GEFs and their formed complexes have been identified [12]. For the sake of simplicity, they are not depicted in Fig 2.3. Two examples for different pathways that regulate focal adhesion turnover by activation of Rac1 are its activation by the GEF TIAM1 in a complex with talin, a focal adhesion protein, and by the GEF β-PIX under involvement of PAK (p21-activated kinase) and paxillin, another focal adhesion protein [68, 69]. For actin polymerization, Rac1 interacts with the WAVE complex that in turn activates Arp 2/3, a protein leading to the nucleation of actin branches [70]. It has also been reported that Rac1 can remodel the cytoskeleton by interaction with formins [71]. The dominance of active Rac1 in the lamellipodium over active RhoA can among others be established by the GAP DLC1 that couples to tensin3. This complex deactivates RhoA and is proposed to activate Rac1 by a yet unidentified GEF [72, 73].

At the cell rear, DLC1 froms a complex with PTEN that upon binding inhibits DLC1 activity. The inhibited DLC1 no longer deactivates RhoA and hence leads to an increase in RhoA induced signalling. Foremost, RhoA leads to ROCK induced actomyosin contractility [74]. This contractility in turn leads to the maturation of focal adhesions and the formation of stress fibers. Additionally, the contractility is postulated to block the formation of additional lamellipodia [75]. One possible signalling pathway is the activation of the GAP FilGAP by ROCK that leads to a deactivation of Rac1 as depicted in Fig 2.3 [65].

Two reviews by Ridley [65], and Lawson and Ridley [12] present a more complex regulatory mechanism for Rho GTPase signalling including, more rarely regarded GTPases and different GEF and GAP complexes. However, this highly complex signalling network is far from completely understood and still requires further investigation such as for instance the role of GDIs in spatially modulating GTPase activation by extrusion from the membrane to the cytosol of the cell.

Guilluy *et al.* [63] reduced the complex and not yet fully known regulatory network of RhoGTPases to the two key players Rac1 and RhoA as depicted in Fig 2.4. Here, Rac1 is dominantly present at the leading edge of a migrating cell, only disrupted by the rapid activation of RhoA and the following activation of Rac1 during an protrusion-retraction cycle of a lamellipodium, shown with enhanced spatial extension. At the cell rear, active RhoA dominates and down regulates Rac1.

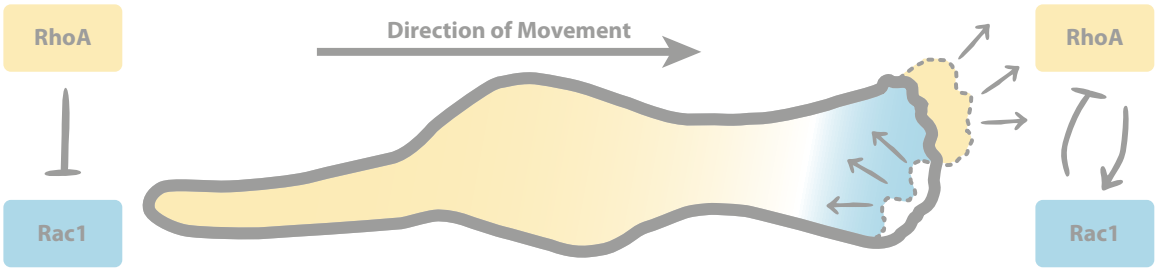

Figure 2.4.: Distribution of active Rac1 (light blue) and active RhoA (pale yellow) throughout a cell as well as spatially dependent mutual regulation.

Machacek *et al.* [60] use FRET sensors to access spatio-temporal timing at the leading edge of migrating 3T3 cells. They show that RhoA is activated synchronized with actin polymerization at the very edge of the protrusion, whereas Rac1 and Cdc42 are activated 2 μm away from the edge 40 s afterwards [60]. In this thesis, the time resolution for experimental image acquisition typically is 10 minutes. Hence, for mere visualization of polarization, simple actin staining has no temporal signalling delay in comparison to experimental time resolution and was used in section 3.2. Furthermore, during 10 minutes the cell has already undergone measurable displacement so that even the nucleus position is a valid access point to the direction of polarization. In section 8 other polarization markers are discussed that could be useful in future experiments with higher temporal resolution.

Myosin-VI in Polarization

Yet, the Rho GTPases and their complex signaling network are not enough to mechanistically polarize a cell via protrusions and exert forces onto the cytoskeleton to physically move the cell. Here, cellular motors come into play. On microtubuli, kinesin and dynein motor proteins move cargo into plus or minus direction. On actin filaments, the myosin family transports molecular cargoes under ATP hydrolysis. Of the 18 known classes of myosins, all but one move towards the barbed, plus end of actin [76]. So far, only myosin-VI (myo6) was discovered to move in the opposite direction towards the pointed, minus end [77], making it a motor protein of particular interest. It is present in all higher eukaryotes [78], strongly bound to actin [79] and exists in four different isoforms in humans that can be expressed in response to different environmental conditions [80]. It was shown to be present at the dynamic membrane ruffles at the leading edge of migrating cells [81].

The detection of myo6 throughout the cell suggests involvement in multiple cellular processes and specific spatial regulation [82]. These processes include clathrin-mediated endocytosis [83], anchoring of the plasma membrane of stereocilia [84] (the lacking results in deafness [85]) as well as presumed roles in stabilizing and sorting in the Golgi complex [86, 87]. Additionally, it has been reported to form a complex with β catenin

and E-cadherin, suggesting it develops a protrusive force that pushes actin filaments against the membrane to create protrusions [88].

To this end, recent studies by Rogez *et al.* [46] have revealed the capability of myo6 to remodel membrane curvature, one of the key processes in cell polarization and migration [89]. In their *in vitro* experiments, they demonstrate how the direct motor protein-lipid interaction of myo6 remodels the membrane geometry at the range from nano- to micrometer scale into flower-shaped membrane pores. By "seeding" the membrane with nanostructures that offer negative gaussian curvatures in the radius of about 60 to 80 nm, they were able to show a strong preference of myo6 for these negative curvatures. Their *in silico* model, consisting of a curvature-dependent recruitment term of myo6 to the membrane and an effective line tension, strengthens the claim of direct myo6 lipid interactions as sufficient to remodel the membrane. Thus, small curvatures on the length scale of 60 nm provide an interesting experimental basis to study the impact of myo6 on cell polarization and migration.

In conclusion, cell migration is a spatially and temporally highly regulated, complex process. Stochastic fluctuations lead to the formation of a cell front and back, differing in activity of Rho GTPases. The actin cytoskeleton is the scaffold used to push new protrusions outwards at the leading edge. This formation of lamellipodia involves complex interplay of Rho GTPases for signalling, myosins for translocation and actin as physically displacing building block.

2.2.3. Coordination of collectively migrating cells

The polarization of cells is getting even more complex when cells no longer migrate solely but move as small cohorts or large groups, referred to as cell sheets. Here, not only single cells polarize but they also need to communicate their polarization to neighbouring cells, coordinate a direction of migration and move cohesively, often without loosing contact. To coordinate their movement, they employ physical or chemical signalling either through direct cell-cell contacts or via interaction with the extracellular matrix, the surrounding of cells. Such coordinated movement is more sensitive to external stimulants [90] and more persistent [45] than single cell migration.

There are recent reviews by Trepat and Sahai (2018), Ladoux and Mège (2017), Friedl and Mayor (2017), and Mayor and Etienne-Manneville (2016) that broadly discuss the current knowledge on collective cell migration with focus on mesoscale physical principles [91], the mechanobiology [92], cell-cell-junctions [93] and front-rear organization [94].

Here, selected aspects thereof are shortly presented. Similar to single cells, front-rear asymmetry in coherently migrating groups of cells is based on actomyosin [95]. Collective cell movement consists of cross-cell polarization, cell-cell interfaces and coordinated multicellular displacement [96]. Ways of cell-to-cell communication involve three different junctions, namely cadherin-based adherens junctions, tight junctions and

desmosomes [92]. For this thesis, adherens junctions are of most interest as cadherins are studied in section 6. These are of importance in communicating stresses and mechanically couple cells to each other [97]. At the very front of a polarized cell group, the first cells indicate direction and are often morphologically distinct from the rest, they are called leader cells [94]. All cells behind the leader cells are called followers. Leading cells have more contacts to external signals [94], larger focal adhesions [92] and their polarization is induced by the lack of junctions at the free edge [94]. They do not simply drag along the cell sheet but engage in a global tension field involving all cells that can be seen as a tug-of-war [98]. The conformation of leader and follower cells is subject to fluctuations and leader cells can fall behind while former follower cells emerge as new leaders [91]. Studies using photoactivatable Rac by Wang *et al.* [99] showed induction of protrusions and emerging leading behaviour as a transient state. Furthermore, at decreasing Rac activity in leading cells, other cells behind the leader develop protrusions and take over the lead indicating the importance of Rac for the emergence of protrusions and leader cell position.

Cells throughout the epithelial sheet are connected to the front cells by adherens junctions. One of the junctions' main components can be E-cadherin, a homophilic transmembrane protein that links two cells by tight binding in the extracellular domain and is connected to the actin cytoskeleton on the inside by accessory proteins called catenins [100]. E-cadherins and its regulators play an important role in communicating stresses and forces between cells [101] as well as in multiple developmental processes associated with cancer metastasis such as the epithelial to mesenchymal transition where cells gain invasive properties and, detached from the collective, start migrating actively [102]. The precise tuning of cadherin number is crucial for coherent cell motion, as down regulation and overexpression both lead to a collapse of coordinated collective migration [103, 95, 17].

During collective movement, only the leading cells form big visible protrusions. However, small lamellipodia slipping under the cells in front have been observed and called cryptic lamellipodia [104]. These small lamellipodia play an important role in signalling, as protrusions induce downstream cascades leading to cohesive movement of cell cohorts via the previously described Rac1-RhoA pathway. All Rho GTPases fulfil the same tasks as in single cell migration, although they now additionally regulate and control cell-cell contacts and cell-to-cell signalling. Rac1 plays a significant role in closure of gaps in cell monolayers by promotion of cells crawling into the gap [105] as well as leader-follower conformation [99]. For polarization of leading cells in monolayers, Cdc42 is needed in different cell types [106, 107]. Presumably, RhoA not only controls myosin-based contractility but also the lateral coupling in cadherin-based cell-cell contracts [95].

Although the exact molecular details of collective migration may vary substantially in different types of cells, Fig 2.5 shows a reduced scheme of cell-cell coupling employed in this thesis. As for single cell migration, we focus on the distribution of Rac1 and

RhoA that is not changed much. Only the cells at the very front of the sheet exhibit clearly pronounced lamellipodia. Cells further behind show small, so-called cryptic lamellipodia reaching only little beneath the cell in front. Polarization in the cell sheet is achieved via mechanical stresses in the actin cytoskeleton that can be communicated by E-cadherin based adherens junctions. Myosin VI is located at these juctions and on actin filaments at the cell front.

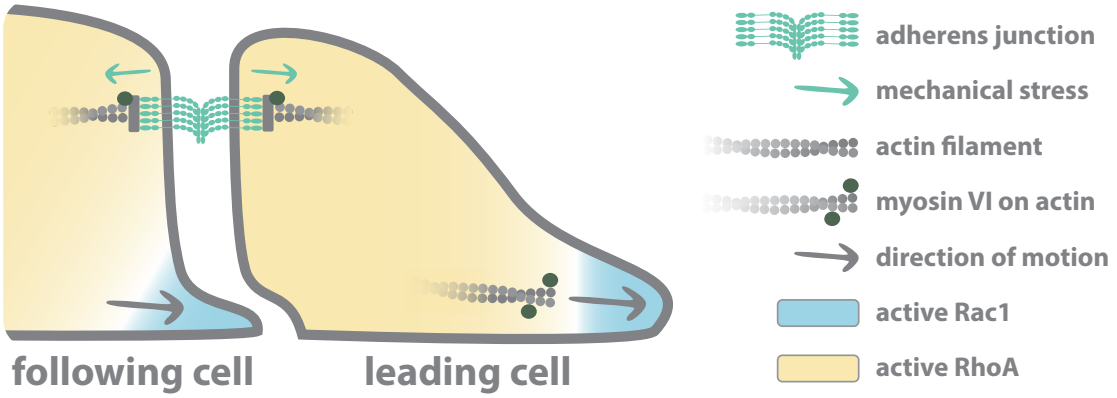

Figure 2.5.: Scheme of collectively migrating cells reduced to leading cell and first follower. Cells are connected by adherens junctions based on E-cadherin that communicates mechanical stresses throughout the cell sheet and is coupled to the actin cytoskeleton. Myosin VI is co-localized on actin at the connection to E-Cadherin as well as at the leading edge. Distribution of active Rac1 in lamellipodia is depicted in blue and active RhoA in the cell bulk in yellow. The lamellipodium of the leading cell is much more pronounced than in the following cells that only exhibit small, cryptic lamellipodia slipping beneath the cell in front.

2.3. Models for Cell Migration

Although much can be learned about cell migration by modifying the biology and analysing the resulting changes, a physics perspective on cell dynamics aims for a more general description. Such a description is achieved by abstracting and reducing the plethora of bio-chemical processes to a minimum model. In the field of cell migration, many different models are well established. However, most of the currently employed models have their specific scope of application, e.g. collectives from small cohorts to hundreds of cells, single cell dynamics or intracellular processes, and do not describe the whole plethora of cell migration phenomena in detail. An overview of modelling approaches for cell collectives is given by Alert and Trepat [108], whereas single and intracellular models are discussed by Danuser *et al.* [109]. A very detailed overview on different modelling approaches for adherent cells, singles and collectives, as well as abstraction possibilities for the underlying biology is given in Schwarz and Safran [110].

In the following, only models applicable to the experimental scope of this thesis are shortly discussed. In a zoom-in, at the beginning models for the description of a ”liquid

of cells“ are discussed and followed by models including more and more cellular details at the cost of the capability to only describe fewer to single cells, resulting in a short overview of intracellular models that describe signalling dynamics inside a single cell without displacement or interaction to the surroundings.

2.3.1. Collective Cell Migration

Collective cell migration is an umbrella term as cell collectives can span orders of magnitude in cell number and spatial extension from the description of thousands of cells to as few as two interacting cells. This section starts with models describing collective migration of a few hundreds of cells.

Continuum models

Continuum models are models that describe cells not on a particle resolution, but as temporally and spatially evolving fields $X(\mathbf{r}, t)$ described by partial differential equations. Nematic models are a type of continuum models where the fields describing cells have an order parameter that is invariant to rotations under 180° [111]. These fields can describe velocity, density or polarity. Alert and Trepat [108] systematically build up a model starting with a free energy of quiescent compressible polar media. Adding density and polarity dynamics, overall force balance in the tissue, viscoelastic properties, traction forces described in [112] and boundary conditions, they arrive at a very general description based on liquid crystal principles [108]. A subclass of nematic models is the Toner and Tu [113] field generalization of the classic Vicsek model [114], often referred to as dry active matter, as hydrodynamic interactions are not included [115]. Modelling cells as active nematic liquid crystals has succeeded in linking isotropic stresses leading to protrusion from a confluent cell layer to topological defects suggesting an analogy between epithelial sheets and active nematics [116].

Cell sheets invading a straight channel are well described by simple hydrodynamic laws in the form of a Fisher-Kolmogorov equation as in [14]:

$$\frac{\partial c(x,t)}{\partial t} = D_c \frac{\partial^2 c(x,t)}{\partial x^2} + \lambda c(x,t)(1 - \frac{c(x,t)}{k}),$$

where $c(x,t)$ is the one dimensional density over x ranging from cell front back to channel entrance at time point t, λ describes exponential growth up to approaching the carrying capacity k where growth saturates, and D_c is the collective diffusion coefficient. However, when introducing a constriction inside the channel, simple hydrodynamic laws no longer accurately describe cell motion. Here, even a more advanced active nematic liquid crystal model shows clear deviations from experiments and is not able to describe velocity fields correctly as shown in Fig 2.6 [117, 118].
Collective flow through a constriction is again shortly discussed in section 7 and an outlook on an alternative to investigate this type of motion is given.

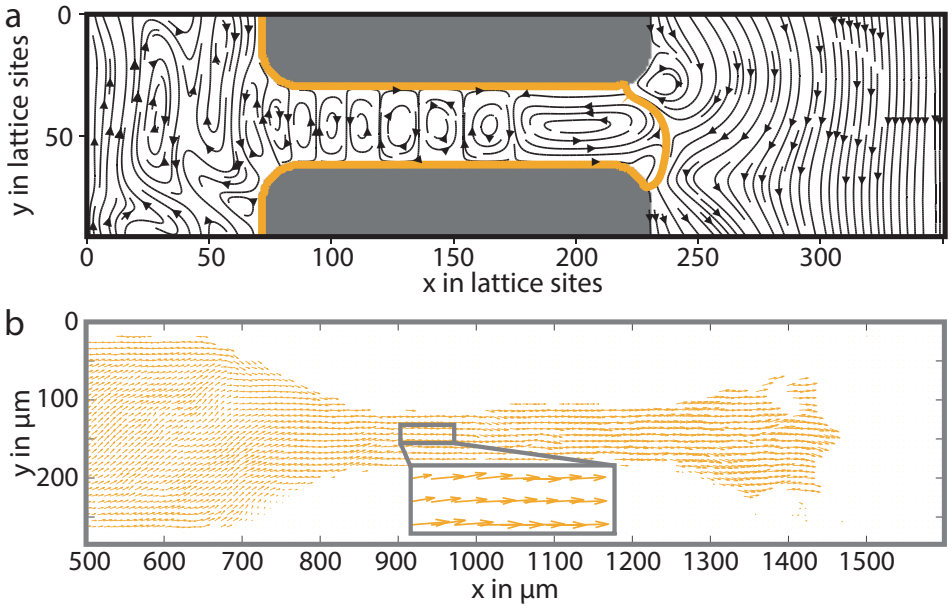

Figure 2.6.: Comparison of velocity direction in simulation and experiment. **(a)** Velocity field orientation as calculated in the active nematic liquid crystal model. Yellow line indicates the current position of the cell sheet, i.e. the border between nematic and isotropic phase. In front of the constriction flows are mostly perpendicular to the channel and inside the constriction vortices dominate. **(b)** Velocity field orientation as extracted from experimental data via particle image velocity in yellow. Prior to constriction movement is mainly directed into the constriction where flow is even more oriented parallel to the channel. Images courtesy of M.L. Zorn adapted from [117].

Single Particle Resolution

A more detailed level of modelling are models that discern different cells. Single particle models such as the Vicsek model have a phenomenological alignment term motivated by animals flocks and can show spontaneous formation of particle flocks spanning the whole system [114]. Phase field models describe multiple cells $i \in \{1, ..., N\}$ by spatially varying fields $\Phi_i(\mathbf{r}, t)$, one per cell [119]. They have been applied to simulate collective cell migration around a circular object [120] or dynamics of elastic cell monolayers [121]. As described in [122], collectively migrating cells can be modelled as isotropic particles [123], deformable particles [124] or polygons described via Voronoi tesselation [125].

When turning the focus from cell collectives more onto cell interactions, one can reduce the number of observed cells for the benefit of more details in intracellular dynamics. Fully describing all cellular interactions with data-derived equations of motion is still a challenge as disentangling deterministic from stochastic contributions is hard. Here, Brückner *et al.* recently introduced underdamped Langevin inference to derive a model framework directly from experimental data [126].

2.3.2. Bridging the Scale

In their most recent work [34], Brückner *et al.* reduce the complexity from large groups of cells to a minimal model for cell-cell interaction consisting of two cells in a 'cell collider' thus bridging from the description of collective migration to the modelling of single cells. Here, cells are represented by point-like particles with a certain position and velocity.

Cell-Cell Interaction Model

First used for the description of single cells in a two-state micropattern [26], Brückner *et al.* propose a stochastic equation of motion with predictive power to describe two-cell interactions as follows [34]:

$$\frac{dv}{dt} = F(x,v) + f(|\Delta x|)\Delta x + \gamma(|\Delta x|)\Delta v + \sigma(x,v)\eta(t),$$

where $F(x,v)$ describes the interaction of a single cell with the confinement, as in [26]. The cell-cell interaction is decoupled into two terms accounting for cohesion $f(|\Delta x|)\Delta x$ and friction $\gamma(|\Delta x|)\Delta v$, the Δ indicating relative position and velocity of the two cells. The stochastic contribution influencing motion is presumed to be described by a Gaussian white noise $\eta(t)$, with mean $\langle\eta(t)\rangle = 0$ and $\langle\eta(t_1)\eta(t_2)\rangle = \delta_{t_1,t_2}$. They apply their method of undamped Langevin inference [126] and fit the single cell term $F(x,v)$ up to third order in a Fourier basis in x and polynomials in v (see Supplement S4 in [34]). They resolve different types of cell-cell interactions, spanning a two-dimensional plane along the friction - anti-friction axis and the attraction - repulsion axis with two cell lines being located in different quadrants [34].
This concept is also used for the analysis in section 6.

Cellular Potts Model

Another model living on the mesoscale and applied in sections 3, 4 and 7 is the cellular Potts model (CPM). In 1962, Steinberg suggested that many multicellular processes can be attributed to differences in cell-cell and cell-substrate adhesion [127]. Intrigued thereby, Graner and Glazier developed a cellular interpretation of the Potts model, where degenerated spins $\sigma(i,j) = 1,2,...,N$ identify areas of N cells on a lattice of all connected sites (i,j) [128, 129]. Emanating from their model, all CPMs are lattice based models described by a Hamiltonian, minimizing free energy, and modelled with a Monte-Carlo scheme. Today, there are many different applications of cellular Potts models in collective migration [130, 131, 132], for small groups of cells [133], as well as in single cells [31, 134].

Here, the model described by Thüroff, Goychuk *et al.* [33] is used. This model features a scalar internal polarization field that can be seen as abstraction of the biochemical Rac-Rho network as well as mechanical coupling via a constrictive term, making it a

versatile hybrid model. It has been previously applied in studies investigating small groups of cells on circular micropatterns [133], single cells on substrates of different stiffnesses [135] and in short microlanes [136] and cell collectives migrating through a constriction [137].

Here, we focus on the case of a single cell in confinement which is most relevant for the present work. A cell in confinement is described by three fields that each assign a numeric value to all grid sites: The temporally invariant "confinement field" D that is zero for all hexagons of the micropattern and assigns a numeric energy penalty onto all cell-repellent sites of the confinement. The "polarization field" ε that assigns temporally evolving values of "activity" to all hexagons of the cell and is zero on all other sites. The "regulatory field" $F \in \mathbb{Z}$ that is used for bookkeeping during simulation sub-steps and reset to zero after each main step. An illustration of these fields is shown in Fig 2.7. D is ∞ on all grey tiles of the confinement and zero on all others. ε is zero on all tiles that are not occupied by the cell, i.e. do not have an orange contour, and changes over time in all tiles of the cell ranging from minimal to maximal polarized. F is zero everywhere except the tiles of the shaded circles where it is -1 for retraction and $+1$ for protrusion.

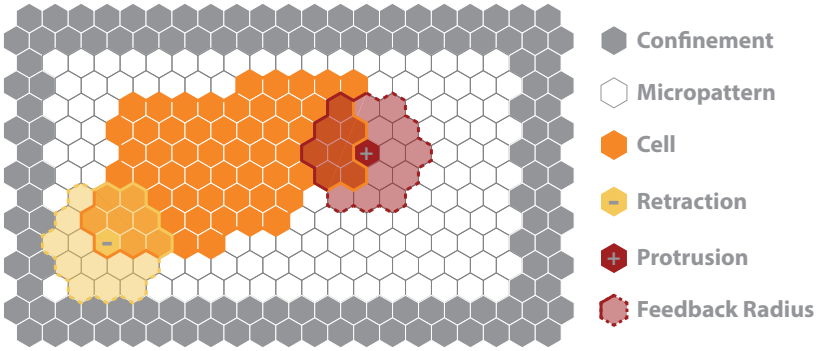

Figure 2.7.: Illustration of the CPM as described by [33] for single cells on a micropattern. Confining hexagons not accessible to the cell are coloured in grey. Grid sites occupied by the cell are indicated by an orange contour. Retraction or protrusion sites are indicated by - (yellow) or + (red). Cell sites within a feedback radius R from the retraction or protrusion site are shaded in the respective colour.

The durations of the simulation is measured in Monte-Carlo-Steps (MCS). The MCSs are subdivided into smaller steps each, so-called elementary events ϑ. The number of elementary events occurring in a MCS is dependent on the number of empty grid sites along the contour of the cell. For each elementary event ϑ, a random hexagon of the cell contour is chosen and an empty adjacent site next to it. With equal probability one of two events is attempted: Retraction from the occupied site or protrusion into the adjacent field, both depicted in Fig 2.7. Then, an acceptance probability for this event $p(\vartheta)$ is calculated and evaluated. If the event is discarded, a new elementary event starts. If the event is accepted, the cell grid is updated accordingly and noted in the bookkeeping field F. A new elementary event starts until all ϑ of one MCS have been

performed. Then, F is used to update the polarization field of the cell ε, a new MCS is started and the number of elementary events ϑ is determined anew until all MCS of the simulation have been performed.

The determination of the acceptance probability of elementary events $p(\vartheta)$ is focused on in this paragraph. All simulation parameters used in the following paragraphs are listed in overview Table 2.1. The acceptance probability consists of a product of two independent contributions:

$$p(\vartheta) = \min\{p_{cont}(\vartheta) \cdot p_{cyto}(\vartheta), 1\} \quad ,$$

where $p_{cont}(\vartheta)$ is a term accounting for cell contractility and $p_{cyto}(\vartheta)$ can be seen as outwards driving cytoskeletal force.
The cell contractility term $p_{cont}(\vartheta)$ is determined by a change in contractile energy

$$\mathcal{H}_{cont}(\vartheta) = \kappa_A A(\vartheta)^2 + \kappa_P P(\vartheta)^2,$$

with A being area and P perimeter of the cell and κ_A and κ_P positive coupling constants. The elementary event ϑ causes a change in contractility $\Delta\mathcal{H}_{cont}(\vartheta) = \mathcal{H}_{cont}(\vartheta) - \mathcal{H}_{cont}(\vartheta_0)$ with ϑ_0 describing the current state of the cell units. This results in a term

$$p_{cont}(\vartheta) := exp\left(\frac{-\Delta\mathcal{H}_{cont}(\vartheta)}{k_B T}\right)$$

which reflects the probability ratio between the probability $q_{cont}(\vartheta) \propto exp\left({}^{-\mathcal{H}_{cont}(\vartheta)}/_{k_B T}\right))$ of the proposed state given by ϑ and the probability $q_{cont}(\vartheta_0)$ of the current state ϑ_0. This connects the proposed sampling scheme to a Metropolis algorithm [138].
The cytoskeletal term $p_{cyto}(\vartheta)$ contains the previously introduced three fields for confinement D, polarization ε and the bookkeeping regulatory field F. The field D is constant for the whole simulation and F is reset at the beginning of each MCS and only needed for the evolution of ε. At the beginning of the main simulation, the cell starts with a homogeneous mean polarization field $\varepsilon = \varepsilon_0$, that will evolve over time and assign each hexagon a polarization value $\varepsilon \in [\varepsilon_0 - {}^{\Delta\varepsilon}/_2; \varepsilon_0 + {}^{\Delta\varepsilon}/_2]$, with $\Delta\varepsilon$ thus denoting the difference between maximal and minimal polarization. The change in polarization energy for the elemental event ϑ taking place at a certain cell site and a neighboring free hexagon is given by

$$\Delta\mathcal{H}_{cyto}(\vartheta) = \begin{cases} \varepsilon_{cell} + D_{cell} & \text{for } \vartheta = \text{retraction event.} \\ -(\varepsilon_{cell} + D_{free}) & \text{for } \vartheta = \text{protrusion event.} \end{cases}$$

Here, ε_{cell} denotes the polarization at the site of the elemental event ϑ, D_{cell} the confinement at this site and D_{free} the confinement at the site the protrusion invades into. The contribution to the probability accordingly is defined as above as

$$p_{cyto}(\vartheta) := exp\left(\frac{-\Delta\mathcal{H}_{cyto}(\vartheta)}{k_B T}\right).$$

As described at the beginning of the paragraph, the obtained probabilities $p_{cont}(\vartheta)$ and $p_{cyto}(\vartheta)$ are multiplied and the elemental event takes place with probability $p(\vartheta)$. A successfully invaded hexagon is assigned the polarity field value of the field of origin of the protrusion ε_{cell}.

The temporal evolution of the polarization field ε is discretized into MCSs and the regulatory field F keeps book of changes due to accepted elementary events ϑ. An important parameter here is the feedback radius R that describes how many neighbouring lattice sites the accepted event ϑ influences, illustrated in Fig 2.7. Initially, F is set to zero and updated by ϑ as follows

$$F_{\vartheta+1} = \begin{cases} F_\vartheta - 1 & \text{for } \vartheta = \text{retraction event} \\ F_\vartheta + 1 & \text{for } \vartheta = \text{protrusion event} \end{cases} \quad \text{in radius } R \text{ around event site.}$$

After all elementary events ϑ of one MCS have been performed, the polarization field ε is updated in dependence on F and an additional parameter μ, the cytoskeletal rate, that describes the speed of the polarization changes:

$$\varepsilon_{MCS+1} = \begin{cases} \varepsilon_{MCS} + \mu\left(\varepsilon_0 + {}^{\Delta\varepsilon}/_2 - \varepsilon_{MCS}\right) & \text{for } F > 0 \\ \varepsilon_{MCS} + \mu\left(\varepsilon_0 - {}^{\Delta\varepsilon}/_2 - \varepsilon_{MCS}\right) & \text{for } F < 0 \\ \varepsilon_{MCS} + \mu\left(\varepsilon_0 - \varepsilon_{MCS}\right) & \text{for } F = 0 \end{cases}$$

After update of the polarization field ε, the bookkeeping field F is set back to zero for all grid sites and a new MCS begins with the determination of the number of elementary events ϑ it will try to perform.

To clarify and illustrate the influence of the cytoskeletal rate μ on the temporal evolution of the polarization field ε, Fig 2.8 shows the change in ε for different values of the cytoskeletal rate μ in dependence on the bookkeeping field F.

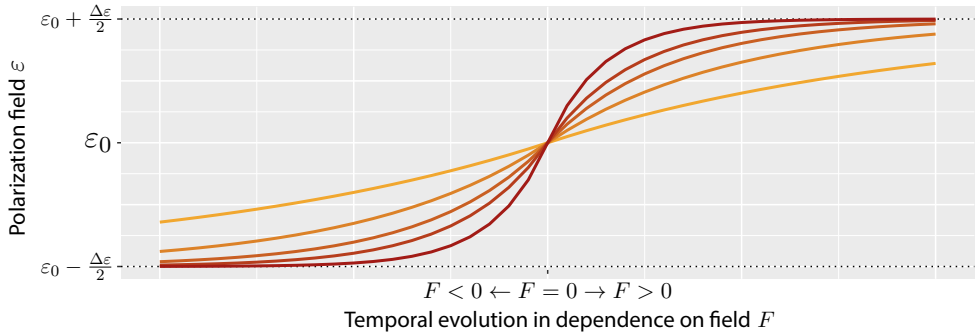

Figure 2.8.: Evolution of polarization for different values of μ. Starting at ε_0, the different colours illustrate the speed of change in polarization, i.e. position on the y-axis, for different values of μ from low (yellow) to high (red). Additionally, values of $F < 0$ of a hexagon lead to an temporal evolution of the polarization field towards the minimum, whereas $F > 0$ over time drives the polarization towards the maximum. Where $F = 0$, the polarization of the hexagon relaxes into mean polarization ε_0 (this is the case for all hexagons inside the cell body that are not reached by the signalling radius R).

Table 2.1 shows an overview of the parameters of the CPM relevant for this work. For a more detailed description of the model and additional features, please refer to [33].

Table 2.1.: Overview of the parameters used for single cell CPM simulations developed by [33].

Symbol	Parameter	Description
κ_A	area coupling	energy coefficient for number of hexagons inhabited by the cell
κ_P	perimeter coupling	energy coefficient for the cell perimeter
T	temperature	temperature used for scaling of probabilities, degenerated
D	adhesion penalty	adhesion penalty for each hexagon
ε_0	mean polarization	starting polarization of the cell
$\Delta\varepsilon$	polarization span	difference between maximal and minimal polarization
R	feedback radius	radius of adjacent hexagons influenced by elementary event ϑ
μ	cytoskeletal rate	speed of change in polarization

2.3.3. Single Cell Models

Earlier publications on single cells using CPMs included internal dynamics in the form of partial differential equations for key regulatory proteins such as Cdc42, Rac and Rho [31, 139]. They nicely produced broad gradients of these key players, but did not show the fast Rac-Rho dynamic at the cell front, that was experimentally reported around the same time [60]. Also, a very recent publication reported a Monte-Carlo based model for 3D cell structure containing cytoskeletal forces as well as curved membrane proteins [140]. A model including the Rho GTPase network of polarization with active and inactive forms of RhoA, Rac1, DIA, ROCK and PAK and their mutual regulation was recently published by Bolado-Carrancio *et al.* [141]. It focuses on the description of cell-internal fields by means of regulatory networks but does not model cell displacement or deformation. However, by abstraction of regulatory networks they show Rho-Rac oscillations at the cell front and Rho dominated contractility at the back as well as the propagation of waves of activity from cell front to back as observed in their experiments. A mechanistic option to describe single cell movement is the reduction to 1D lanes and the modelling and observation of cell lengths and protrusion dynamics [142, 143, 144]. In both, experiment and theory, cells confined to 1D lanes show a variety of movements that can be abstracted to springs connected to the substrate [142, 143, 145].

2.4. Micropatterning for Confined Cell Migration

In the scope of this thesis, cytoskeleton and morphodynamics of cells are quantitatively compared to models. An important experimental tool to access different modes of cell migration in a high-throughput and reproducible fashion is the confinement of cells to small structures of choice, micropatterns. Generally speaking, there are two fundamentally different approaches to confine cells. Either by two-dimensional surface structuring, defining areas of cell adhesiveness and cell-repellent areas, or by physically modelling a confinement in three dimensions. For two-dimensional confinement, there are three commonly used techniques: Microcontact Printing (μCP), Microscale Plasma-initiated Protein Patterning (μPIPP) and Laser-Assisted Protein Adsorption by Photobleaching (LAPAP). First proposed by the group of Whitesides at Harvard, μCP and μPIPP are techniques developed in the late 1990ies [146, 147]. Both techniques are based on a polymer stamp that moulds the desired structure often cast from a silicon wafer fabricated with classical laser lithography. In μCP, the stamp is incubated with the protein for cell adhesion and used to transfer it onto the surface. Then, the remaining uncoated surface can be passivated [148, 149]. In μPIPP, the stamp is used to protect a part of the surface from passivation that is afterwards incubated with a protein of choice [150]. The advantage of μCP is the possibility to fabricate hollow structures, e.g. a ring-shaped adhesive area, whereas micropatterns fabricated by μPIPP are visible in phase contrast and thus labelling of the adhesive protein with a dye is optional. As a more recently developed approach, LAPAP no longer relies on polymer stamps but instead uses classical photo lithography. A photomask, e.g. a chrome mask with transparent microstructures, is used to adsorb a fluorescent protein to a repellent surface by bleaching at UV-illumination [151, 152]. Then, a cell-adhesive sequence can be bound to the bleached protein via click-chemistry. An schematic overview of these fabrication protocols is given in Fig 2.9. The most commonly used protein for cell adhesion in micropatterning is fibronectin, a protein also present in the extra cellular matrix [153]. For passivation, coatings with polyethylen glycol (PEG) chains are widely used. They can be attached to poly-L-lysine backbones, resulting in PLL-PEG block-copolymers binding to the surface with PEG chains hindering attachment of cells and other proteins.

Experiments on cells confined by micropatterns have a broad application [154]. They can be used to keep single cells immobile, allowing for the investigation of translation kinetics [155, 156], signalling pathways [157, 158] or cytoskeletal properties in various different shapes [19, 159, 160]. When allowed to migrate, single cells confined to micropatterns allow the investigation of cell speed, persistence and polarization in dependence on environment [36, 161, 23] as well as the quantification of other migratory aspects particularly addressed by the specific geometry [162, 163]. The high flexibility in not only shape but dimensionality as well, make micropatterns a versatile tool to study cell collectives as well [17, 164].

For the confinement of collectively invading cell sheets, three dimensional patterns present an alternative to two-dimensional structures if channel shapes could lead to bridging of the sheet over passivated areas. This method has been as well proposed by the group of Whitesides [165] and cells are guided by an adhesive substrate and repellent walls, see Fig 2.9. During fabrication, a photo-polymerizable cell repellent, e.g. polyethylene glycol-dimethacrylate (PEG-DMA), is invading into the channels of a stamp and cured [166, 167, 168]. After stamp removal, the previously protected surface can be incubated with cell adhesive proteins that do not adsorb to the cell repellent PEG-DMA walls due to the steric hindering of the PEG chains.

All previously described techniques describe the structuring of rigid surfaces. There are as well protocols for micropatterning soft substrates, e.g. polyacrylamide, that allow the observation of migration on different elastic modules [169, 170]. Also, not only flat adhesive substrates can be structured but cells can be embedded in three dimensional confinement as well [171, 172, 173].

Concludingly, migration of cells presents a very rich phenomenology and confinement of cells by micropatterns can present a tool to disentangle different aspects of migration and provide a highly reproducible and well-defined experimental platform [174].

Table A.1 indicates the microstucturing techniques used in the different sections of this thesis.

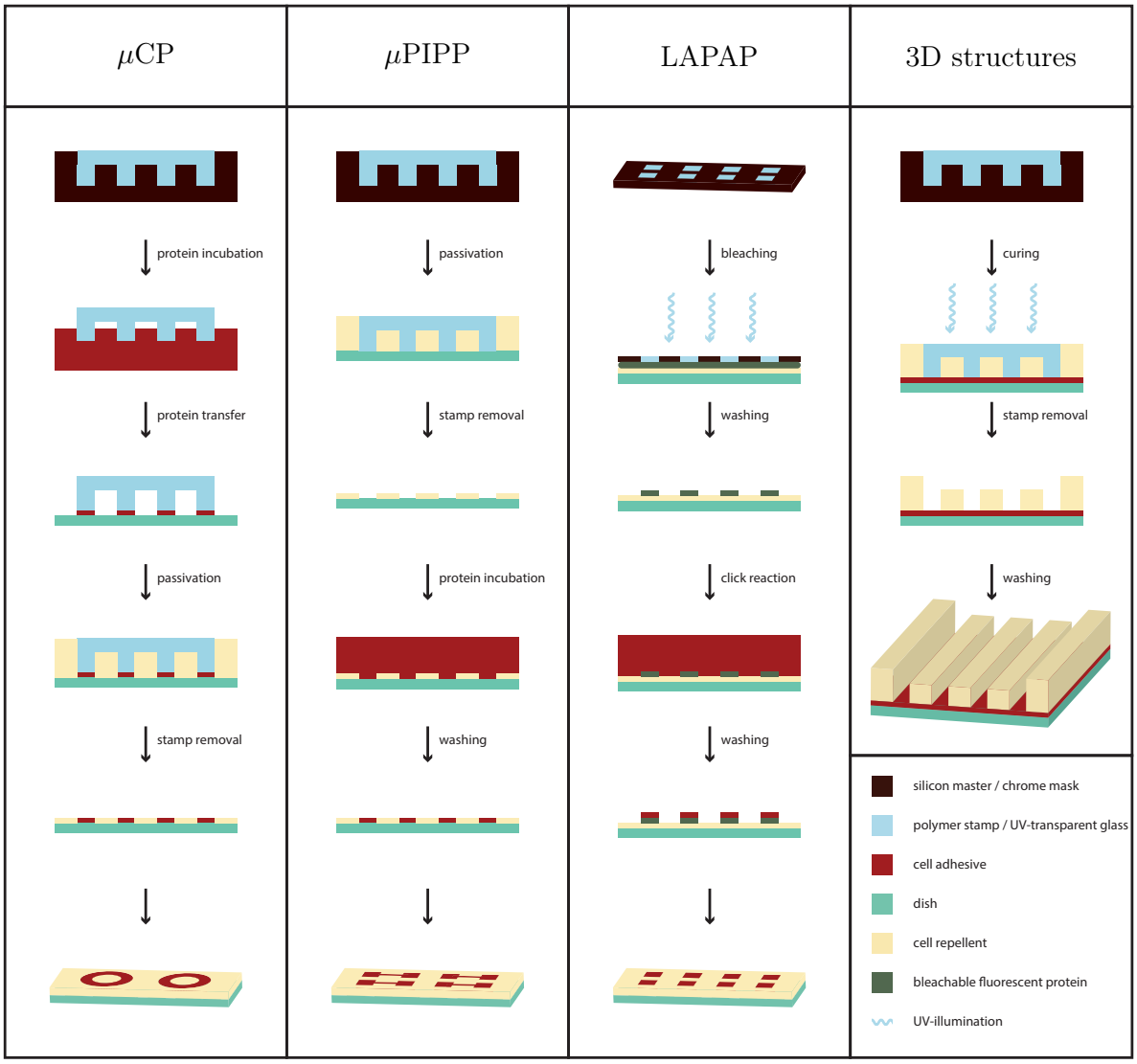

Figure 2.9.: Schematic overview of different micropatterning techniques: Microcontact Printing (μCP), Microscale Plasma-initiated Protein Patterning (μPIPP), Laser-Assisted Protein Adsorption by Photobleaching (LAPAP) and moulding of three-dimensional structures.

3. Spontaneous Polarization in Stripes

The first step of cell migration is polarization; either induced or spontaneous [35]. Stochastic fluctuations lead to spontaneous symmetry breaking and result in a formation of front and back end defined by distinct cell signalling events. The cell adapts a typical polarized morphology. Different mechanisms for polarization have been discovered [175, 176, 106]. An important aspect of polarization is the spontaneous quenching at contact with a boundary and the resulting dynamics of cell locomotion in absence of external clues. To investigate the dynamics of polarization, depolarization and repolarization, we use a confining geometry suitable to observe many of those events in a row; an adhesive stripe.
This chapter is published as Zhou, Schaffer *et al.* [136].

3.1. Quasi Oscillations of Cells in Stripes

On a short stripe-shaped micropattern, cell migrate along the longer axis in a periodic fashion, as shown in Fig 3.1.

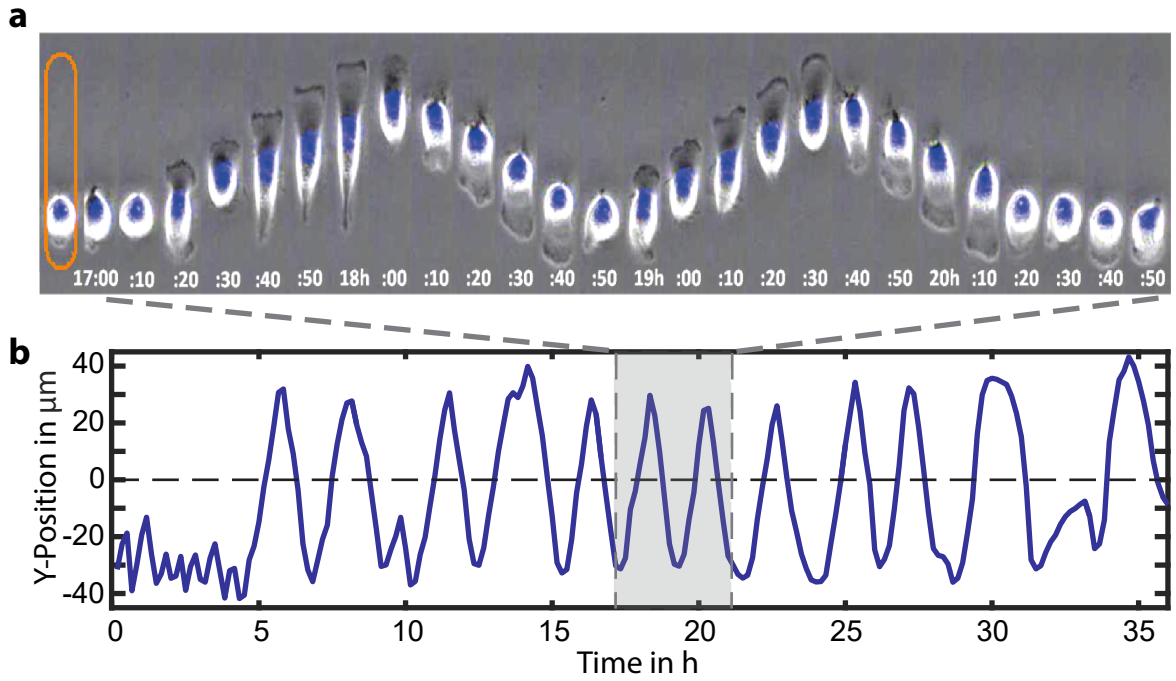

Figure 3.1.: Cell migration on a stripe micropattern. **(a)** Overlay of phase contrast and fluorescence images of a migrating cell with nucleus stain in blue at 10 min time resolution. Stripe micropattern of $20\mu m$ width and $120\mu m$ length indicated in first time frame in yellow. **(b)** Nucleus trajectory of this cell exhibits quasi oscillatory behaviour over 36 hour of observation.
Adapted and reprinted from [136] under (CC BY 4.0).

During migration, as shown in Fig 3.1a, we see a pronounced lamellipodium at the leading edge with dark ruffles at the very front and a slimmer retracting tail at the back. When the cell reaches the tip of the stripe, the cell shortens, depolarizes and repolarizes on the opposite site to redirect its movement along the stripe once more. This behaviour is stable over the whole 36 hours of observation during which every 10 min images were recorded. Fig 3.1b shows an exemplary nucleus trajectory of a cell migrating in a stripe of 120 μm length and 20 μm width. The trajectory shows up-down oscillations with repolarization phases of different lengths at the two ends of the stripe. Comparing the y-coordinate of the plot 3.1b and the fluorescently labeled nucleus in Fig 3.1a, we note that the nucleus does not reach the tip of the stripe and the lamellipodium elongates much further in front of it. Depolarization starts when the lamellipodium reaches the tip and thus the amplitude of the quasi oscillations may vary. Some spontaneous turning events in the middle part of the stripe are observed as well. Cells used in this experiment are MDA-MB-231, a highly invasive and motile breast cancer cell line, shortly described in section A. Cell position is accessed by tracking the nucleus that is stained with Hoechst 33342 over 36 hours of observation at an imaging rate of 10 min.

Oscillations are stable over different stripe lengths

To investigate the universality of cellular quasi oscillations in stripes, cells have been observed in stripes of different lengths of $120, 170, 220$ and 270 μm and constant width of 20 μm as shown in Fig 3.2. All recorded trajectories are shown as grey background and an exemplary trajectory for each stripe length is highlighted in blue. About one hundred trajectories have been recorded for each length. To distinguish phases of polarized motion from phases of reorientation, "reversal areas" are chosen such that the lamellipodia of cells not yet has touched the end of the stripe. They are indicated in blue areas of the stripes next to the trajectories and the areas are constant for all stripes. In the grey area of the illustrated stripes, cells are expected to mostly move persistently.

In this way disentangling motion and reorientation, the influence of length on the reversal times as well as on the velocity of polarized motion can be explored. Therefore, Fig 3.3a shows the velocity distribution in the centre part of the stripe, indicated in grey in Fig 3.2, for different lengths. Part b of the figure displays a plot of the distribution of reversal times for the different lengths. Insert display the corresponding absolute counts. The velocity simply is calculated by the displacement in y direction from one time point to the next for all observations starting in the grey area. We observe similar velocity distributions for all lengths. Taking into account the different amounts of observations underlying the densities, we conclude that the length of the stripe does not influence the velocity in the centre part. Corresponding conclusions can be drawn for the reversal times depicted in Fig 3.3b where the similarity of distributions is even

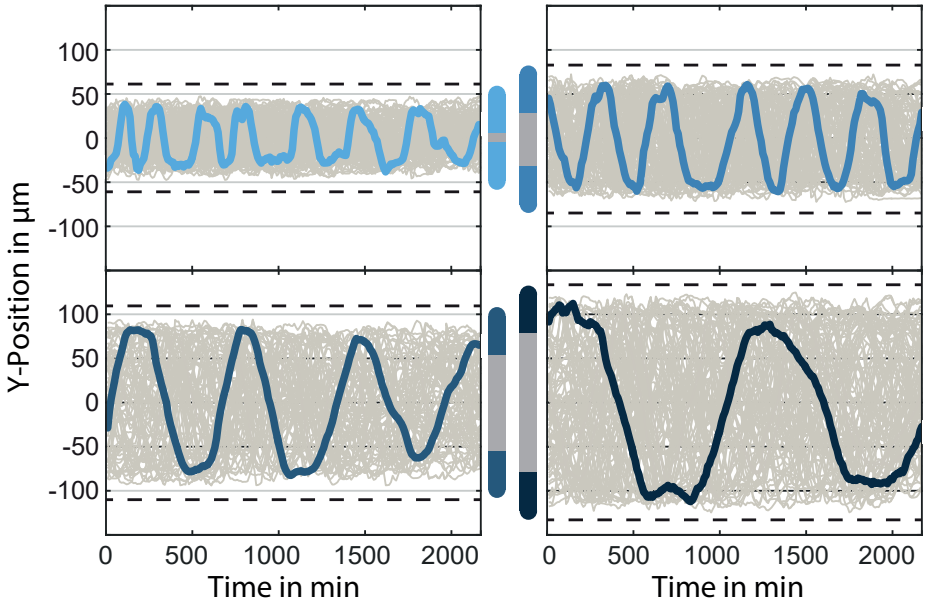

Figure 3.2.: Quasi oscillations in stripes of $120, 170, 220$ and $270\ \mu m$ length. All recorded trajectories are shown in grey background and an exemplary trajectory is highlighted in blue for each length. Trajectories were recorded over 36 hours at 10 minutes time interval.
Adapted and reprinted from [136] under (CC BY 4.0).

more pronounced. Thus, for all investigated lengths the cells do not show any fatigue, for instance by prolonged reversal times or by reduced migration velocities for long stripes. Predictions from theoretical models of oscillatory behaviour of cells in stripes can be confirmed [177].

Cellular Potts Model reproduces Oscillatory Movement

The versatile Cellular Potts model described in section 2.3.2, further referred to as CPM, has been successfully used to describe movement of small groups of cells in micropatterns [133] and single cells on substrates of different stiffnesses [135]. Combining a simplified biochemical Rac-Rho interaction model in form of a scalar polarization field with mechanical coupling via a constricting term, this hybrid model is a versatile tool for the description of cell migration. For a detailed model description, please refer to [33]. Here, time was calibrated by setting the average absolute velocity of cells in experiment $\langle |v| \rangle = 0.6 \mu m/min$ to equal the simulation. Starting from previous work [133], we revise the parameters to tune persistence, stochasticity and resolution of the cells to better resolve the tip of the micropatterns. Applying this model to the confining geometry presented here, we can see the emergence of oscillatory behaviour similar to experiment as illustrated in Fig 3.4. Looking at the simulated cell in panel a of the figure, we see the emergence of repeated up and down movement. The internal polarization field is depicted in a colour gradient from blue to green, showing short

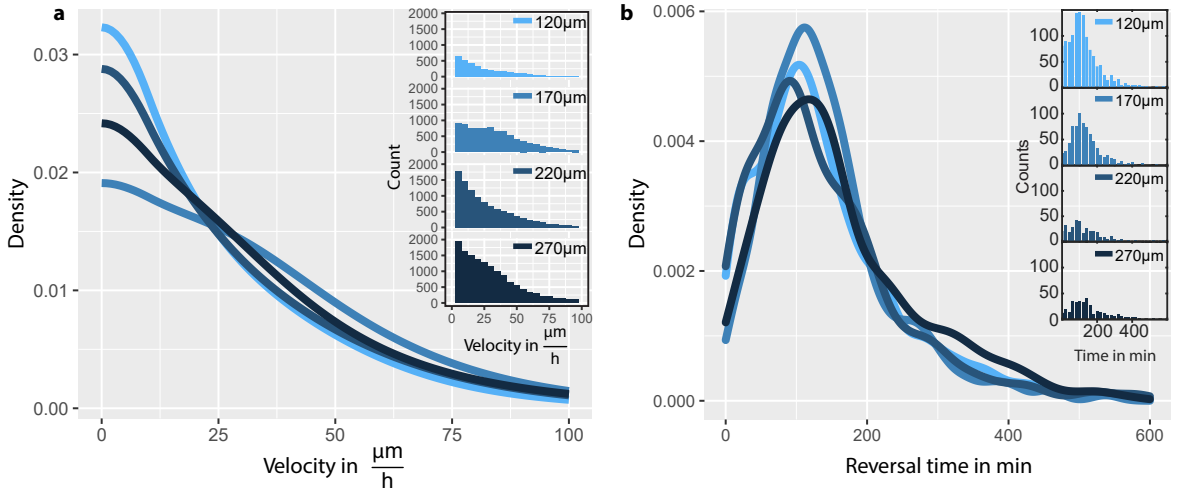

Figure 3.3.: Distributions of velocities and reversal times for different stripe lengths of 120, 170, 220 and 270 μm. **(a)** Colour-coded distributions of velocity in the centre part of the stripe and accordingly coloured inserts displaying count basis of the densities. **(b)** Colour-coded distributions of reversal times at the tip regions and accordingly coloured inserts displaying count basis of the densities. Adapted and reprinted from [136] under (CC BY 4.0).

periods in a depolarized state at the tips during reversal. We access the trajectory of the cell plotted in panel b by the centre of mass of the cell. This is a difference to experiment where the centre of mass of the nucleus is used for determination of cell position. Nevertheless, we assume the centre of mass to be a robust access to the cell position and well-comparable to the centre of mass of the nucleus. Taking a closer look at the trajectory in b, we see reversal events of different durations just as in experiment, making the model well-suited for further comparison.

3.2. Repolarization in Different Tip Geometries

As in experiment the length of the stripe does neither influence velocity nor reversal time, we use this reliable set-up to investigate the influence of curvature on reversing. Membrane curvature has been reported to play a role in many intracellular signalling networks including formins [178], BAR proteins [89], cell migration and polarization via MyosinVI, as described in section 2.2.2 and [46]. We choose geometries to address different types of curvatures, depicted in Fig 3.5. After having started with the most natural-seeming tip of a cell to migrate into, the round shape, we can think of the most simple curvature, namely no curvature at all, i.e. a blunt end. As many proteins are reported to be explicitly sensitive to positive versus negative curvature [89, 46], the next curvature of interest is the inverted round shape, a concave tip. As the most intriguing feature of this geometry are the two very pointed ends, another thing that come to mind is flip of the pointed ends, leading to a single, pointed tip presenting two negative curvatures to the cell. We adjust the stripe dimensions of the different geometries to

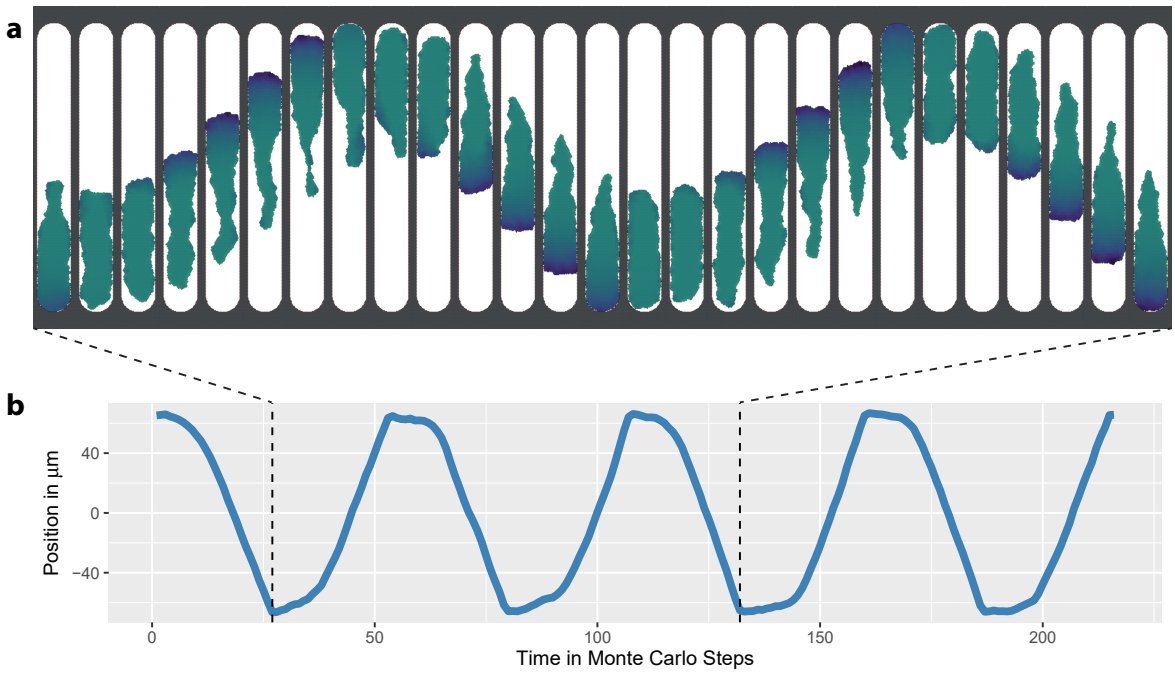

Figure 3.4.: Cell migration on a stripe micropattern simulated by the CPM. **(a)** Graphical output depicting the simulated cell. Colour gradient depicts polarization field. Time intervals were chosen to correspond to experimental time resolution. Stripe micropattern of 20μm width and 170μm length. **(b)** Centre of mass trajectory of the simulated cell exhibits quasi oscillatory behaviour and shows fluctuations in the reversal duration.

all have the constant width of 20 μm as used before and present constant reversal areas to the cells, resulting in varying stripe lengths labelled in the illustration.
From the different lengths with round tips, the stripe length of 170 μm has been chosen for further investigation as a good compromise between number of reversal events and time points outside the reversal areas.

Analysing the trajectories obtained accordingly to the experiments on different lengths of stripes, we see that the tip geometries seem to have little to no influence on reversal times as depicted in Fig 3.6. Panel (a) shows the velocity distributions in the centre part of the stripes for the different geometries coded in colour. The insert displays the corresponding counts. Mean velocities range from 34.7 $\mu m/h$ for the round tip to 41.1 $\mu m/h$ for the pointed tip, ranging within the expected scale, modulated by cell-to-cell variations. Reversal times plotted in panel (b) show even less variation for the different geometries. Although magnitudes of the densities do indicate slight differences, mean as well as median reversal times range within the temporal resolution of 10 min for all geometries.

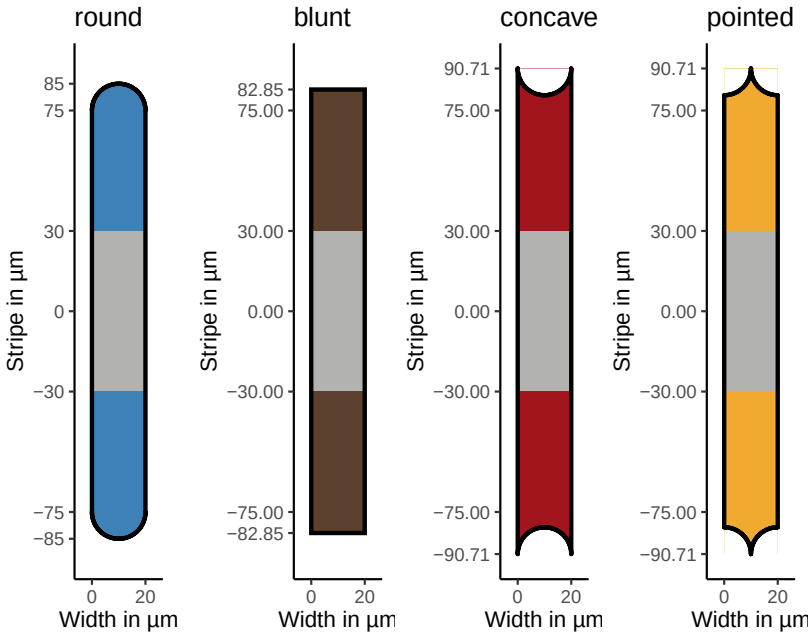

Figure 3.5.: Different stripes with annotated dimensions and reversal areas indicated in colour. The stripes are designed in a way to have a constant middle part and tips of the same area. All circular shapes used here have a radius of 10 μm and stripes have a constant width of 20 μm. Names and colours indicated here are further used for the different geometries.

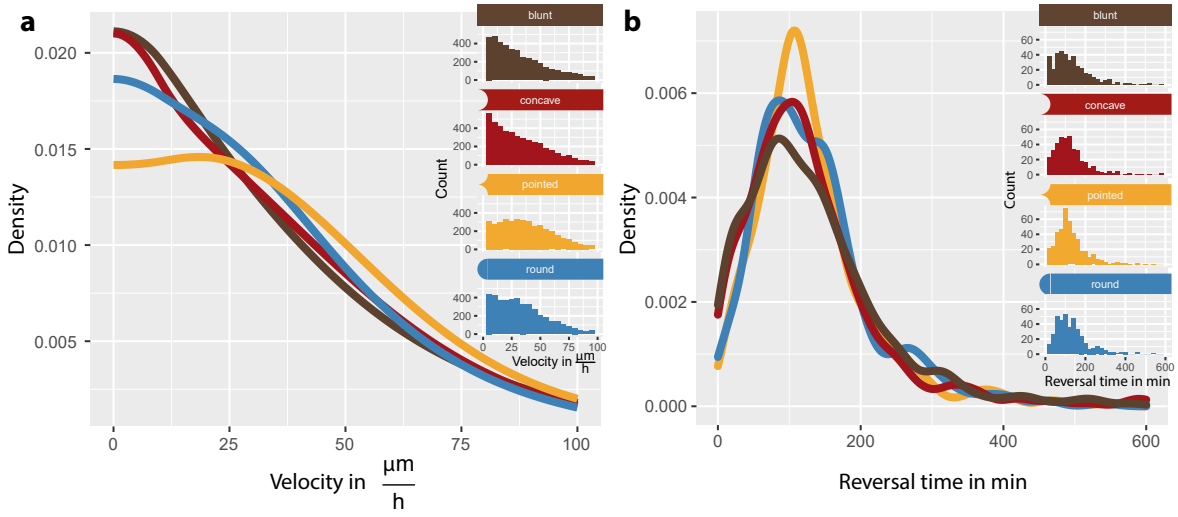

Figure 3.6.: Distributions of velocities and reversal times for different tip geometries. **(a)** Colour-coded distributions of velocity in the centre part of the stripe and accordingly coloured inserts displaying count basis of the densities. **(b)** Colour-coded distributions of reversal times at the tip regions and accordingly coloured inserts displaying count basis of the densities.
Adapted and reprinted from [136] under (CC BY 4.0).

3.2.1. Repolarization Time in Experiment and Simulation

The indifference of the cells to the presented tip geometries nevertheless is an intriguing effect in its negativity and presents an interesting basis for comparison with the CPM. Analysing the simulated trajectories analogously to experiment and adjusting time via velocity in the centre part of the stripe, we obtain densities compared in a violin plot in Fig 3.7. Simulated reversal time distributions are depicted in coloured contour coding for tip geometry and filled with white on top of experimental densities with solid contour and shaded filling. Density amplitudes between simulations and experiments are scaled by a constant to allow for better comparability. Now comparing the distributions of simulation and experiment, we can see a much less pronounced stochasticity of reversal of the simulations but nice agreement in peak position that is confirmed in mean and median values. The much narrower distributions for simulated cells are due to the nature of the modelling process where we simulated cells using different random seeds but the very same parameters, thus describing perfectly monoclonal cells but not including population heterogeneity as in experiment.

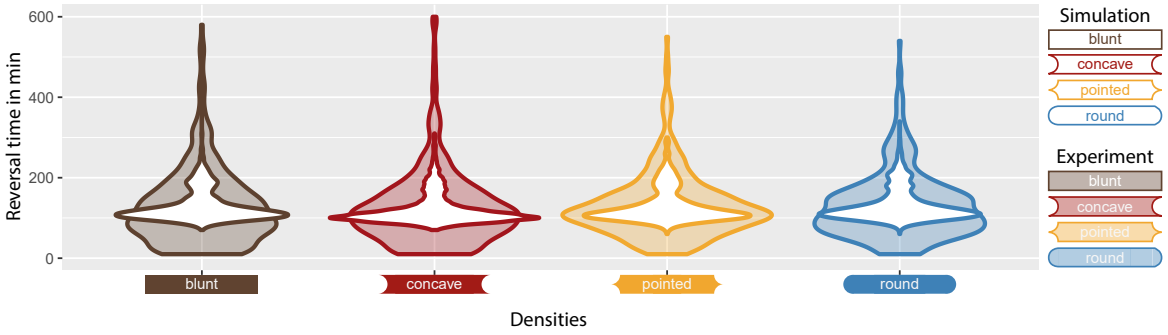

Figure 3.7.: Reversal time densities for experiment and simulation for different geometries. Densities are displayed in white with coloured contour for simulations and shaded for experiments. Furthermore densities are scaled by a constant factor between experiments and simulations to allow for better comparability.
Adapted and reprinted from [136] under (CC BY 4.0).

3.2.2. Actin Dynamics in Experiment and Polarization in Simulation

Although there is no difference for different tips in reversal times, the cells do encounter quite distinct geometries at the tip. Especially the depolarization as the cell reaches the end of the geometry presents an interesting phenomenon. To visualize this depolarization, cells were transfected with LifeAct GFP mRNA. Exemplary close-up images of F-actin distribution during depolarization are shown in Fig 3.8 in the top rows and compared to the polarization field of simulated cells displayed beneath. Panel a shows how actin polymerization in the blunt end stops equally distributed, similar to the

round tip in panel d. For concave shaped tips in panel b, we see how the lamellipodium splits into two small one that each advance into the pointed ends. In contrast, in panel c the altered negative curvatures in the tip lead to a focusing of F-actin activity in the pointed end. The polarization field in simulation is not as spatially narrowed and does not as clearly show either splitting or focusing. This may be due to the broader region of high activity in simulation simply not yielding a contrast big enough to show in the overall polarization, suggesting that polarization describing the level of the whole cell does not correspond to the microscopic actin activity on the subcellular level in detail. Furthermore, the cells in experiment often protrude into the area around the micropattern which is energetically not possible in simulation.

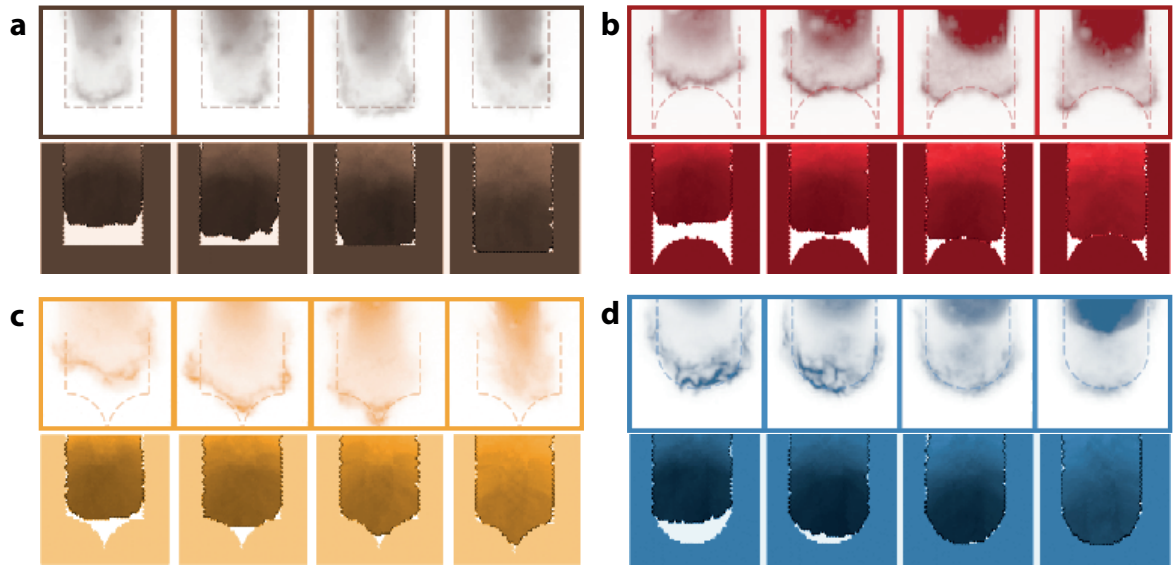

Figure 3.8.: Time series of cells in different geometries reaching the tip. Comparison between LifeAct-GFP transfected MDA-MB-231 cells in the top row and simulated data below for **(a)** blunt **(b)** concave **(c)** pointed and **(d)** round tips.
Adapted and reprinted from [136] under (CC BY 4.0).

3.3. Discussion

In this work, we analysed cell motion in confining stripes. Restricted to these stripes, cells show polarized quasi oscillatory behaviour along the long axis of the stripes. This motion can be characterized by the movement velocity and the reversal times in the tip regions. There, the leading edge encounters the end of the fibronectin coated adhesive surface and the begin of the cell-repellent PEGylated area that prevents the formation of focal adhesions and thereby stops further movement into this area. Presumably by this reduced capability of adhering, the cell depolarizes in this region and new protrusions are formed at the free edge on the opposite end of the cell. This phenomenon of quasi oscillation is stable for all investigated lengths and geometries, in accordance

with previous studies reporting on the persistence length to be much larger with about 400 μm [36, 21]. Interestingly, even the migration velocities and reversal times are found to be very similar for all geometries used in this study.
However, for different curvatures at the tip the microscopic details in actin distribution vary, indicating that protrusions into tapered constrictions are enhanced and can even split into two separate small ones. This microscopic differences and constant overall reversal time independently of geometry allow the conclusion that depolarization time scales are short compared to overall turning and repolarization at the opposite edge.
For a future study, one could also think about switching from 2D confinement to 3D. In this study, cells are solely able to "feel" presented curvatures via the position of substrate adhesions resulting in deformation of the membrane. The real 3D curvature of the leading edge often extends out into the PEGylated area "blurring" the curvature. Here, forcing the cell into a 3D confinement might lead to more pronounced curvature effects.

Comparison with the extended Cellular Potts model described in detail in [33] yields a possible explanation for stochastic reversal times, another indication of the model's capability to describe motion of cells: A cell randomly explores its vicinity and at successful adhering to the substrate, positive feedback reinforces the adhesions and promotes further polarization in the close surrounding area. At the tip, the inability of the cell to form new protrusions leads to a halt in positive reinforcement and the polarization fades or is actively quenched. At the same time, the cell still tries to form new adhesions in its surrounding leading to the inevitable formation of new adhesions on the free, opposite cell edge. With positive feedback, the cell repolarizes at this side leading to a full reversal. The main driving mechanism for quasi oscillatory motion in stripes thus can be reduced to the stochastic emergence and reinforcement of exploring protrusions of the cell. We will investigate the multifariousness of the Cellular Potts model in the next section.

4. Multi Geometry Calibration on Single Cell Trajectories

Cell migration is a complex process and the regulatory networks are highly intertwined [12] and precisely spatiotemporally controlled [60]. Confining cells to micro-structured environments has proven a versatile tool to specifically access intracellular organization [134], characterize single cell motion [162] or observe the dynamics of collective migration [92]. By restricting single cells to patterned surfaces, the naturally complex spatio-temporal dynamics is reduced and particular aspects of cell migration can be addressed such as persistence and speed of migration or reversal time for repolarization [36, 136]. Such kind of experiments are a useful basis for models. Here, we present a systematic approach to determine the full set of CPM parameters as presented in section 2.3.2 using a set of well-chosen experiments of single cells in defined geometries. The geometries accentuate complementary properties and facilitate a successive parameter determination. We demonstrate this "calibration" strategy using four data sets from a MDA-MB-436 cell line. It is furthermore shown that a calibrated CPM-cell will allow for predictive modelling of cell behaviour in novel geometries that have not been used in the parameter optimization.

4.1. Single Cell Geometries with Orthogonal Properties

We performed experiments in a set of four distinct geometries shown in Fig 4.1. Each geometry yields different measures of migration for a single cell. All experiments are performed with the same cell line, in our case MDA-MB-436, a cancer cell line that is shortly characterized in section A. In total, the experiments yield seven different observables as listed in Table 4.1 and at least one hundred cells are recorded per geometry.

Figure 4.1.: Cells in different confinements. Cell nuclei are stained with Hoechst and indicated in blue. **(a)** Cell in no confinement, **(b)** stripe with round tip (length 170 μm, width 20 μm), **(c)** ring-shaped micropattern (inner radius 40 μm, outer radius 60 μm), **(d)** ring with a cell-repellent gap (ring as c, gap width 13 μm). Figure tiles c and d adapted and reprinted from [162] under (CC BY 4.0).

The most simple geometry for two dimensional migration is a cell without confinement that freely moves on an adhesive substrate. From this case, we extract the unperturbed

cell area A_0. A simple, dimensionless measure for shape of a two-dimensional object is circularity O, relating area A and perimeter P via $O = P^2/4\pi A$. For a perfect circle, the circularity is equal to 1 and increases with rougher outline. Therefore, cells were stained with a cytosol marker and area and perimeter were extracted by a Python script and manually checked for miss-identifications as described in Appendix B.2. Futhermore, we observe cells to move in mesenchymal mode, i.e. with a clearly pronounced lamellipodium, an elongated cell shape and a slimming rear. This means, cells in experiment move along the long axis of their body, a phenomenon that often is not the case in CPMs and will also be used for parameter determination.
As presented in section 3, a stripe-shaped geometry is very suitable to study frequent arrest of motion and repolarization; a feature challenging to more mechanical descriptions of cell motion [143]. We analyse cells on stripes of a length of 170 μm with a round tip. Here, we extract the reversal time in the tip region t_{rev} and additionally the mean velocity v that is used for time calibration. Experimentally, microscopy data was automatically processed by a Python script detecting the pattern, rotating and cropping areas of interest and tracking the centre of mass of the stained nucleus as described in Appendix B.1. Afterwards, all extracted cell tracks were manually checked for miss-identifications.
Another geometry restricting cell motion to quasi one dimension is a ring-shaped confinement that has been previously suggested as a platform to compare cell migration via a "migratory fingerprint" [162]. To describe cell motion in such a circular confinement, the mean squared displacement MSD is particularly suited. Experimental trajectories were re-evaluated from [162].
A simple modification of the ring, introduced in [162] as well, allows access to another completely independent parameter. A gap in the ring shape provides the opportunity for investigation of cell protrusions into cell-repellent areas. To quantify the ability of the cell to overcome repulsion by the passivated area, the crossing probability over a gap p_c is well suited. Here a gap width of 8 μm is used and p_c is calculated by defining an area $\pm 40 \mu m$ around the gap and observing entry and exit side, i.e. crossing (c) or turning (t) and taking the ratio of event numbers $p_c = \frac{n_c}{n_c+n_t}$ with n_c the number of crossing and n_t the number of turning events. Experimental data from [162].

To facilitate later comparison with simulations, Table 4.1 gives an overview of the observables, their symbol of representation, the geometry they are extracted from and their value used for calibration.

Table 4.1.: Overview of geometries and extracted experimental observables from MDA-MB-436.

Geometry	No Confinement		Stripe		Ring	Gap
Observables	Area	Circularity	Velocity	Reversal time	MSD	Cross. Prob.
Symbol	A_0	O	v	t_{rev}	MSD	p_c
Calib. Value	733 μm^2	5.06	34.9 $\frac{\mu m}{h}$	90 min	-	35%

4.2. Determining Parameters of the Cellular Potts Model

Now that we have reduced cell migration in different confinements to their unique characterizing variables, we want to connect these observables with simulation parameters of a cellular Pott's model (CPM) as introduced in section 2.3.2. This hybrid model that combines a constrictive, mechanical term with an elastic term for polarization and adhesion is a versatile tool to abstract the complex processes underlying cell migration. In contrast to section 3, we want to stepwise derive model parameters by connecting them with experimental observables in one to one relations. As submodels of CPMs are meaningful in their own right, we start with a minimal set of parameters and increase complexity while further refining the cell. After each newly set parameter, we go back through all previous steps to ensure no aspect of migration is neglected arriving in a full set of parameters capable to reproduce cell migration in all geometries with the same set of parameters.
For the sake of brevity, in the plots of this section only the very first calibration of each parameter is depicted. A full overview of the parameter evolution during the process of calibration is given in Table 4.2.

4.2.1. Cellular Potts Model in Equilibrium

Starting with a minimal set of parameters for a cell adhering to a surface, we set the polarization field to the mean polarization ε_0 and do not allow temporal evolution. Thus, we set the following term to zero: the polarizability of the cell $\Delta\varepsilon = 0$, the feedback radius for protrusions or retractions $R = 0$ and the cytoskeletal rate $\mu = 0$ that describes how fast the cell polarizes.

As described in [33], temperature in this model is a degenerated parameter that scales the overall probability of a retraction or protrusion event to happen via $p(T) \propto \frac{-\Delta\mathcal{H}}{k_B T}$. Thus, we set it to an arbitrary value of $T = 40$.

The model is scalable to describe cells in different spatial resolutions and therefore we need to fix one more parameter to start from. We set the mean polarization to a starting value of $\varepsilon_0 = 1500$ and determine all other parameters in dependence on the mean polarization.

Micropattern set hexagon-to-micrometer scale

To set a spatial resolution of the hexagons, we use the confinement microstructures and choose a number of hexagonal tiles for representation that still allows for enough detail to describe the round tip of the stripe and introduce small gaps in the ring, as seen in Fig 4.2.

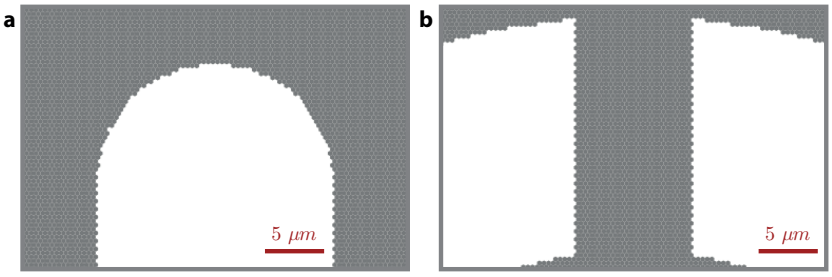

Figure 4.2.: Spatial resolution of hexagons determines level of detail in micropatterns. **(a)** Round tip of stripe structure. **(b)** Zoom in on the gap of the ring-shaped micropattern.

The area of all simulations is set to correspond to a square of 200 $\mu m \times 200\ \mu m$, represented by hexagons arranged in 460 columns and 530 rows[1]. This allows for direct transfer of area, perimeter and coordinates in simulation to experimental observables measured in μm^2, μm and Cartesian coordinates.

Area and Area Coupling κ_A

At equilibrium, the CPM shows no gradient in polarization and thus no polarization-driven movement. An easily accessible parameter of such a resting cell is the adhesion area. Here, the cell area is balanced by restrictive forces of the contractile term and elastic forces of the mean polarization. As we already set the mean polarization ε_0, we can now adjust the mechanical parameters that constrict area, the area coupling κ_A, and perimeter, the respective perimeter coupling κ_P. For simplicity, we first assume the influence of both to be equal, setting $\kappa_P = \kappa_A$ as their influence should be of the same order of magnitude. Thüroff *et al.* [33] determined the area coupling to be of major influence on cell size, so we first determine the area coupling κ_A to result in a cell area A_0 as observed in experiment. Therefore, we vary the area coupling κ_A and compare the resulting area to the experimental value. As a proportional dependence of area on the ratio ε_0/κ_A was reported, we expect a monotonously decreasing coupling between area and κ_A. The optimal value for κ_A is determined by spline interpolation with additional monotonicity assumption according to the method of Fritsch and Carlson [179] and depicted in Fig 4.3a.

As can be seen in Fig 4.3b, the variations in experimental cell sizes are much more pronounced than for simulations. This can be explained by a variety of reasons. Ex-

[1]These numbers are not the same due to the hexagonal grid of the model that lead to a different width than height

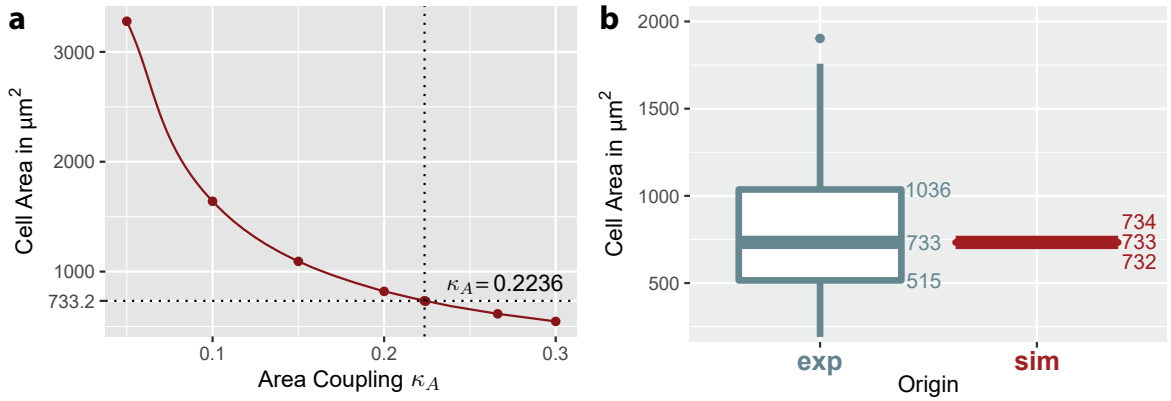

Figure 4.3.: Determination of area coupling κ_A by cell area A_0. **(a)** Dependence of cell area on area coupling, dashed lines indicate experimental mean area and interpolated κ_A.
(b) Boxplots of area distributions. Experimental data in blue, simulations in red. The filled box corresponds to the 25 to 75 percent quantiles and the median is indicated by the solid horizontal line.

perimental cells are no perfect monoclonal replicates of the same cell, whereas in simulation the exact same parameters are used. Furthermore, in experiment we didn't inhibit polarization for the determination of cell size, as this mostly results in a change in morphology resulting, for instance, in the rounding of cells. But the most reasonable explanation of the experimental variation in sizes is simply the fact that real cells divide after some time into two daughter cells of about half the size that again grow to divide. Thus, we approximate a cell cycle independent area by taking the median cell area and neglecting cell division in simulations.

4.2.2. From Equilibrium to Polarization

Allowing a small, localized polarization, we leave the non-motile equilibrium regime. Therefore, we set the cytoskeletal rate to the maximum value $\mu = 1$, resulting in a discrete three step polarization $\varepsilon \in \{\varepsilon_0 - {}^{\Delta\varepsilon}/_2; \varepsilon_0; \varepsilon_0 + {}^{\Delta\varepsilon}/_2\}$. The initial value of the feedback radius for protrusion and retraction events $R = 4$, corresponding to $\approx 1.8\ \mu m$, is motivated by the width of the membrane ruffles at the cell front. For the polarizability $\Delta\varepsilon$, we lack a biologically motivated starting point, so we determine its value as first migratory parameter.

Circularity and Polarizability $\Delta\varepsilon$

As the value of polarizability determines the outwards pushing force of the cell and the strength of adhesion to the substrate, we expect it to strongly influence the cell shape. Varying polarizability widely across its range of definition ($0 < \Delta\varepsilon < \varepsilon_0$), we obtain completely different cell shapes from almost circular cells to very rough and frayed ones.

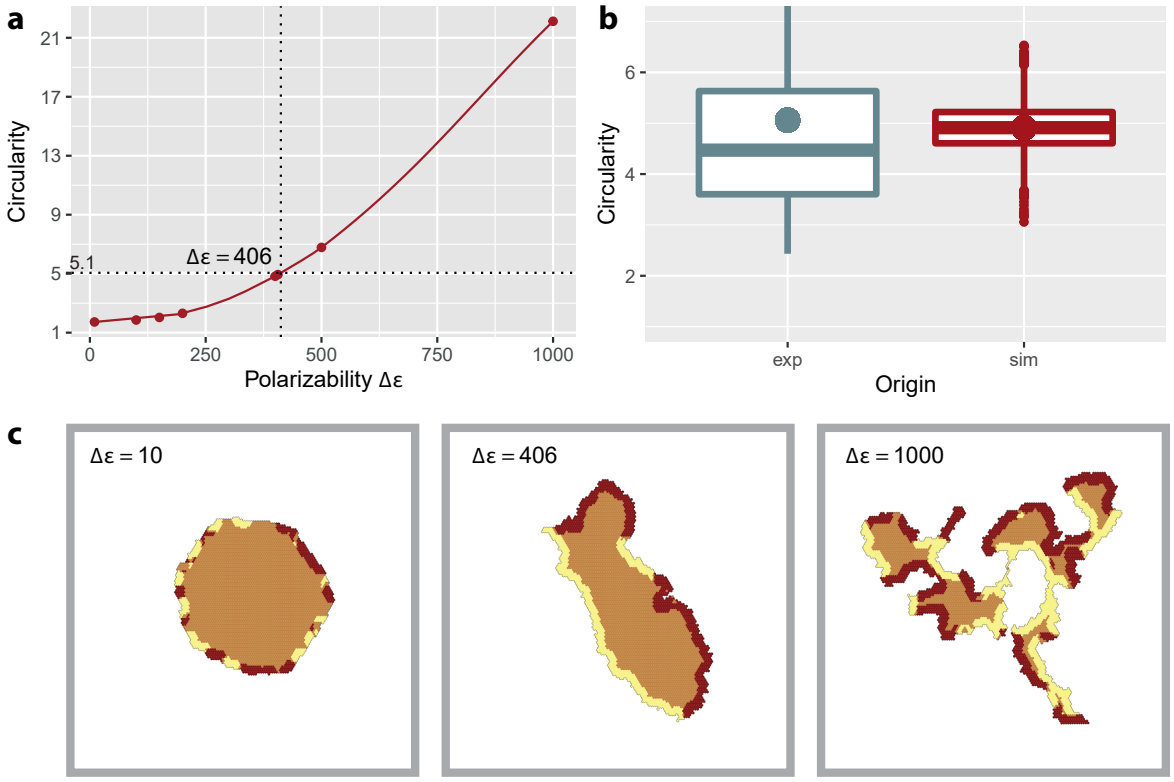

Figure 4.4.: Determination of polarizability $\Delta\varepsilon$ by circularity O. **(a)** Dependence of circularity on polarizability, dashed lines indicate experimental mean circularity and interpolated $\Delta\varepsilon$.
(b) Boxplots of circularity distributions. Experimental data in blue, simulations in red. **(c)** Exemplary images of simulated cells for different polarizabilities.

By tuning the polarizability as depicted in Fig 4.4, we fit mean circularity in simulations to experiment. First, depicted in panel a), we vary polarizability and interpolate the observed values of mean circularity as described for the area. Second, we compare the obtained distribution of circularities for simulation with the fit parameter and experiment and obtain nice accordance, see panel b). Panel c) shows cells for different polarizabilities to motivate circularity as a well-suited measure for cell shape.

This adjusted polarizability now describes the minimal adhesion energy of a cell before it detaches as well as the maximal protrusive force a cell can exert in simulation.

Reversal Time and Cytoskeletal Rate μ

So far, we only allow three different states of cell polarization, i.e. minimal $= \varepsilon_0 - {}^{\Delta\varepsilon}/_2$, mean $= \varepsilon_0$, and maximal $= \varepsilon_0 + {}^{\Delta\varepsilon}/_2$. As this does not at all capture important biological phenomena as for instance the slow process of depolarization, we aim to correct this description next. A geometry particularly suited to observe cell depolarization and repolarization is stripe shape already explored in section 3. The parameter describing the speed of regulation of polarization is the cytoskeletal rate μ that determines the number of intermediate polarization steps. As we now no longer compare time-independent cell observables, a method to connect simulation time, given in Monte Carlo Steps (MCS) and experimental time has to be established. To this end, we extracted the mean velocity of cells in the stripe from experiments and set it equal to the velocities observed in simulation. As both velocities contain the displacement in μm, we obtain a factor for time calibration that calculates to 0.00689 ${}^{\text{h}}/_{\text{MCS}} = 0.4134\ {}^{\text{min}}/_{\text{MCS}}$. By applying this factor to the reversal times, extracted as in section 3, we obtain simulated and experimental reversal times in minutes. Then we investigate the evolution of median reversal time t_{rev} in dependence of the cytoskeletal rate μ, see Fig 4.5a. To this end, we model the median t_{rev} with a quantile-regression spline fitted by the R package mboost [180]. The distributions of experimental reversal time and adjusted simulation are depicted in panel b) and nicely correspond.

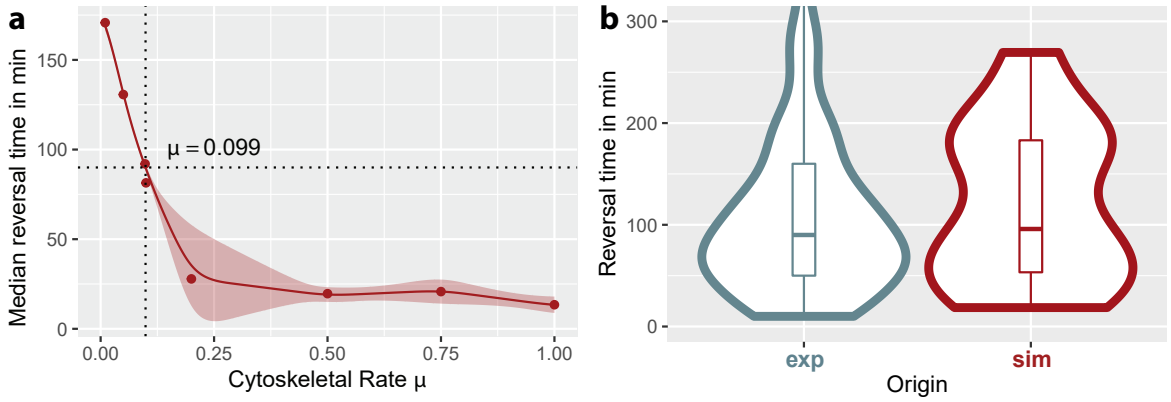

Figure 4.5.: Determination of cytoskeletal rate μ by reversal time in a stripe. **(a)** Evolution of reversal time in dependence on cytoskeletal rate. Dots show medians of simulations. Dotted lines indicate the experimental median t_{rev} and selected μ. Solid line depicts the fit and shaded regions correspond to $\pm$ 2 se, i.e. standard error obtained by 999-fold bootstrapping. **(b)** Resulting reversal time distributions after parameter adjustment.

Directionality and Signalling Radius R

After adjusting the first parameter in a second geometry, we take a step back and observe the behavioural changes for a cell without confinement. Area and circularity are barely changed. However, simulated cells without confinement no longer show typical polarization behaviour of two or more competing protrusions and an elongated shape in the direction of movement but rather a keratocyte croissant-like shape. An additional observable describing the cell shape in dependence on the direction of motion needs to be introduced to ensure correct cell behaviour in periodic boundary conditions without confinement. This dependence can be quantified by the angle between the long axis of the cell and the direction of movement, termed d. A frequent observation in CPMs is the keratocyte-like cell shape that here contrasts the reported elongated shape of cells in experiment [181]. Although not extracted from experiment, the angle can be calibrated by minimizing it in simulation. Here, we turn to the signalling radius R as feedback mechanism of protrusion. We vary R to minimize the angle between long axis of the cell and movement direction of the cell and discover a bi-phasic behaviour plotted in Fig 4.6. Investigating both areas of local minima, $R = 1$ and $R \geq 30$, we discover a "dead-end" for the latter as for the stripe geometry the extrapolated optimum of μ exceeds the maximum of $\mu = 1$. Furthermore, at $R \geq 30$ cells no longer move in a random walk like fashion but spiral in circles. This phenomenon of circular motion has been previously reported for cells reacting to a chemo-attractant [31], but in the case presented here is caused by a feedback radius that covers a comparably large part of the cell. The respective feedback radius is indicated in panel b) of Fig 4.6 as solid grey hexagon.

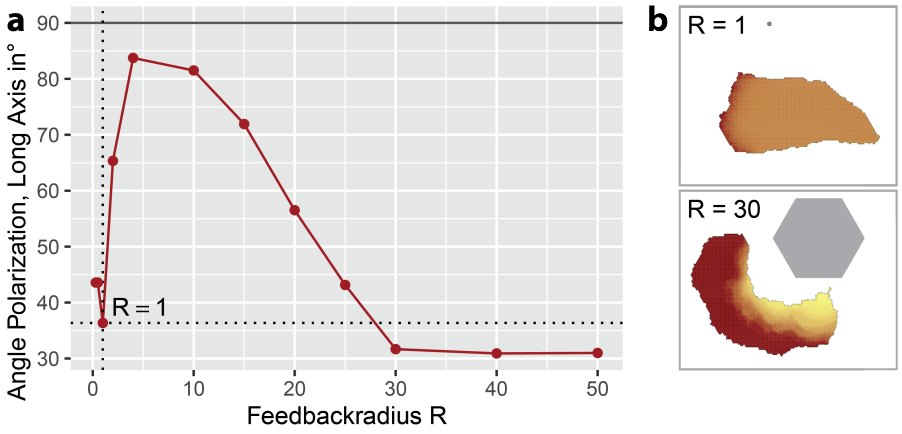

Figure 4.6.: Determination of signalling radius R by angle of polarization and the long axis of the cell. **(a)** Mean angle for different signalling radii. **(b)** Typical cell shape for two different signalling radii with respective R indicated as solid grey hexagon.

Having minimized d setting $R = 1$, we re-calibrate the previously determined parameters and arrive at a set of parameters that is capable of describing all observations so far at the same spatial and temporal resolutions as stated earlier.

Mean Squared Displacement and Perimeter Coupling κ_P

So far, we equally weighted area coupling and perimeter. Whereas area coupling κ_A has a quite intuitive influence on area as we saw before, the perimeter coupling κ_P is more difficult to grasp. Thüroff, Goychuk *et al.* [33], have unravelled an important relation where the persistence time of motion increases monotonically with the ratio of polarizability $\Delta\varepsilon$ and perimeter coupling κ_P. Using the ring-shaped lane geometry, we want to fine-tune this ratio via the mean squared displacement (MSD) of a cell as function of time. Time is using the same factor of 0.4134 $^{\text{min}}/_{\text{MCS}}$ applied before. Thüroff, Goychuk *et al.* [33] furthermore showed that this ratio consistently determines not only persistence time but aspect ratio as well. We thus knowingly compromise between circularity and MSD by changing κ_P. To measure the distance to the experimental MSD curve, we employ the Sobolev distance induced by the L^2 norm applied to $f(t) = \log(\text{MSD}(\log(t))$ and its first derivative $\dot{f}(t)$ [182]. The log-log-scale is the standard scale for interpreting MSDs and the Sobolev distance reflects both absolute values and slope of the curve. The distance is discretized at the experimental 10 min sampling rate and minimized as depicted in Fig 4.7.

In Fig 4.7b, we see that experimental MSD shows a transition behaviour in scaling from $MSD \propto \tau^2$ to $MSD \propto \tau$, indicating a transition from more ballistic to diffusive behaviour. For simulation data, this effect is not as pronounced. Although a clear transition from ballistic to diffusive motion has been reported in [33] for a freely moving cell, we don't see this effect as clearly in a ring shaped micropattern. Nevertheless, as shown in Fig 4.7c, we do see random turning events for $\kappa_P = 0.3352$, an important feature for migration in a ring-shaped micropattern. The chaotic trajectory for $\kappa_P = 0.1$ can be explained by looking at the cell images in Fig 4.7d. For small values of κ_P, the cell looses coherence and several cell segments, connected by thin membrane tubes, move almost independently. This is a biologically not reasonable behaviour. The simulation still returns the calculated centre of mass that no longer adequately describes the cells and leads to a chaotic trajectory. For $\kappa_P = 0.4$, we see completely erratic movement and the cell barely polarizes at all. This may indicate that the ratio of polarizability $\Delta\varepsilon$ and perimeter coupling κ_P already is too big and the behaviour reported by Thüroff, Goychuk *et al.* [33] may change in a ring-shaped confinement compared to a freely moving cell.

By tuning the parameter coupling κ_P, we achieve cell motion reproducing spontaneous turning events while maintaining the mean aspect ratio within reasonable range of experimental observations, compare Fig 4.9c.

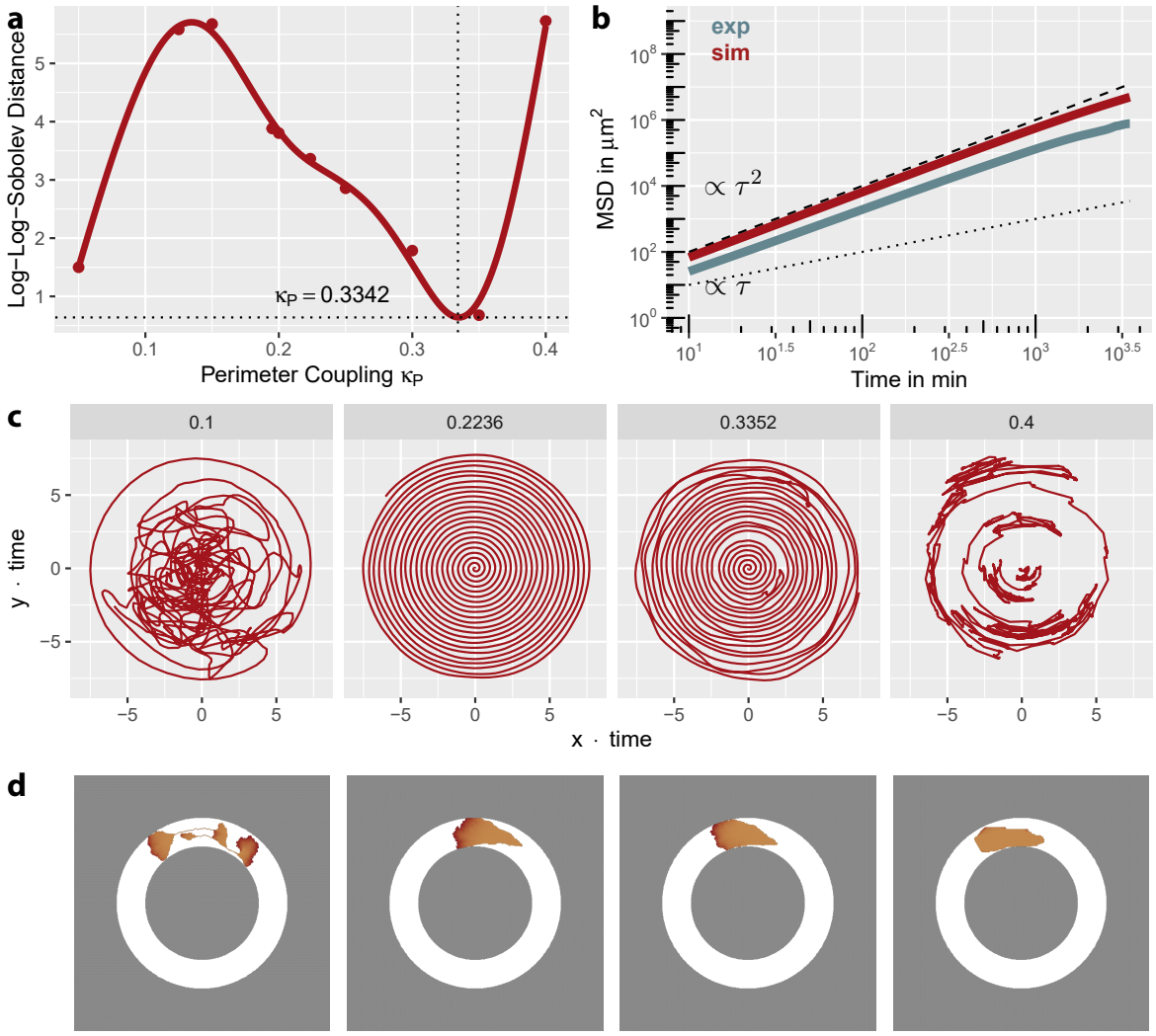

Figure 4.7.: Determination of perimeter coupling κ_P by mean squared displacement in a ring. **(a)** Log-log Sobolev distance of simulations with different κ_P to experiment. **(b)** Mean square displacement trajectories in a ring for experiment (blue) and simulation with best fit (red). **(c)** Spiral plots, where radius of motion is increased over time, for different κ_P. **(d)** Corresponding image of a simulated cell in a ring.

Transition Probability and Adhesion Penalty D

So far, in simulations the cell was exclusively confined to the micropatterned structure. In experiment, the micropattern consists of a fibronectin coated surface and the surrounding area is passivated by PLL-PEG that should not allow for cell adhesion [150]. However, cells can extend into this area and overcome a small repellent space [162]. Using a ring with a gap, we tune the strength of repulsion by the energy penalty field D that directly feeds back into polarization as described in section 2.3.2. We link it to the crossing probability p_c over a 8 μm gap, as shown in Fig 4.8.

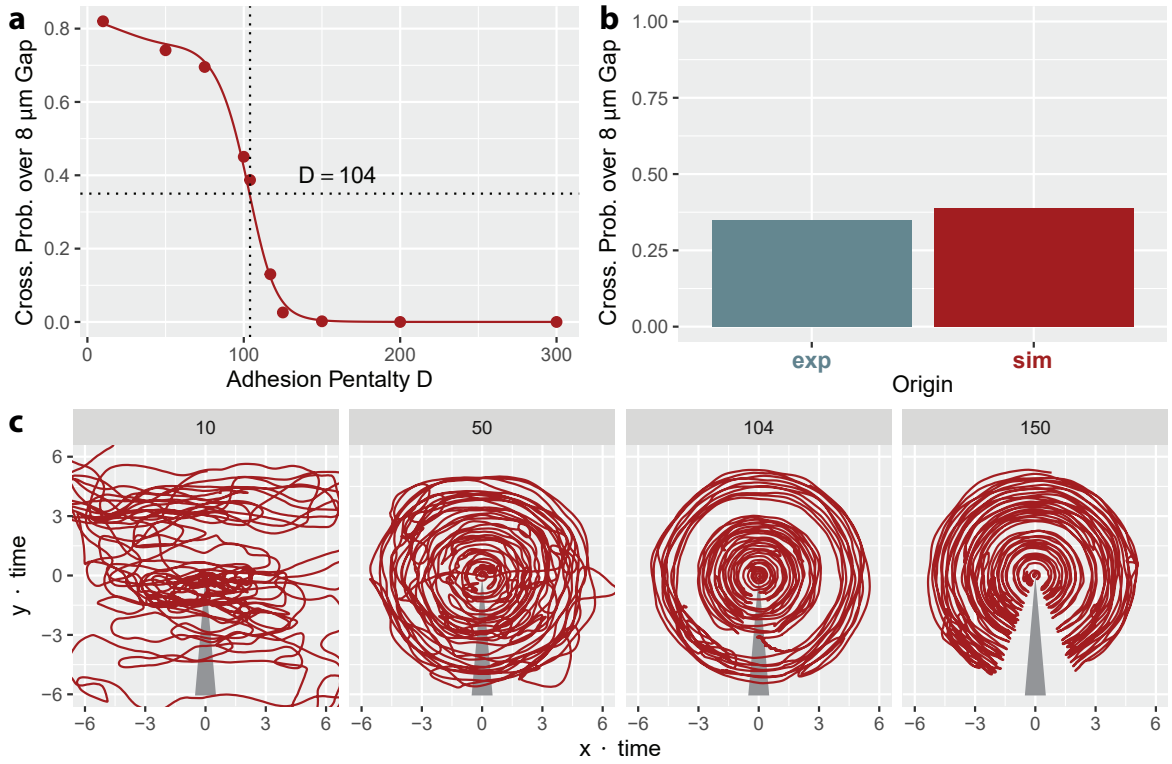

Figure 4.8.: Determination of adhesion penalty D by crossing probability over a 8 μm gap in a ring. **(a)** Crossing Probability for different adhesion penalties D and best fit to experimental data, indicated by dotted lines. **(b)** Crossing probability in experiment (blue) and adjusted D for simulation (red). **(c)** Spiral plots, where radius of motion is increased over time, for different D, gap indicated in grey.

Exemplary trajectories for different penalties D are plotted with radius of confinement increasing with time, as already used for mean squared displacements. The position and width of the gap is indicated in grey. For very small adhesion penalties, compare $D = 10$, cells are no longer confined to the ring shape but move rather freely, leading to a no longer reasonable definition of crossing probability. For intermediate values, see $D = 50$ and $D = 104$, the cells are nicely confined and crossing and turning events can be observed. At high penalties $D > 150$, the cells no longer cross the gap but turn when their front reaches the repellent area. By estimating the crossing probability p_c with logit-regression as depending non-linearly on a spline of D, we find the optimal value for the adhesion penalty field to be $D = 104$.

4.3. Calibrated CPM and Predictive Power

After iterative calibration of single parameters, we arrive at a set of parameters that is suited to describe cell migration in four different geometries simultaneously, as depicted in Fig 4.9.

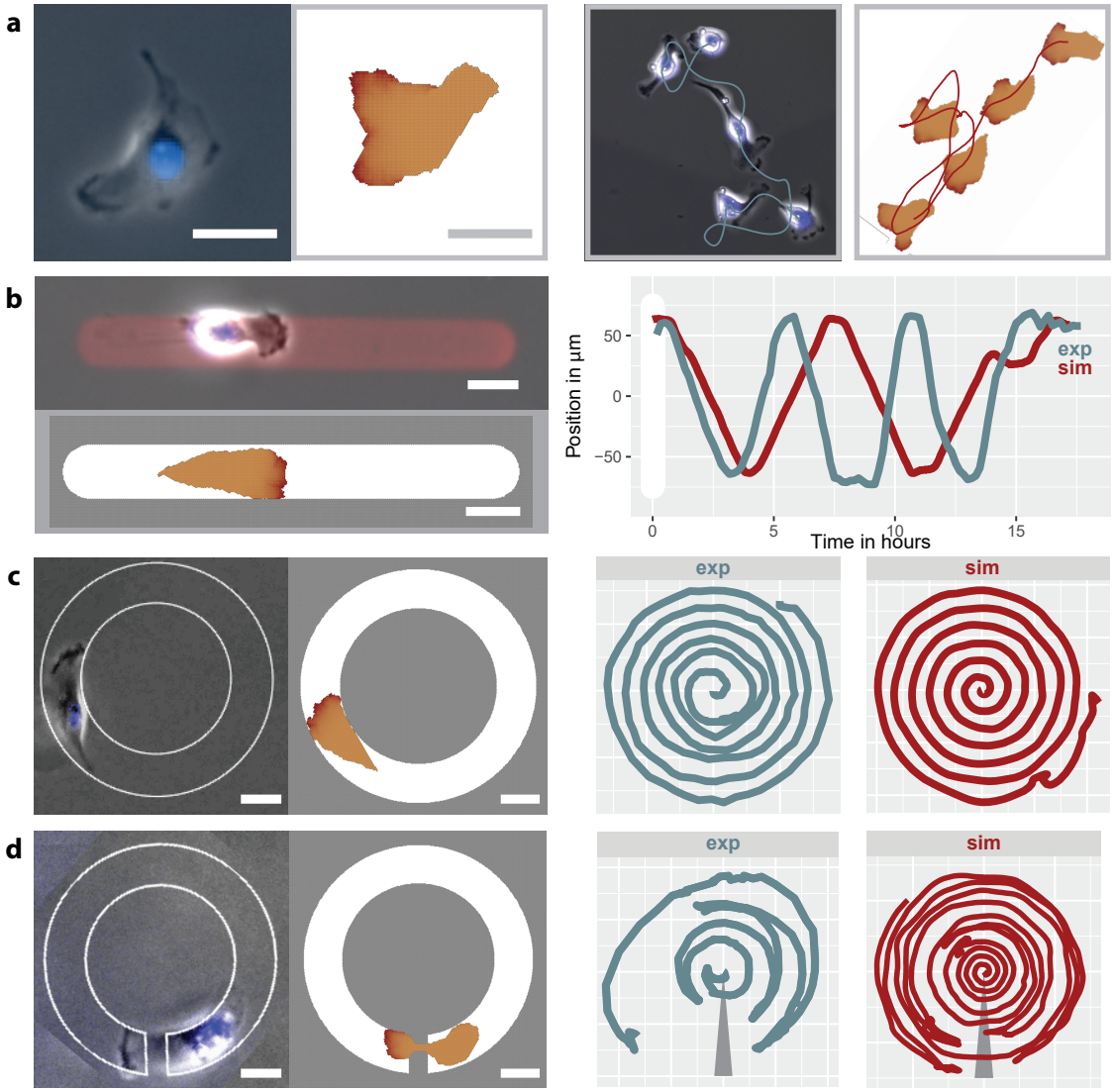

Figure 4.9.: Comparison of experiments (blue) and simulation (red) with fully calibrated set of parameters. Scale bars correspond to 20 μm. **(a)** Cell without confinement, cell shapes on the left, exemplary trajectories on the right. **(b)** Cell in a stripe, typical cell image in confinement on the left, exemplary trajectories along the long side on the right. **(c)** Cell in a ring, typical cell image on the left, spiral plots with radius of motion increased over time on the right. **(d)** Cell in a ring with 8 μm gap, image during crossing on the left, spiral plots with radius of motion increased over time and gap indicated in grey on the right.

We conclude that the CPM is capable to reproduce different migratory behaviours in four distinct confinements with one carefully obtained set of parameters. Experiment

and simulation match in following aspects: Cells without confinement show multiple competing protrusions and frequently change direction of migration. Their shape is elongated along the main movement direction and shows a broader front and a slimming rear. In a stripe, cells migrate from one end to the other in an oscillatory manner with reversal times of different lengths at the ends. There, they completely depolarize and spontaneously repolarize. In a ring-shaped confinement, cells show quite persistent motion but also turning events occur and the direction of migration reverses. Cells encountering a repellent barrier in a ring show crossing as well as turning events at the barrier and spontaneous reversal of migration anywhere on the ring. As all previous geometries were re-evaluated after each new step, we developed a consistent description of a cell in different micro-environments. The parameter evolution is summarized in Table 4.2. Note that due to the careful optimization using nested models and independent observables only one recalibration of parameters was needed when proceeding to a subsequent step.

Table 4.2.: Overview of experimental observables and parameter development used for single cell CPM simulations. Rows: Simulation Parameters. Columns: Steps in Calibration, labelled by experimental observables used in this step, calibrated parameter bold.

Parameters	Experimental Observables					
	A_0	O	v_{exp}, t_{rev}	dir	MSD	p_c
T	40	40	40	40	40	40
ε_0	1500	1500	1500	1500	1500	1500
κ_A	**0.2236**	0.2236	0.2236	0.2236	0.2236	0.2236
$^{\text{min}}/_{\text{MCS}}$	-	-	0.4134	-	0.4134	-
$\Delta\varepsilon$	0	**406**	406	834	834	834
μ	0	1	**0.099**	0.077	0.077	0.077
R	0	4	4	**1**	1	1
κ_P	$= \kappa_A$	$= \kappa_A$	$= \kappa_A$	$= \kappa_A$	**0.3352**	0.3352
D	∞	∞	∞	∞	∞	**104**

Predictive Power for a Dumbbell-shaped Confinement

We now challenge the CPM by introducing a new geometry, a dumbbell-shaped micropattern that has been previously used to characterize migration [26].
Fig 4.10 depicts a comparison of experiment and simulation with the calibrated CPM. The panel Fig 4.10a shows the localization of cell nucleus in experiment and centre of mass in simulation, already indicating differences. In experiment, cells spend most of the time on either side of adhesive squares whereas in simulation cells seem to get stuck on the bridge connecting the two islands. This is confirmed by the plot of experimental trajectories in Fig 4.10b. However, if migration is simplified to hopping rates from one

side to the other, the differences seem less pronounced, compare Fig 4.10c. A possible reason for deviations is the simplification of cells to two dimensions that is of particular interest when cells move over the bridge. In experiment the cell does not need to deform much but simply ”hovers“ over the bridge whereas in simulation, cells seem to get stuck due to energy penalties on membrane deformation and adhesion outside the bridge leading to unpolarized cells trapped on the bridge. In conclusion, the calibrated CPM is capable of reproducing qualitative migratory phenomena, such as the hopping of cells from one island to another, but differs when migration is quantified.

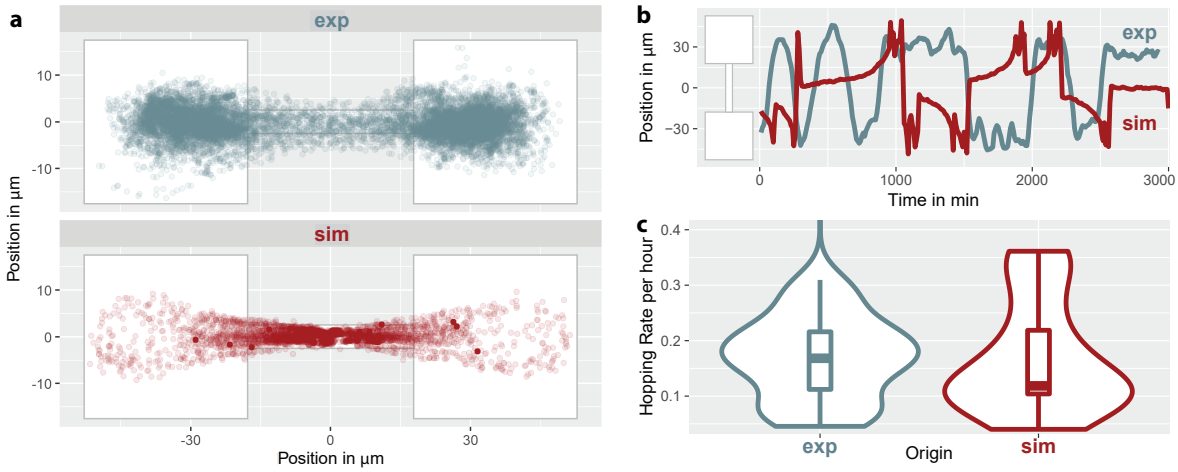

Figure 4.10.: Predictive capability of calibrated CPM and comparison in a dumbbell micropattern. **(a)** Position of cell nucleus in experiment and centre of mass in simulation on a dumbbell. **(b)** Exemplary trajectories for experiment (blue) and simulation (red) along the long side. **(c)** Distribution of hopping rates for experiment (blue) and simulation (red). Experimental data provided by Alexandra Fink.

Predictive Power for Different Tip Geometries

As the calibrated CPM is capable to reproduce cell behaviour in various geometries quantitatively and predict it qualitatively in dumbbells, we challenge this model with the tip geometries investigated in chapter 3. There, the model correctly reproduced the invariance in reversal times. However, when we compared the polarization field of the model with a LifeAct marker visualizing actin at the leading edge while the cell encountered the differently shaped ends of the stripes the model did not show some features such as the splitting of lamellipodia in concave tips. Here, we used the fully calibrated CPM to simulate these geometries again and observed the polarization field at encounter with the end of the lane as shown in Fig 4.11. For comparability, the experimental pictures from chapter 3 are again depicted next to the images of simulation. With the fully calibrated CPM, the polarization field shows the behaviour we observed experimentally. At the blunt end, polarization is evenly quenched. For cells migrating into the concave tip, the active region splits into two parts as polarization

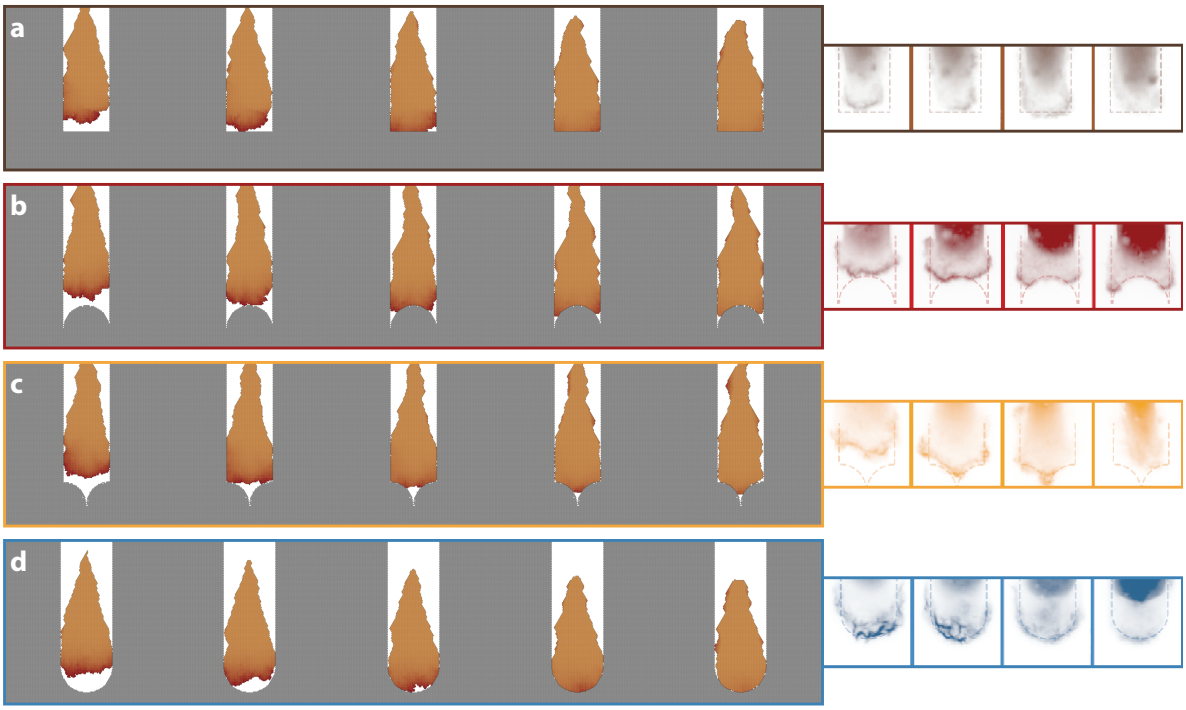

Figure 4.11.: Correct reproduction of actin distribution in different tip geometries by the polarization field of the fully calibrated CPM. LifeAct stained actin distributions obtained in experiment shown in colour next to simulated images of the same geometry. **(a)** Quenching of actin activity in a stripe with blunt end. **(b)** Splitting into two tips for negative curvature. **(c)** Focussing into the pointed end. **(d)** Centred quenching in the positive curvature.

is quenched first in the centre. For a related geometry, a protruding concave tip, polarization is persistent in the tip although the cell in simulation is more confined to the pattern than in experiment. In the round structure that has already been used during calibration, polarization is quenched rather evenly and a last active part is visible in the centre although it is not as clearly defined as for the protruding concave tip. Here, stepwise calibration has lead to a parameter set that, unlike the simulations presented in section 3.2, is capable to reproduce even details in the actin distribution while maintaining accordance to experiment in all other geometries used.

4.4. Discussion

In this chapter, a method for parameter optimization of a CPM is proposed, tested and extrapolated. Using experiments on confinement geometries evoking different migratory properties, model parameters are determined in a step-wise process. Explicitly defined observables and distance measures for comparison between experiment and simulation guarantee transparency and reproducibility. Statistical modelling was used to approximate objective functions at, yet, unevaluated sites, yielding guidance for parameter space exploration. Starting from a minimal set of parameters, determination of new

parameters and re-checking already calibrated ones leads to a continuously improved accuracy for cell representation, shown for the freely moving cell in Fig 4.12. In the end, all experiments are nicely reproduced with a single set of parameters both qualitatively in terms of cell shape and trajectories as well as quantitatively determined by the established accuracy measures. However, the possibility of another even more suited parameter cannot be ruled out, as two starting parameters were determined *a priori* and not changed throughout the process. Furthermore, the parameter optimization guided by statistical modelling could be further refined and reconceptualized in the sense of model based (Bayesian) optimization [183]. This approach is particularly suitable for costly objective functions involving for instance the conduction of experiments or computationally expensive simulations.

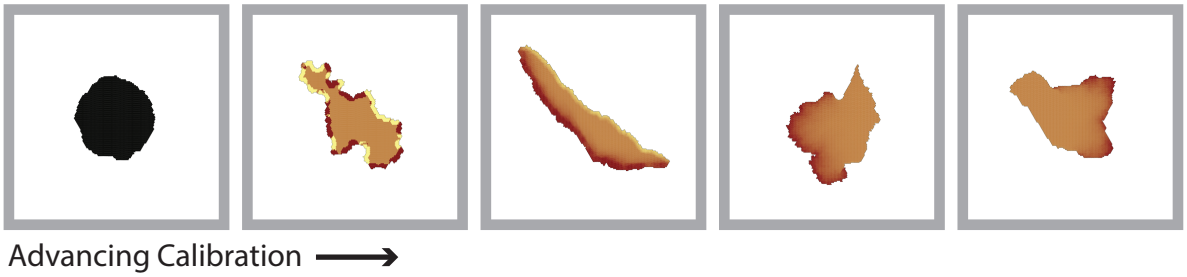

Figure 4.12.: Images of free cell with advancing calibration from left to right.

Applying the fully set parameters to a new geometry, a dumbbell-shaped microstructure, the model shows even predictive capability on a phenomenological level. Predictions of hopping motion between the two adhesive sites are observed in experiment as well. When experiment and simulation are compared on a quantitative level, the limits of the model become apparent and hopping rates in simulation are about a factor of two smaller than in experiment. This discrepancies can be lead back to the fundemental difference between the two dimensional nature of the model and the three dimensional biological cell that is highly emphasized in the dumbbell geometry. However, for the different tip geometries we observe accordance even on the level of microscopic details that highlights the strong predictive capability and clever biological abstraction of the model.

In conclusion, CPM parameter determination benefits from a step-wise calibration approach with experimental data leading to the capability of reproduction of many features of cell migration simultaneously. Yet, fundamental differences restrict full accuracy. An expansion of the CPM to three dimensions at conserved volume and explicit introdution of a bio-chemical and a mechanical adhesion field could lead to a much more accurate representation and could even allow for modelling of different cell lines opening a whole new field of possible experiment-simulation comparisons.

5. Persistence of Polarized Motion in Mazes

The ability of single cells to move persistently over large distances through complex environments is an important process for instance for the human immune system. There, leukocytes are exposed to different external clues [184] and in response navigate through dense surroundings in a fast and efficient manner securing our resisting to pathogens [5]. While migrating through complex tissue, cells constantly have to find their path exploring different branches and squeezing through small constrictions. To investigate this complex form of navigation, an abstraction to more simple geometries is useful [185]. Whereas directed leukocyte migration is crucial for our immune system, just the opposite is true for cancer metastasis where cells invade into healthy tissue leading to the formation of new tumors. This single cell migration of cancerous cells can be observed both in three dimensions as well as in two dimensional lanes [173, 143].

Much is already known about the biochemical regulation of polarization inside cells but we want to analyze the temporal evolution of cell polarization in a complex environment. Here, we investigate single cell decisions in mazes and the resulting development of a directional memory. We apply a simple urn model, expand it for a memory term and a memory-degradation term and find that cell migration through a maze is more than a simple random left-right decision. Previous decisions influence the next choice and the effect weakens for decisions laying further back.

This work is a collaboration with Theresa-Maja E. Reitz as part of her Bachelor's Thesis [186] and David B. Brückner and Chase P. Broedersz from the Arnold Sommerfeld Center for Theoretical Physics of the LMU.

5.1. Accessing Migration through Mazes

Confining cells to microstructures is a very versatile and broadly used tool to investigate specific properties of cells in a reproducible and coherent manner. To investigate directional bias in cell migration, a geometry presenting many subsequent left-right decisions is needed. Furthermore, cells need to be able to migrate the maze in any direction to gain long trajectories and better statistics.

The Maze

The structure used to access persistence of polarization here is shown in Fig 5.1. It consists of a stretched hexagonal lattice to suggest a preferred movement direction along the long side of the pattern. Cells moving from left to right or vice-versa encounter a spike forcing them to decide for left or right. They are lead back into a horizontal part and again encounter a spike forcing them to decide. In this way, many subsequent decisions can be observed of many cells in parallel as plotted in Fig 5.1c.

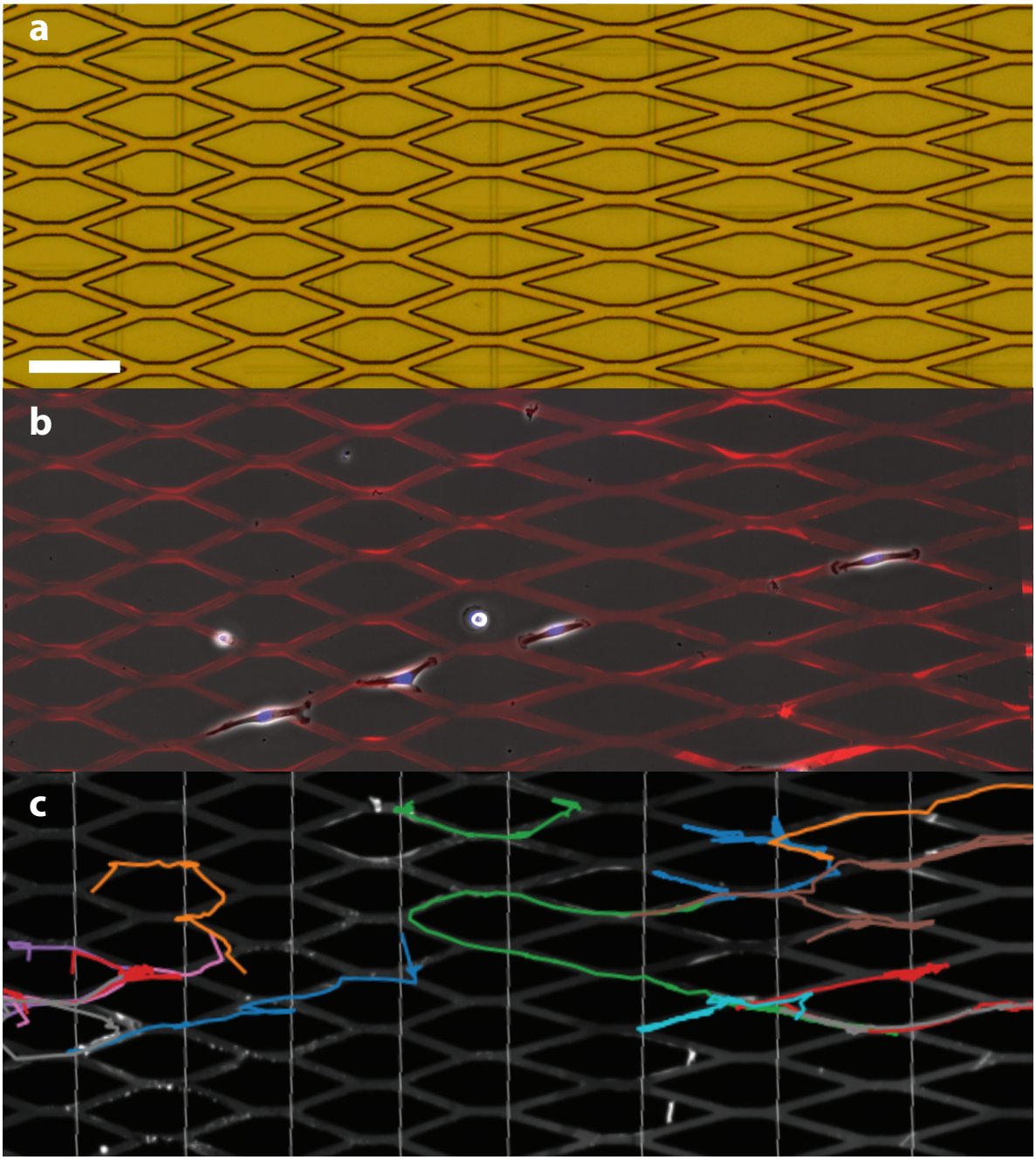

Figure 5.1.: Microstructured maze for the investigation of directional memory in cell migration. Scale bar = 200 μm. **(a)** Image of the wafer negative structure. **(b)** Experimental overlay image of cells on the maze. Micropattern in red, phase contrast in gray and cell nuclei used for tracking in blue. **(c)** Binarized maze and trajectories in color generated using the TrackMate plugin of ImageJ [187].

Here, all experiments were performed with MDA-MB-231 cells, a highly invasive breast cancer cell line shortly described in Appendix A.4. Structures were fabricated using microcontact printing as described in section 2.4 and [150]. Trajectories were extracted using the TrackMate plugin of ImageJ [187].

Breaking down Motion into Decisions

To discretize the cell trajectories into a tuple of choices, the maze is subdivided into unit cells and cell motion is tracked from one unit cell to another as illustrated in Fig 5.2. This results in lists of discrete left or right choices for each cell obtained as described in section B.3.

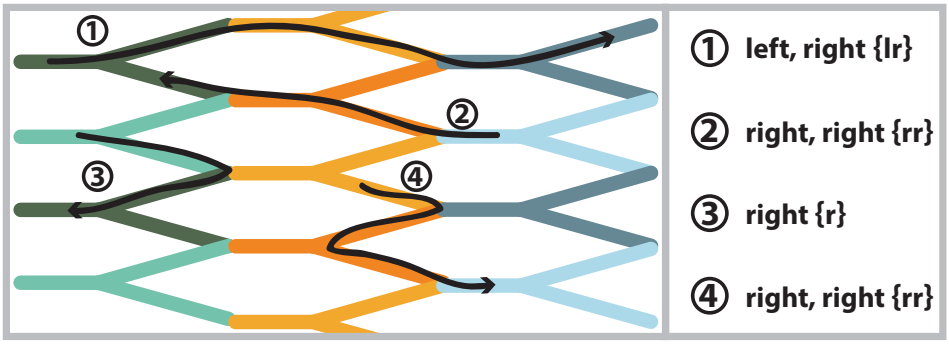

Figure 5.2.: Exemplary trajectories of cells on a grid of unit cells and resulting decision lists. Unit cells are color coded. Trajectories 1 and 2 show no turning events. Trajectories 3 and 4 show one and two turning events, respectively. Two successive turning events as shown in 4 lead to a difficulty in classification as {right, left} is justifiable as well depending on how far the cell advances into the horizontal part of the orange unit cell. If trajectory 4 advances more than 26 μm into the dark blue unit cell, the track is classified as {right, left, right}. This distance corresponds to roughly a quarter of the horizontal segment of the unit cell.

The decisions are saved in lists and result in the relative frequency tree shown in Fig 5.3. All tracks are stopped after four subsequent choices to minimize the selection for unusually fast cells. The total amount of cells to make the fourth choice has dropped to about one third. In the relative frequency tree, all possible choices are listed separately and can be used to get a first feeling for the stability of the observed effects. As we know nothing about the previous choices of the cells and the pattern is symmetric for left and right choices, we expect the first decision to have a 50:50 relative frequency as directional biases of different cells should level out. Deviations from these numbers can be seen as a quality measure for sample size and the resulting stability of stochastic effects and relative frequencies. Here, for a total of 2787 cells we observe relative frequencies of $f(l) = 51.6\%$ for a first left choice and $f(r) = 48.4\%$ for right. For the probability of a first left choice, we obtain a 95% Wald confidence interval of $[0.497, 0.535]$ which indicates that deviations from symmetry, if present at all, are very small. Thus, and as there is no reason why cells should have an intrinsic preference for left or right, the order of choices is assumed to modulate the relative frequencies in a symmetric way, i.e. $f(\{llrr\}) = f(\{rrll\})$. A symmetrization of the decision tree for left and right further improves the statistic reliability by roughly doubling the number of observations and the relative frequencies are treated as probabilities for comparison with models for memory in the following denoted as ”s“ for start and same as the first choice and ”d“ for different than the starting choice.

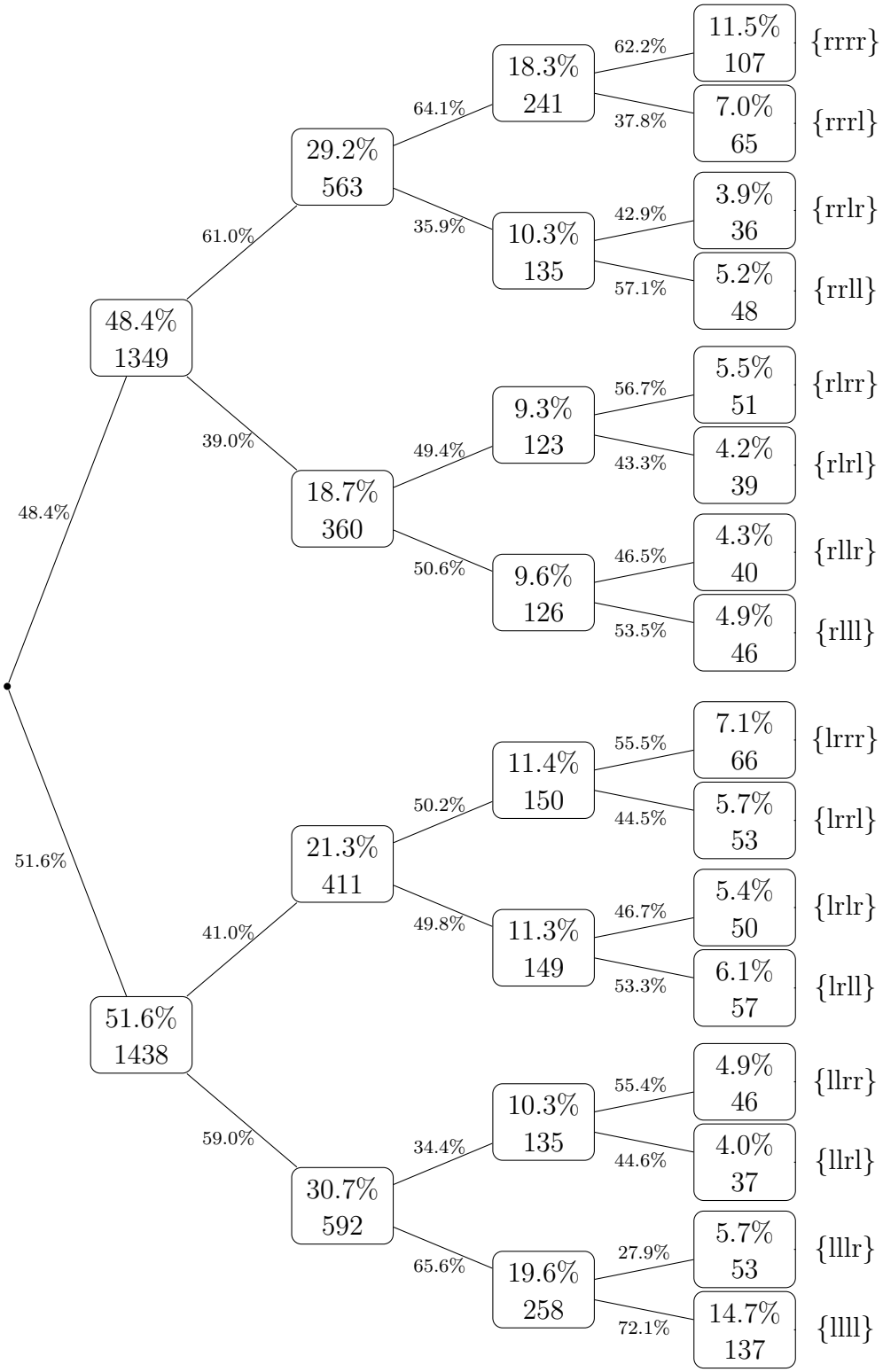

Figure 5.3.: Decision tree for single cells in a maze. Edges are labeled with dependent relative frequencies, boxes indicate absolute relative frequency and total number of observations. Last column specifies branch decisions, "l" for left and "r" for right.

For the ease of comparison, a symmetrized decision tree with according labeling is depicted in Fig 5.4.

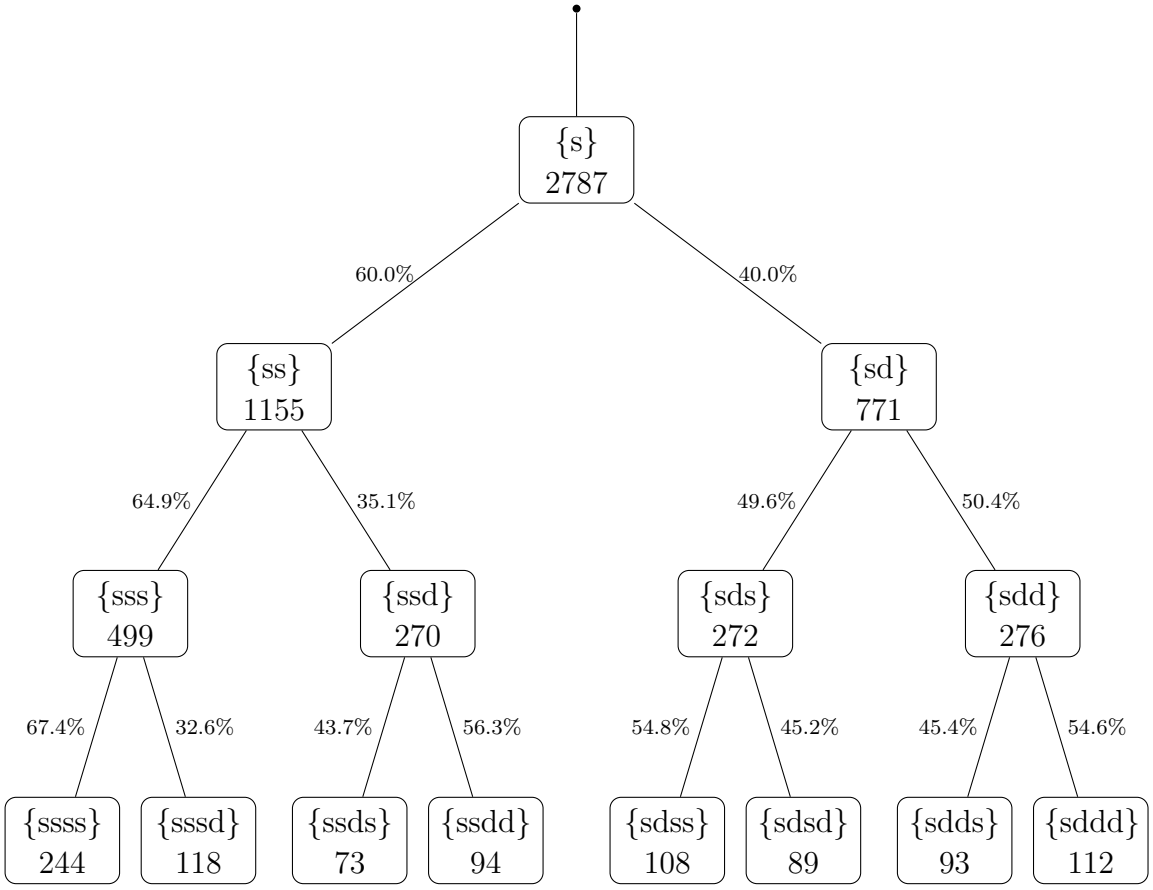

Figure 5.4.: Symmetrized decision tree for single cells in a maze, "s" denotes start and same as first choice, "d" indicates a switch in decision compared to the first one. Edges are labeled with dependent relative probabilities, boxes contain choice abbreviation and total number of observations. {dddd} is incorporated in the total number of {ssss} for reasons of symmetry.

If the decision sequence is to be considered, the dependent relative probabilities denoted at the edges can be compared. Here, accumulating preference for series of "s" decisions can be seen.

5.2. Modelling Migration through Mazes

As a first access point for comparison with models, the decisions can be visualized and compared to a Galton Board, a visualization of a Bernoulli process suggested by François Galton in 1889 [188]. Fig 5.5 shows the comparison of four successive left-right choices in comparison to a classic Galton Board. The distributions plotted in Fig 5.5b show pronounced deviations of the cellular behavior from an ideal Bernoulli process. Indeed, a χ^2 test comparing experiment and Galton probabilities is highly significant with a p-value of about zero. This indicates that subsequent cell decisions are not independent.

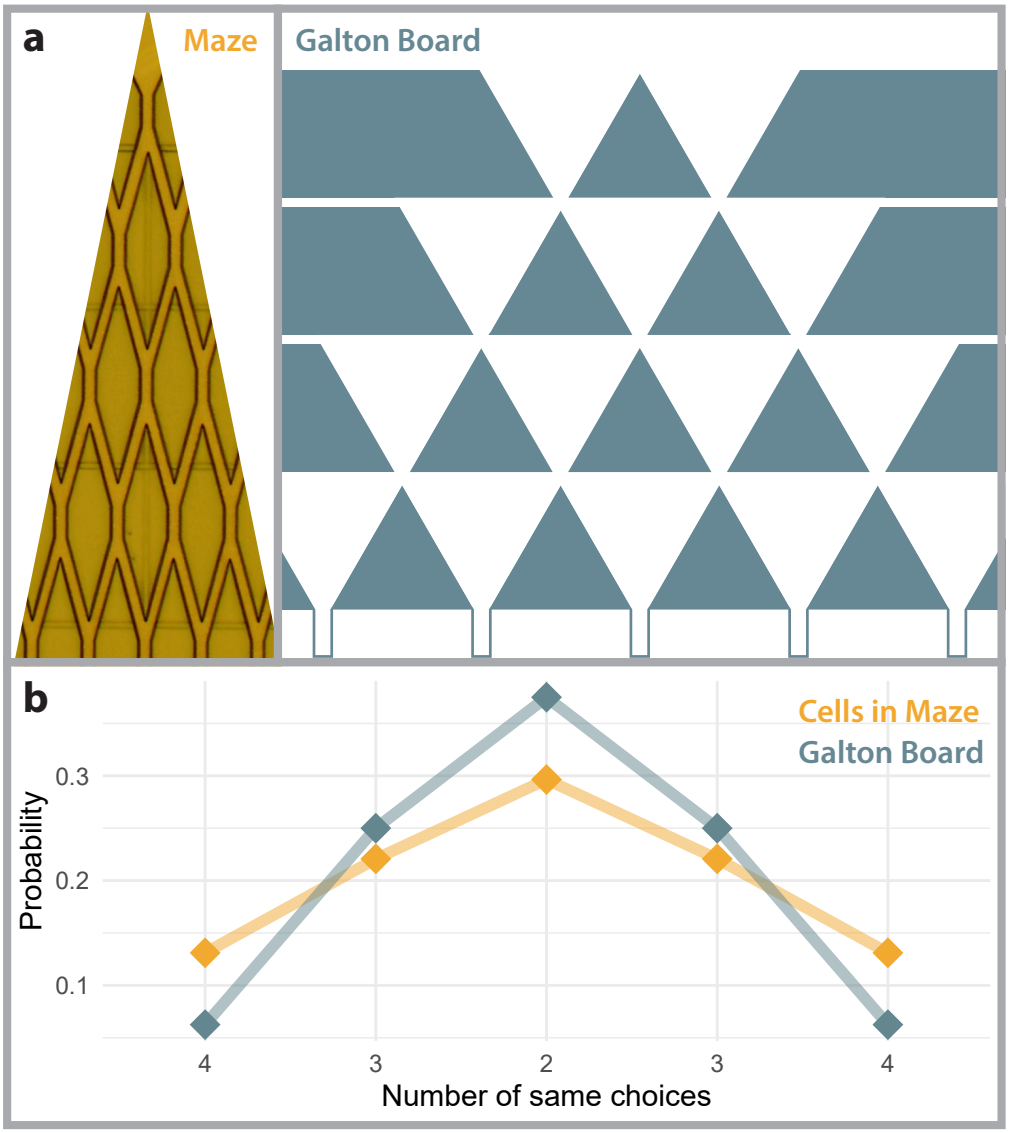

Figure 5.5.: Comparison of four subsequent left-right decisions of cells in a maze with a Galton Board with four levels. **(a)** Image of the maze and board structure. **(b)** Plot of symmetrized choice frequency for N=931 cells (orange) and probabilities of the Galton Board (blue).

The Urn Model

To quantify the deviation of the cellular probability distribution from a Bernoulli process, the urn model provides a simple and suitable platform. Here, we model left or right choices of cells as drawing from an urn containing spheres in two colours, "s" and "d". To account for dependence, after each decision the cells adds additional H spheres of the same colour to the urn. A value of $H = 0$ corresponds to the classical drawing with replacement and $H = -1$ equals drawing without replacement. We also allow for non-integer values of H and start with five spheres of both colours. In fact, in this model the probability of a path $X_1, \ldots, X_n \in \{s, d\}$ does not depend on the order of decisions and can be written in dependence of $k = \sum_{i=1}^{n} \delta_{X_i,s}$, the number of "s" choices amongst n subsequent decisions:

$$p(k) = \binom{n}{k} \frac{\prod_{i=0}^{k-1}(5 + iH) \cdot \prod_{j=0}^{n-k-1}(5 + jH)}{\prod_{m=0}^{n-1}(10 + mH)} \,.$$

For the same four successive choices as visualized above, i.e. $n = 4$, $k \in \{4, 3, 2\}$, the probability distributions are modulated by H as shown in Fig 5.6.

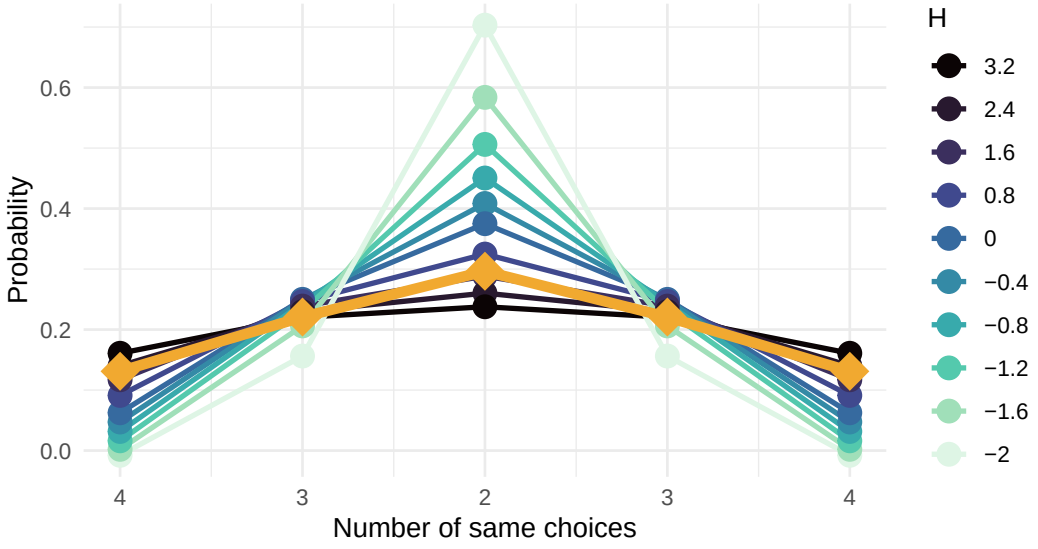

Figure 5.6.: Comparison of four subsequent left-right decisions of cells in a maze with an urn model. Experimental data in orange, $N = 931$ cells. Urn model data color coded for parameter H. Initially, the urn contains 10 spheres, 5 each, and H describes the change in sphere number. For $H = 0$, the probability distribution of the Galton Board is recovered.

Comparing the distributions created by the urn model to the experimentally observed probabilities, the optimal value seems to be close to $H = 1.6$ which indicates a positive feedback, i.e. a tendency of the cell to repeatedly choose alike. This model only takes into account the absolute number of choices and in particular has perfect memory. For a more fine-grain analysis, we compare single paths in the decision tree (Fig 5.4) with the respective model probabilities in Fig 5.7.

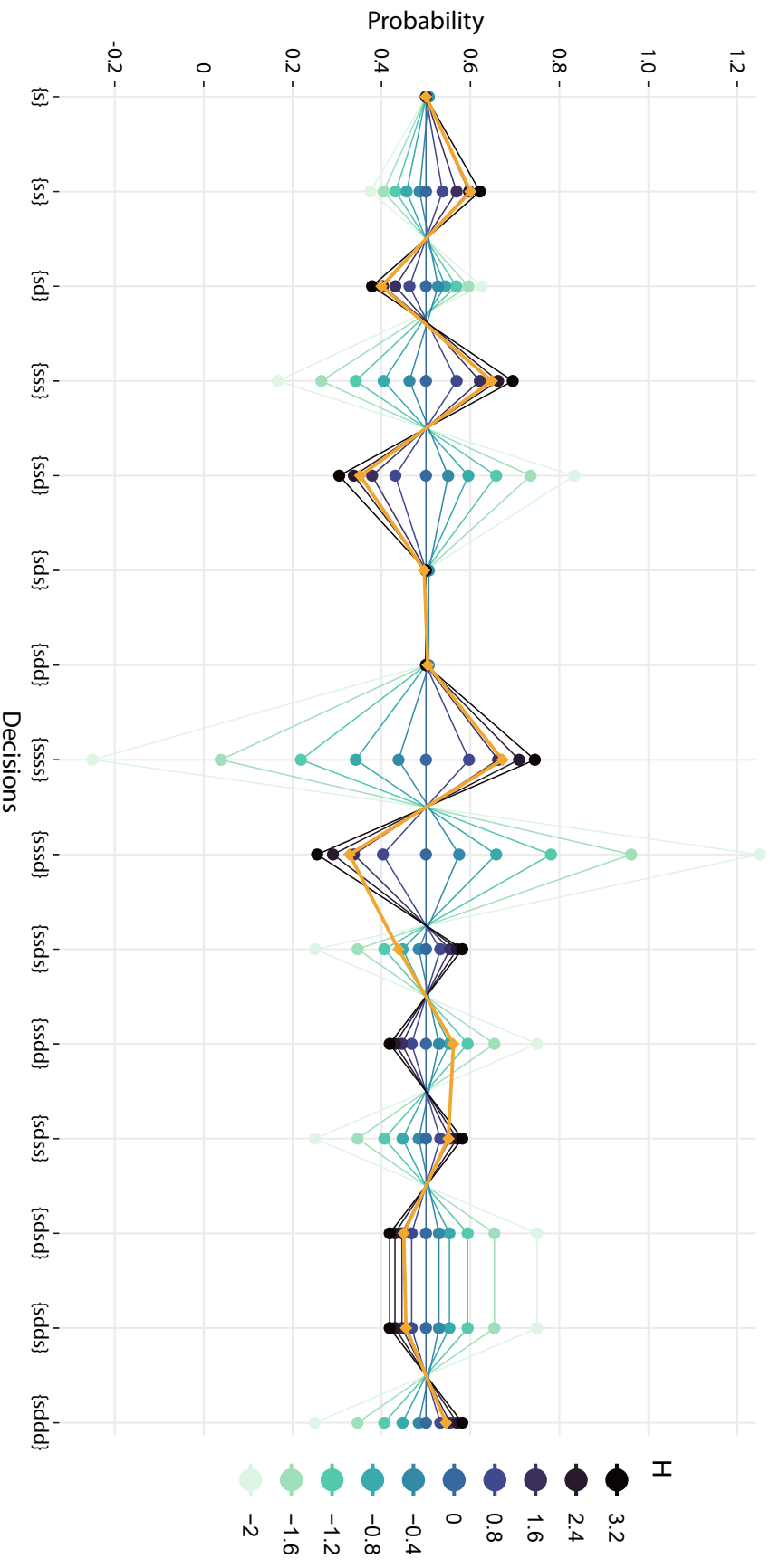

Figure 5.7.: Comparison of symmetrized decision tree probabilities shown in Fig 5.4 with an urn model. Experimental data in orange. Urn model data color coded for parameter H.

At comparison of the detailed decisions, two big differences become immediately apparent. For {ssds} and {ssdd}, the urn model shows strong deviation from experiment and no longer $H = 1.6$ seems to be the perfect fit but rather about $H = -0.9$. Despite this, for an increasing number of decisions made, decreasing values of H can be seen to fit best. This indicates that early choices are over-represented and in experiment choices laying further back in time loose influence. By the nature of the urn model, an implementation of a memory degradation term would worsen interpretability. The impact of the parameter H is not accessible in an intuitive fashion as at later choices the number of spheres has changed and adding a constant number of spheres results in a decreasing influence on probabilities.

A Two Parameter Model for Memory

A model with more intuitive change in probabilities, e.g. proportional influence of H on the probabilities in each step, can have following form with again X_n the results of previous n decisions, $X_{i\in n} \in \{s, d\}$, and k_n the number of "s" choices thereof:

$$p(X_{n+1} = s|X_1, ..., X_n) = \max(\min(\ 0.5 + k_n H - (n - k_n)H,\ 1),\ 0)\ .$$

This allows a direct proportional change in probabilities and describes the imbalance between left and right choices. So far, this model does not include a fading in memory over time but it can be expanded by an additional parameter $\lambda > 0$ to describe the loss of memory:

$$p(X_{n+1} = s|X_1, ..., X_n) = 0.5 + \sum_{i=1}^{n} e^{\lambda(i-n)} H\ (\delta_{X_i,s} - \delta_{X_i,d})\ . \tag{5.1}$$

This model now includes a symmetric change in probability by a factor H at decision and a loss of influence of previous choices at a rate e^{λ}. Assuming $|H| < 0.5 \cdot (1 - e^{-\lambda})$, we obtain $0 < p(X_{n+1} = s|X_1, ..., X_n) < 1$ leaving a positive probability for both outcomes for all $n \in \mathbb{N}$ unlike the previously discussed one parameter models.

In comparison with experimental data, a minimum residual sum of squares optimization has been used to estimate parameters fitting observed relative frequencies in each stage of Fig 5.8. For estimation of experimental error, a bootstrapping algorithm has been applied and the resulting fits are shown in Fig 5.8. The reduced one parameter model shows some quite pronounced deviations for {ssds} and {ssdd} as already observed for the urn model but else is able to qualitatively describe the probabilities. The two parameter model is capable to show the right tendency (more or less than probability 0.5) for all observed decisions. When comparing the change in probability H, the two models show strong differences. The one parameter model has relatively weak feedback onto the probabilities whereas H is about a factor of five stronger in the two parameter model but looses a factor of about one half in influence with each previous decision.

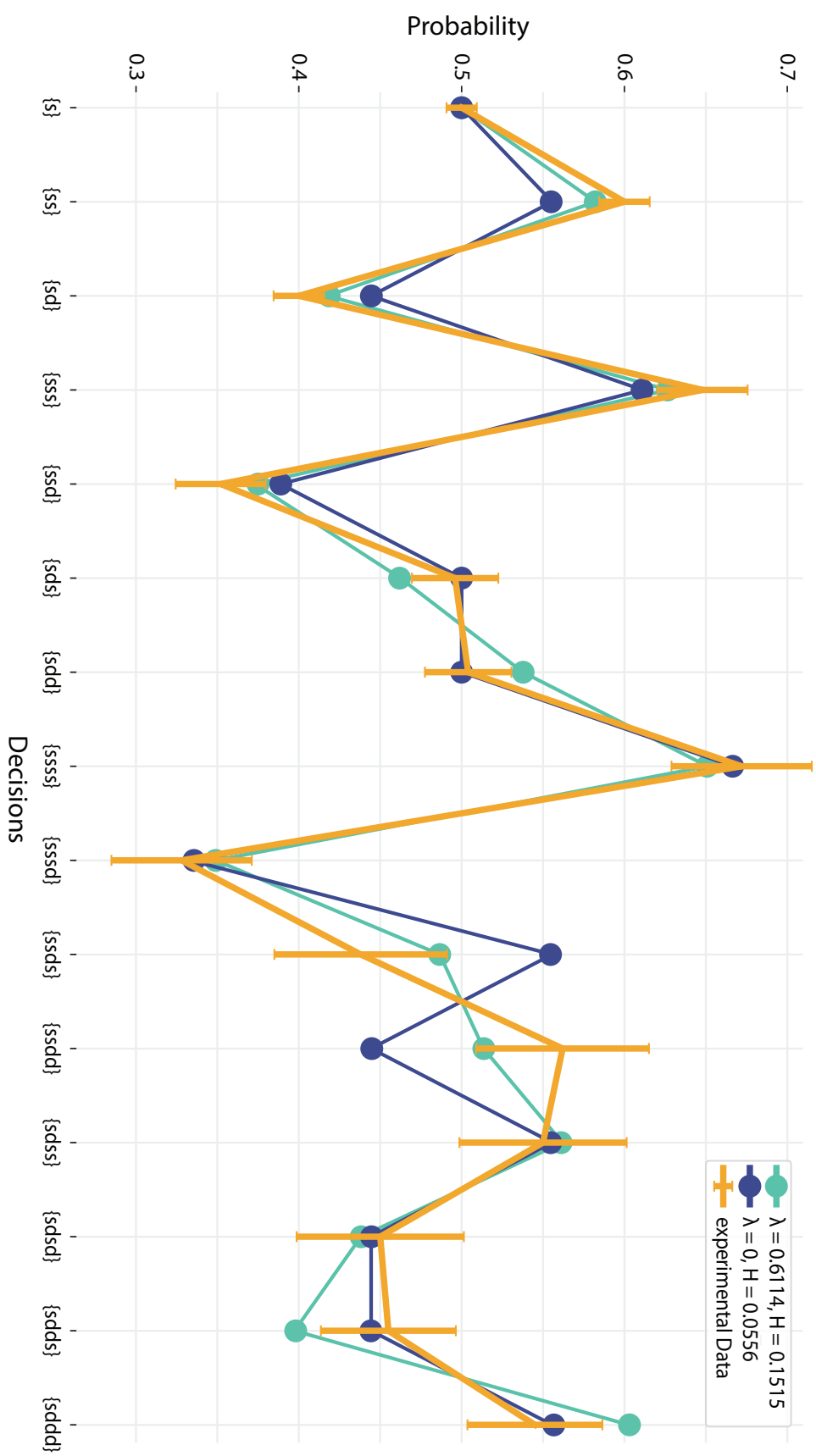

Figure 5.8.: Comparison of symmetrized decision tree probabilities shown in Fig 5.4 with model 5.1. Experimental data in orange. Errorbars indicate standard deviation.

5.3. Discussion

In conclusion, cellular motion through mazes cannot be described as pure random left-right decisions. While the overall distribution of cells can be recapitulated by an urn model with simple feedback, the detailed probabilities including the order of choices presents cannot be quantitatively captured. To describe the observed decisions, a two parameter model is needed, that includes relative changes in probabilities and a term for memory loss over time.

However, biochemical understanding of ”memory“ has yet to be obtained. To this end, memory can be seen as simple inertia in motion which leads to preferences of same choices. The cumulative effect observed here could be linked to a stronger polarization towards this direction. First experiments to force a reset of the lamellipodium by introducing a constriction before the branching segment did not bring the desired result as cells preferred to redirect motion rather than force the way through the constriction.

For more detailed insights into the cellular process of deciding, the decision should be analyzed as a temporally resolved process. Therefore, heatmaps indicating the spatial distribution of cells in the unit cells could lead to a deeper understanding if simple inertia is the key factor in deciding or if cells spend much time at the branching point and more actively choose a direction. To this extent, a brightfield segmentation of cell shapes could further improve the picture of cellular decision making.

On the long run, targeting potential polarization related proteins by fluorescent dyes, e.g. by a FRET sensor for active Rac1 Rho GTPase, could answer the question if the cell stays polarized into the same direction during the decision process. Also, choosing differently branched geometries, e.g. regular hexagonal paths, could lead to a simplification of the categorization of decisions that currently present a possible source for errors, as shown in Fig 5.2, trajectory 4. Furthermore, a comparison of invasive behavior of metastasizing cancer cells and leukocytes on structures allowing multiple protrusions and constrictions as described by Kopf *et al.* [185] could lead to further understanding of the invasive capabilities of cells during tumor spreading and their origin.

6. Cell-Cell Contacts and Friction

After previously studying single cells and their motility in confinement, we now turn to cell-cell interaction. Generally speaking, collective cell migration plays an important role in many processes such as development, wound healing and metastasis. This highly complex process, as shortly described in section 2.2.3, includes three hallmarks as specified by Friedl and Gilmour [96]: First, the formation of cell-cell junctions that connect cells on a physical and biochemical level and remain intact during movement. Second, an actin cytoskeletal organization that spans across cell boundaries. Third, changes in the extra cellular matrix around the cells. Different collective migration modes are tuned by the strength of junctions and the molecules involved [93]. Cell-cell interaction and communication thus is a crucial process for collective movement.

One important type of such cell-cell junctions are based on E-Cadherin [101]. Its role in metastasis, however, is still unclear and subject to recent studies [189, 13]. A simple access to the complex process of E-Cadherin based collective migration is a reduction to two cells. To ensure reproducible two-cell encounters, cells can be confined to a 1D lane microstructure [190, 191] where they can either redirect, slide past each other, or follow one another. A more advanced "cell collider" has recently been proposed and explored by Brückner *et al.* [34]. Here, cells are confined to a dumbbell shape consisting of two adhesion sites connected by a narrow bridge [26, 163, 192]. Due to the shape of confinement, multiple repeated collisions of two cells can be observed in parallel. In a previous study, Brückner *et al.* show that this geometry is well suited to characterize cell-cell interaction. They compare a highly invasive cell line, MDA-MB-231, and a non-cancerous cell line, MCF10A, and quantify differences in encounter behaviour. Both cell lines are briefly characterized in Appendix A.

Here, we employ this previously suggested "cell collider" to quantify the influence of cell-cell signalling proteins on two-cell interactions of the same cell lines, MDA-MB-231 and MCF10A. We show that blocking of E-Cadherin, a mainly mechanical coupling protein, leads to a more invasive phenotype in MCF10A and their motility pattern evolves similar to that of MDA-MB-231. We also explore the role of the signalling protein ephrin-A2 onto the invasiveness of MDA-MB-231 and find that blocking of ephrin-A2 lead to a even far more invasive behaviour.

This work is a collaboration with Georg Ladurner as part of his Master's thesis and David B. Brückner and Chase P. Broedersz from the Arnold Sommerfeld Center for Theoretical Physics of the LMU.

6.1. Motion of Two Cells in a Confining Geometry

To investigate repeated encounters of two cells, Brückner *et al.* have developed an analysis that will be briefly wrapped up in this section following the line of thought of their recent publication [34].

They propose a dumbbell shaped micro-confinement, as shown in Figure 6.1a. Here, cells adhere to one square each and they extend lamellipodia along the bridge connecting the squares transitioning onto the other side. The cell position is accessed via tracking of the stained nucleus. Three different outcomes of such cell-cell contacts are distinguished as shown in Fig 6.1b. Either the cell invading the other square turns back and reverses into its original square, or the other cell slides past the intruder, leaves the square and they switch places, or the cells connect and both follow each other to the vacant square. Panel c displays an exemplary interaction table with relative occurences of the different interaction types. Tables of this kind will be used to compare and quantify cell interactions in the following.

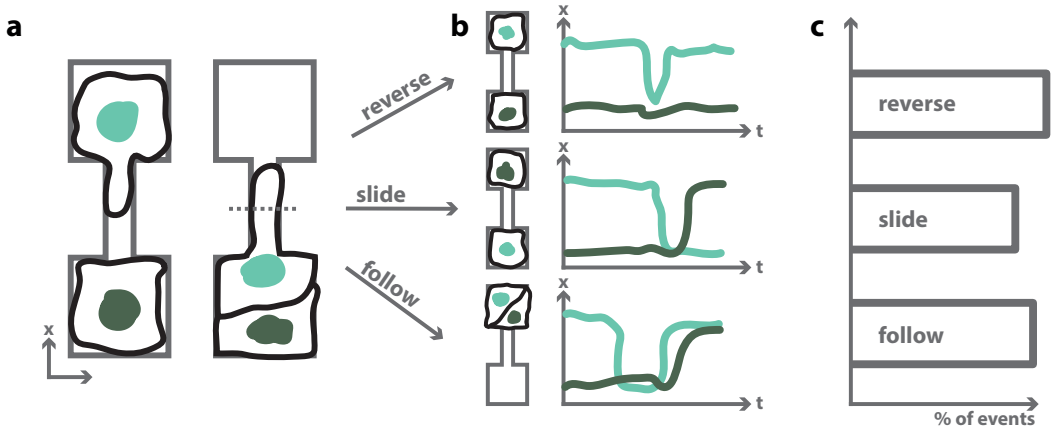

Figure 6.1.: Two cell behaviour on a dumbbell micropattern. **(a)** Cells occupy one square each. A contact events starts when one cell nucleus crosses the centre of the pattern, as indicated by the dashed grey line. **(b)** Possible outcomes of contact events and resulting nuclear trajectories **(c)** Interaction table showing exemplary relative frequencies of contact results.

Moving from a phenomenological level to a more advanced analysis, as described in 2.3.2, both previously mentioned cell lines can be compared in terms of their distance dependent cohesion f and their friction γ that is dependent on relative position and relative velocity. Figure 6.2 shows the cohesion and friction terms for both cell lines as well as the respective interaction tables. The first row shows interaction analysis of the highly invasive MDA-MB-231 cell line, second row shows the same analysis for MCF10A. This analysis reveals quite different interaction behaviour of both cell types. On a phenomenological scale, MDA-MB-231 cells slide past each other, whereas MCF10A cells tend to reverse at contact and slide less frequently. At the dynamic level of those interaction events, even more pronounced differences become apparent. On short ranges, MDA-MB-231 cells do not repel each other but are attracted and even accelerate at contact, as the positive friction term indicates. MCF10A cells exhibit an overall repulsive interaction and slow down as moving past each other.
For more details on the underlying model and further analysis, please refer to Brückner *et al.* [34].

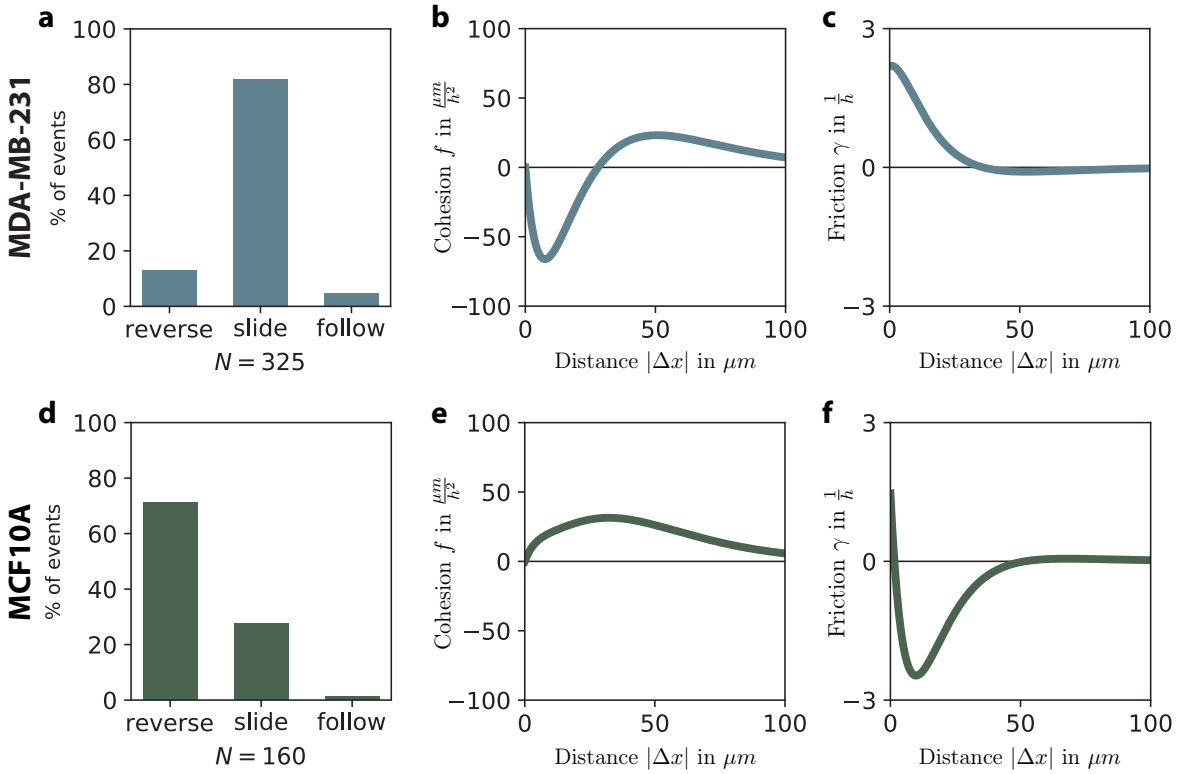

Figure 6.2.: Analysis of two cell interaction on a dumbbell micropattern for two different cell lines. First row MDA-MB-231. **(a)** Sliding past each other is the dominant interaction. **(b)** Cells show short ranged negative cohesion, i.e. attraction. **(c)** Cells show short ranged positive friction, i.e. anti-friction.
Second row MCF10A. **(d)** Reversal up on contact is the dominant interaction. **(e)** Cells show mutual repulsion. **(f)** Cells exhibit short ranged friction.
Plots shown courtesy of David Brückner.

6.2. Influence of E-Cadherin on Cell-Cell Interaction

E-Cadherin mechanically couples cells and plays an important role in the establishment and maintenance of cell-cell contacts and signalling, see also section 2.2.3. Many recent studies indicate an important role of E-Cadherin in cancer metastasis as E-Cadherin levels often are low in single invading cells and high when trains of cells metastasise tissue [13, 102]. In clinical studies low expression levels of E-Cadherin are often linked to poor prognosis [193]. The previously analysed MDA-MB-231 cells do not express E-Cadherin [194, 195] but MCF10A cells do [196]. In a comparable study of cells on lanes of different widths, Milano *et al.* [191] have found E-Cadherin expression levels to influence the number of sliding events. Introducing E-Cadherin expression in MDA-MB-231, they observed a decrease in the number of cells sliding past each other and for MCF10A cells with E-Cadherin knock-out the number of sliding events increased.

This leads to the question how detailed interaction dynamics are influenced by E-Cadherin. The cell collider provides a suitable platform to characterise cell-cell interac-

tion in terms of friction and attraction. We block E-Cadherin in MCF10A cells using an antibody[1] in an excessive concentration of 5 $\frac{\mu g}{ml}$, referred to as MCF10A E-Cad. In Fig 6.3, the resulting dynamics of MCF10A E-Cad are shown and compared to MDA-MB-231 and MCF10A. On a phenomenological level, blocking E-Cadherins leads to an increase in sliding events and a reduction of reversal. The overall behaviour is located in between the two original cell lines. When taking a closer look at the exact dynamics, cells still repel each other at all distances, only at intermediate ranges, the repulsion is zero. However, no attraction on short distances as for the MDA-MB-231 cells can be seen. In terms of friction, cells behave more like the MDA-MB-231 cells as they no longer display strong friction on very short distances but even slight acceleration can be seen. This acceleration is particularly interesting as interaction by E-Cadherin is mainly mechanical and thus blocking of E-Cadherin should only lead to a reduction of friction as mechanical coupling is disabled. A change to acceleration on the other side indicates not only a loss in mechanical friction but a modification of signalling as well. This could be induced either by the blocked E-Cadherin itself or a change in the actin cytoskeleton where the formation of "stress fibers", i.e. actin bundles, is stabilized by E-Cadherin-E-Cadherin bounds.

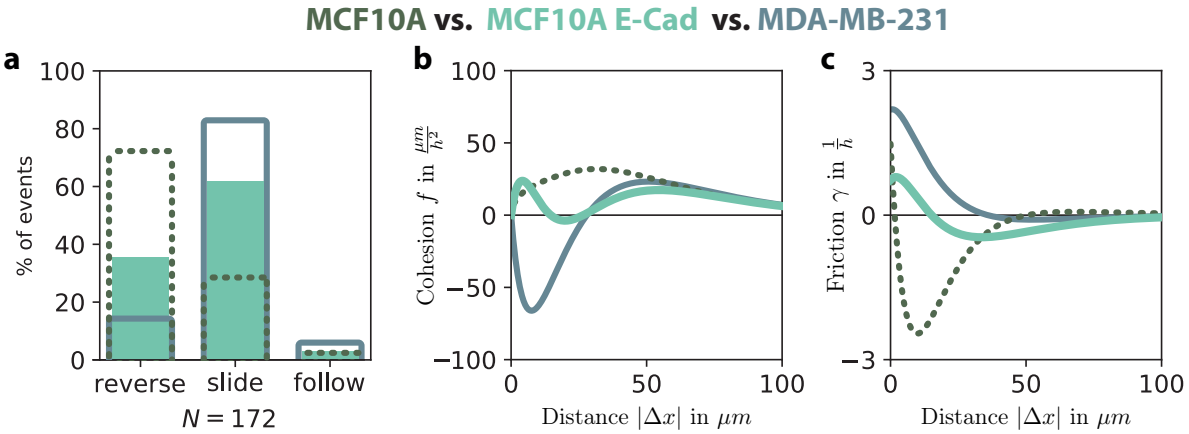

Figure 6.3.: Comparison of MCF10A blocked E-Cadherin (MCF10A E-Cad) to wild-type cells. Wild-type data extracted from Fig 6.2. Green colours indicate MCF10A cell line, dark and dotted for wild-type, bright for antibody blocked E-Cadherin. Blue depicts MDA-MB-231 cell line. **(a)** Relative frequency of contact event outcomes. Sliding emerges as dominant interaction at blocking of E-Cadherin in MCF10A as is typically observed for MDA-MB-231 cells. Indicated number of observations for antibody experiment denoted below. **(b)** E-Cad cells show overall repulsion as wild-type with spatial modulation at intermediate distances. They show no attraction as MDA-MB-231 cells. **(c)** Friction is greatly reduced in E-Cad cells and even slight anti-friction as for MDA-MB-231 cells is observed on short distances.

[1] anti-CD324 (E-Cadherin) Monoclonal Antibody (DECMA-1), Functional Grade, eBioscience™ from Thermo Fisher Scientific, catalog # 16-3249-82, RRID AB_10734213

Concludingly, we observe that blocking E-Cadherin with an antibody in MCF10A does not only reduce friction but in terms of friction leads to interaction behaviour between two cells that is more similar to MDA-MB-231 although less pronounced. However, in terms of cohesion cell-cell interaction still is repulsive as in the wild-type. In general, MDA-MB-231 and MCF10A cells have fundamentally different expression levels of various proteins that all could influence their interaction dynamics [197]. For instance do MDA-MB-231 cells lack E-Cadherin but instead express Cadherin 11, another cell-cell coupling protein [198].

6.3. Influence of Ephrin-A2 on Cell-Cell Interaction

As reduction in mechanical coupling leads to more invasive behaviour in MCF10A cells in terms of sliding events and friction indicating a change in signalling as well, modification of cell-cell signalling could reverse the effect and lead to less invasive behaviour in MDA-MB-231 cells.

A prominent family of cell-cell signalling proteins are erythropoietin-producing hepatocellular receptors (Eph receptors) and their ligands, Eph receptor interacting proteins (Ephrins). They are common in many different cell types throughout the body and play important roles in many signalling processes [199, 200]. Due to their receptor-ligand type of binding, different signalling cascades can be activated inside the two connected cells by receptor and ligand, i.e. forward and reverse signalling [201, 202]. Furthermore, receptor-ligand interactions are not restricted to a matching pair but different receptors can bind to one ligand and the other way round leaving many potential interaction possibilities [203]. Ephrin-A1 and the two receptors EphA2 and EphA1 have already been characterized to play an important role in breast cancer survival [204], regulate metabolism and growth in MCF10A [205] and display different levels of expression in MDA-MB-231 and MCF10A [206] leading to different migration responses at ephrin-A1 clustering [207]. Much less is known about ephrin-A2, another member of the ephrin ligand family, that only recently has started to gain attention in the field of cancer research. Ephrin-A2 has been found to promote metastasis in prostate cancer by enhancing cell invasion depths *in vitro* and promoting angiogenesis and tumor size [208]. In the breast cancer cell line MDA-MB-436 ephrin-A2 has been successfully used as target for drug delivery to reduce cancer progression [209]. Here, an ephrin-A2 antibody[2] in a concentration of 1 $\frac{\mu g}{ml}$ is used in MDA-MB-231 cells, referred to as MDA-MB-231 Ephrin-A2. We expect the antibody to block or hinder ephrin-A2 binding to possible receptors leading to a silencing of the receptor-mediated signalling path. However, we do not know if the antibody silences all ephrin-A2 induced signalling. The resulting change in cell-cell interaction behaviour, depicted in Fig 6.4, thus should be taken with a grain of salt and may need further verification by other experimental methods.

[2]anti-Ephrin A2 Monoclonal Antibody (OTI3E3) from Thermo Fisher Scientific, catalog # MA5-25187, RRID AB_2723128

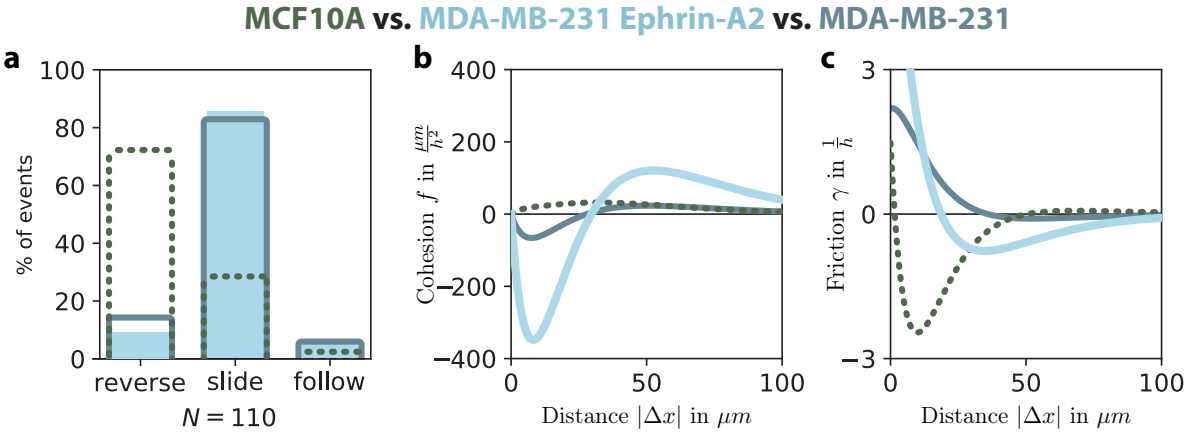

Figure 6.4.: Comparison of MDA-MB-231 blocked ephrin-A2 to wild-type cells. Wild-type data extracted from Fig 6.2. Blue colours indicate MDA-MB-231 cell line, dark for wild-type, bright for antibody blocked ephrin-A2. Dotted green depicts MCF10A cell line. **(a)** Relative frequency of contact event outcomes. Sliding is dominant interaction of MDA-MB-231 Ephrin-A2 cells just as for the wild-type. Indicated number of observations for antibody experiment denoted below. **(b)** Ephrin-A2 cells show even much more pronounced attraction than MDA-MB-231 cells. Axis has been rescaled to show full extent of cohesion coefficient derived from antibody experiment. **(c)** Compared to the wild-type, for the ephrin-A2 blocked cells positive friction, i.e. anti-friction, is enhanced on short distances and converts to negative, regular friction on intermediate distances.

The addition of ephrin-A2 antibody to MDA-MB-231 cells seems to induce an increased invasive behaviour in all surveyed metrics. The strength of effect varies but especially the cohesion term shows a very clearly increased attraction of the cells to each other. Interestingly, this effect does not lead to a higher occurrence of cells following each other. Thus, the effect has to be counter-balanced by the friction term that shows higher anti-friction of cells on short distances compared to the wild-type. This means cells speed up even more when they are close to each other and results in a propelling of cells away from each other. However, as previously indicated, the exact function of the antibody still has to be elucidated and comparably low statistics may distort the effects. In contrast to the observations presented here, Lucero *et al.* report the complete absence of ephrin-A2 in both cell lines used in this section, MDA-MB-231 and MCF10A [210]. This calls for all the more thorough investigation and questioning of the effects described by alternative experimental methods. Nevertheless, the Eph-ephrin family of cell-cell signalling molecules presents a versatile access point to modify cellular interactions. For instance, Eph-receptors have been reported to be involved in contact inhibition of locomotion via the Rho-ROCK signalling pathway and may be another interesting access point for modification [211].

6.4. Discussion

In conclusion, the cell-cell interaction platform proposed by Brückner *et al.* [34] proves a versatile tool to quantify the influence of proteins of interest on cell-cell interaction. For E-Cadherin, we observe a strong anti-correlation of E-Cadherin mediated cell-cell coupling and invasiveness in our system and detect even non-mechanical effects. For Eph-ephrin induced signalling, we also observe strong effects of ephrin-A2 on invasive behaviour indicating an important role in cell-cell communication in our system. However, the complex nature of receptor-ligand binding relations and induced signalling requests more detailed examination. As a first verification a simple immunostaining for ephrin-A2 could answer the question of its presence or absence in the cell lines given the antibody binding is specific enough to this protein only. Genetically knocking-out of ephrin-A2 would allow to determine its role in signalling further. Other, more characterized proteins of the Eph-ephrin family, e.g. EphA2, could also be of interest to infer their influence on cell interaction dynamics. Also, the impact on interaction dynamics of signalling proteins further downstream such as ROCK could be accessed by inhibition, e.g. by Y-27632, to modify the cytoskeletal composition of the interacting cells as reported for MDA-MB-231 by Cascione *et al.* [212].

Generally speaking, the impact of any protein of interest on cell cohesion and friction can be investigated in a quantitative manner using this technique under two restrictions. First, the protein level needs to be controllable, either by a blocking antibody that bears the possibility of cells overcompensating or better by genetical modification. Second, usually cells have more than one signalling pathway to regulate important cellular tasks such as cell-cell interaction or cytoskeletal arrangement. This means that by knockout of one signalling protein one path may be blocked but very rarely do cells not have other pathways to partially compensate this loss. Thus, the full influence of the protein of interest cannot be captured but at least a clear hint of the influence on cohesion and friction can be obtained.

Another application of this platform is the quantification of controlled encounter of cells of different cell lines. By combining one cell each, the interaction dynamics of for instance a metastasising cell line and the surrounding tissue cells can be quantified. This could provide new insights into the details of cell-cell interaction during invasion on a single cell level. By choosing specific proteins, their influence could again be observed at the encounter of two distinct cell types offering a vast field for future experiments.

7. Collective Flow through Constrictions

Cell-cell interaction, taken further from chapter 6, leads to collective migration. Although cell-cell interaction, as described in chapter 6, already presents one of the key processes needed for collective migration, understanding more complex phenomena such as plug-flow, vortex formation or jamming require the analysis of a collective of migrating cells [213]. To abstract processes as complex as collectively migrating cells, theoretical models are a versatile tool to unravel global relations governing the dynamics, see section 2.3 for a short overview.

For collective migration into channels of different widths, Vedula *et al.* report cells exhibiting different migratory phenomena, e.g. contraction-relaxation for narrow stripes and swirling in wide channels [17]. They identify mechanical coupling and cell contractility to be of great influence for the front speeds of the invading cells into the channels. For a channel of constant intermediate width, Marel, Zorn *et al.* observe the development of a stationary plug-like flow profile and a density-dependent emergence of short-lived swirls within the cell sheet [14]. They find the density profile of the cell to stabilize inside the channel and to be well-described by a Fisher-Kolmogorov equation. Tlili *et al.* observe cells moving around a circular object to behave like a fluid as well [18]. In contrast to the fluid description, Angelini *et al.* describe high density monolayers to exhibit glass-like dynamics [214], suggesting a transition from fluid-like to glass-like dynamics with increasing density, a phenomenon often referred to as jamming.

Here, we ask the question to what extent cells obey hydrodynamic laws when we expect proliferation to break mass conservation over long time scales and extrusion from the cell sheet into the third dimension acts as compressibility. Furthermore, we want to explore to what extent these complex dynamics can be captured by a theoretical model. A geometry motivated from hydrodynamics that allows investigation of these questions is a channel with a constriction that afterwards broadens again into the initial width, see Fig. 7.1. This geometry was initially investigated by Matthias Zorn as part of his PhD thesis [117]. This work is a collaboration with Felix Kempf and Erwin Frey from the Arnold Sommerfeld Center for Theoretical Physics of the LMU.

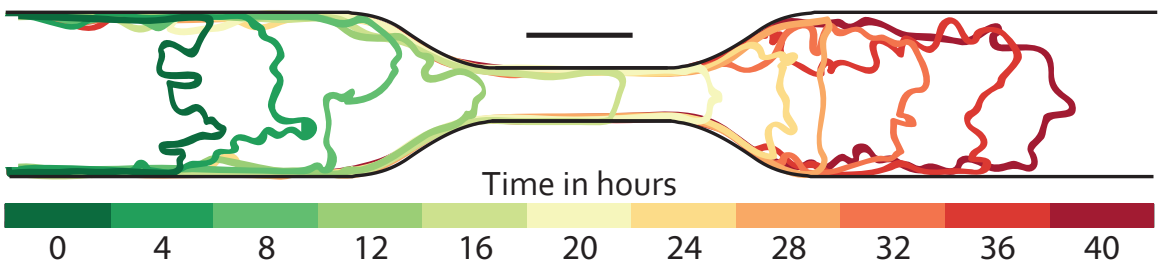

Figure 7.1.: Front shape of cell sheet advancing into a channel with constriction. Scale bar = 200 μm. Cell fronts were manually extracted from an collectively invading cell sheet at the colour coded time points. Image courtesy of Matthias Zorn, adapted with permission from [117].

7.1. Cell Behaviour in Narrowing Channels

As shown in Fig. 7.1, MCF10A cells enter a channel from a reservoir, migrate along, encounter a constriction to pass through and re-emerge into a confinement of the same width as before. Cells are confined by three dimensional PEG-DMA structures, see Appendix A for more details on cells and structuring.

In these experiments, the question was asked how the system deviates from a Newtonian fluid. There, we would expect higher velocity inside the constriction compared to before and after it. To access the velocities, a particle image velocimetry (PIV) analysis is performed, as described in [117]. Generally speaking, PIV analysis tracks displacement of small pixel assemblies from one image to the next, resulting in a flow field often used to visualize fluid dynamics. Here, pixel clusters of the size of 8×8 μm are used to track cell displacement in two subsequent images. The result is exemplarily shown in Fig. 7.2.

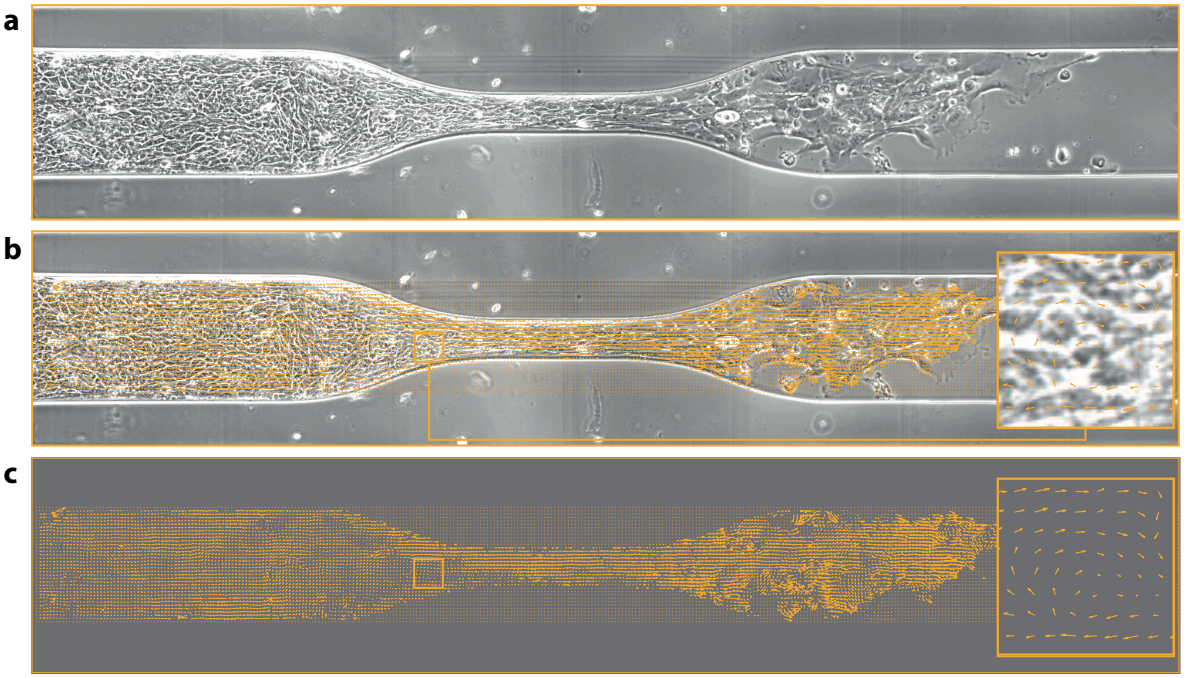

Figure 7.2.: Particle image velocimetry (PIV) analysis of cells migrating through a constriction. **(a)** Phase contrast image of cell sheet advanced into the channel beyond the constriction. **(b)** Overlay of phase contrast image and extracted displacement in two subsequent images averaged over 8×8 μm. **(c)** Velocity field plotted alone for the ease of viewing.
Figure courtesy of Matthias Zorn, adapted with permission from [117].

PIV analysis shows most of the velocity vectors to roughly point into the direction of overall migration but on short length scales more complex behaviour can be observed as can be seen in the insert of Fig. 7.2c. The area of observation is large compared to the spatial resolution but interesting dynamics can be observed at short length scale.

Thus, instead of coarse graining, velocities can be reduced to their component along the direction of migration, parallel to the channel and averaged over the direction perpendicular to the channel and 2 hours in time. The resulting velocity component in x-direction is plotted in Fig. 7.3 for different invasion depths.

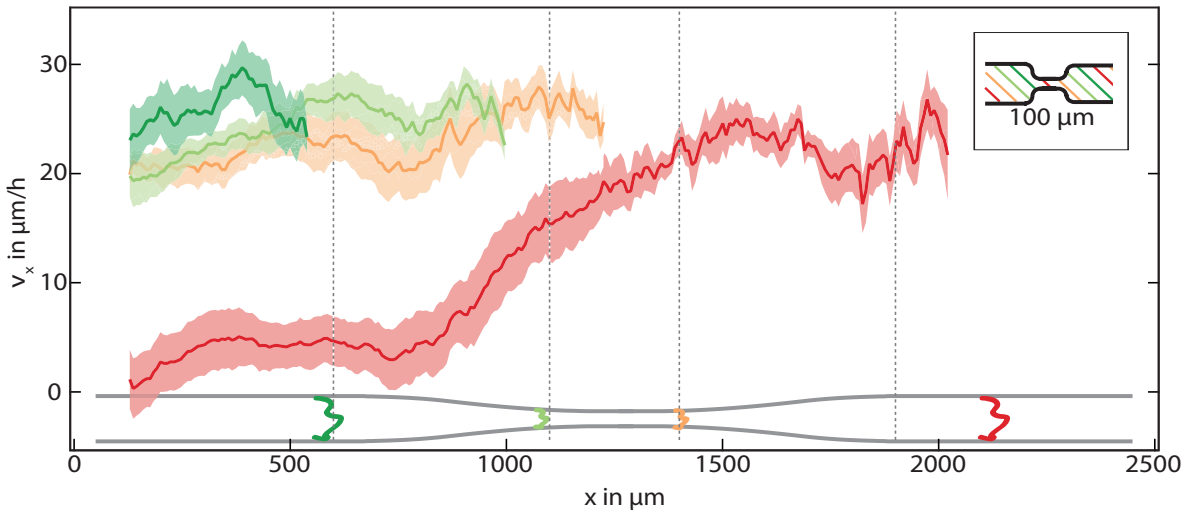

Figure 7.3.: Velocity of advancing cell sheet in parallel to the channel for different invasion depths. Progress into the channel colour coded and indicated on schematic channel drawing at the bottom. Slight difference in indicated cell front and velocity profile due to time averaging of 2 hours. Shaded regions indicate standard errors of the mean.
Image courtesy of Matthias Zorn, adapted with permission from [117].

Interestingly, cells maintain initial speed throughout the narrowing part and the whole constriction. Velocities before the constriction only decrease after the cell front has already migrated 250 μm past the point of the channel that again has maximal width. This observation indicates a clear difference in behaviour to a Newtonian fluid, as velocities are not increased inside the constriction and decreased again after it but we rather see a maximal migration velocity that changes dependent on the position of the cell front as well as the position in the channel itself. The plateau of decreased velocity before the constriction is reproducible over variations in length of constriction as well as for different constriction widths, as depicted in Fig. 7.4. Here, only x-velocities calculated at the last time point are shown for different geometries. Fig. 7.4a shows the emergence of the plateau at introduction of constrictions of different narrowness independent of actual minimal width and in comparison the typical velocity profile for a straight channel. Fig. 7.4b depicts the independence of the length of the constriction. Here, even a dip in velocity right before the constrictions seems to emerge for these geometries. This phenomenon of decreasing velocity in front of the constriction long after the cell front passed may indicate a certain compressibility of cells before motion is altered and presents a key feature for collective flow through constrictions.

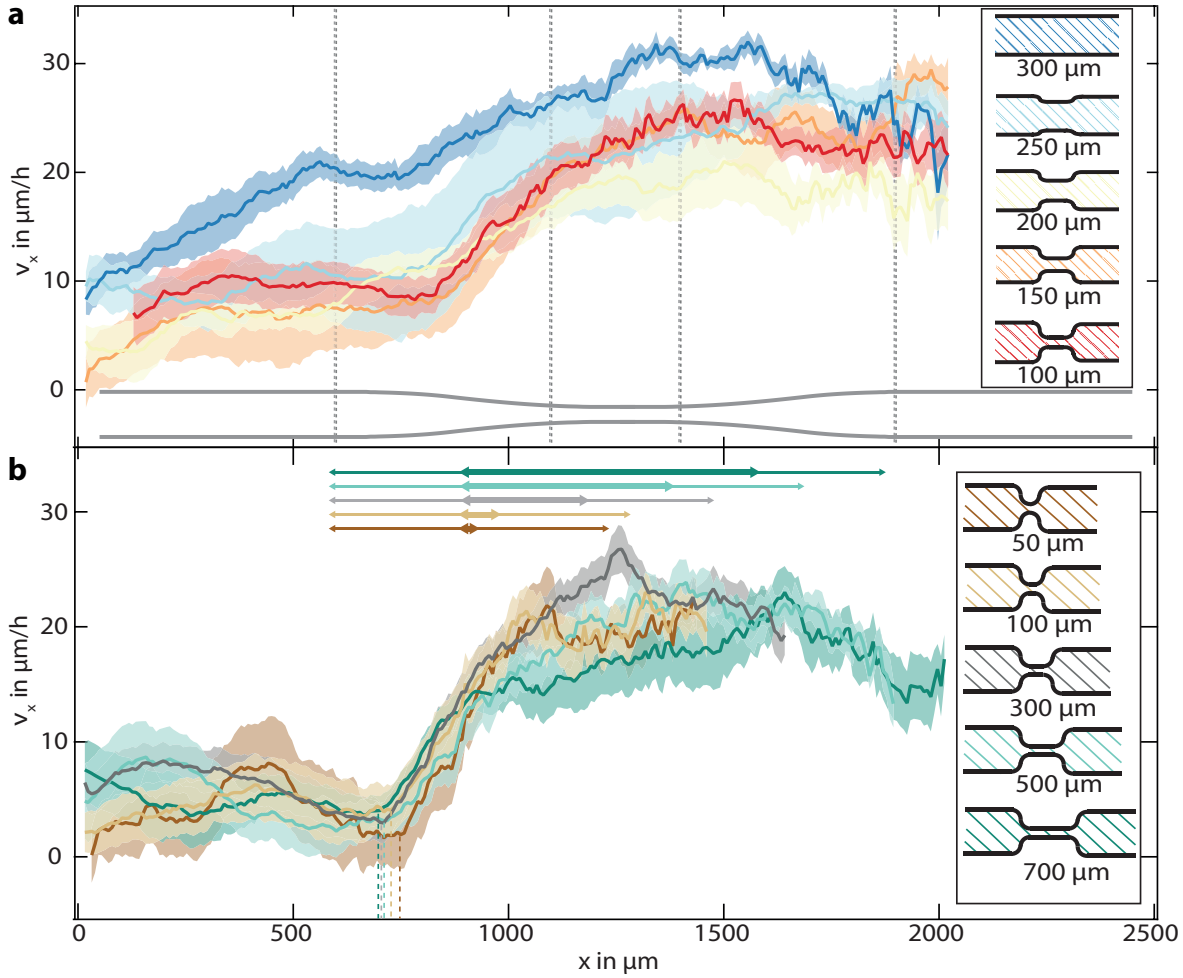

Figure 7.4.: Velocity in x direction of cell sheet 250 μm after the constriction for different geometries. **(a)** Introduction of constriction leads to emergence of a velocity plateau. Dark blue shows the typical velocity profile for a channel without constriction with movement speed increasing steadily towards the cell front, before declining slightly. All other geometries narrow down into a constriction at dotted grey lines as indicated in the schematic channel drawing below the curves. All geometries vary from each other only by narrowness of constriction. **(b)** Velocity plateau seems independent of lengths of constriction. Differently to the geometries of plot (a), transition regions from full width to minimal diameter are reduced from 500 μm to 300 μm, resulting in a completely independent second set of geometries. Geometries in this subplot only vary to each other in length of constriction resulting in curves of different lengths. Arrows above the curves indicate onset of transition into the constriction, bold arrow corresponds to length of minimal width. Dotted lines below the curves indicate end of the plateau. For 50 μm to 700 μm no accumulation of jamming is observed and velocity plateaus are similar within the error margin. Shaded regions indicate standard errors of the mean.
Plots courtesy of Matthias Zorn, adapted with permission from [117].

7.2. Cell Migration in Experiment and Simulation

As already discussed in modelling chapter 2.3 and summarized in Fig. 2.6, previous attempts to describe cell motion through a constriction by an active nematic liquid crystal model failed to reproduce the characteristic flow direction.

Another approach to model collective movement at single cell resolution is cellular Potts models (CPM). CPMs are used to reproduce collective motion in cellular monolayers [130, 131], investigate glass-transitions from fluid- to solid-like behaviour [132] and bridge the scale from single cell migration to large collectives [33]. The cellular Potts model also proved a versatile tool to investigate cell migration described in previous chapters 3 and 4.

Cellular Potts Model in Narrowing Channels

Kempf *et al.* have investigated collective flows through constrictions using a CPM [137]. Their model is compared to experiments in the following.

In experiment as well as simulation, cells are seeded in a reservoir and divide there until a confluent layer is reached. Only then, the entrance to the channel is opened and cells start invading into it. Cell division rates balance invasion speed such that no gaps in the moving cell sheet occur. Images for an advanced cell sheet in simulation and experiment are shown in Fig. 7.5.

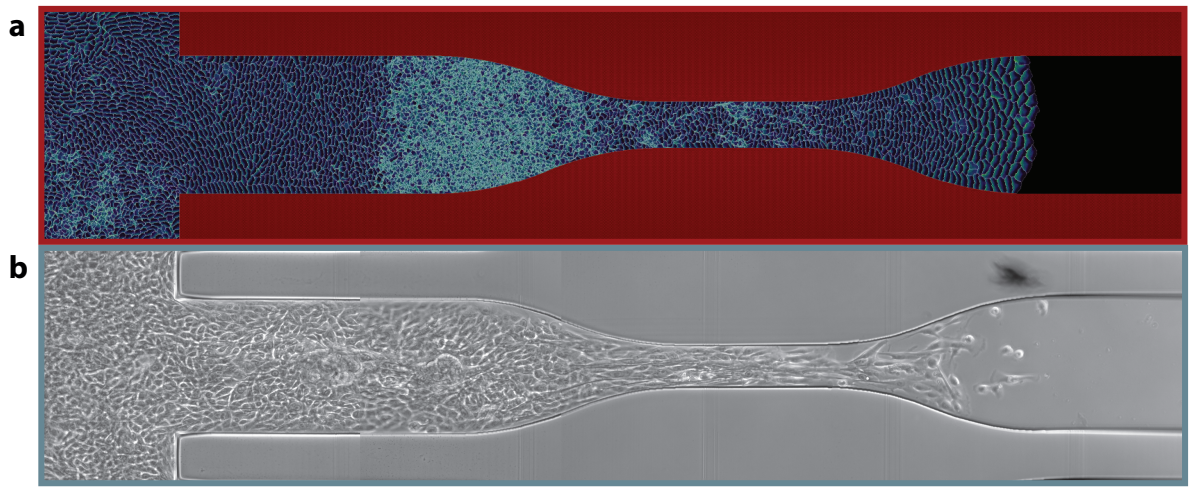

Figure 7.5.: Cells invading a constriction from the left. **(a)** Simulated by a CPM. Image courtesy of Felix Kempf. **(b)** Phase contrast image of fixed MCF10A cells.

From initial observation, for the CPM cell sizes seem smaller than in experiment and cells are tightly connected. In experiment, cells at the leading edge sometimes escape the sheet and move in front as they are only loosely connected. This may already indicate some differences that will be explored in more detail in the following.

Densities throughout the Channel

To compare the general distribution of cells, density and the respective single cell size, Fig.7.6 shows cell numbers for simulation and cell nuclei in experiment.

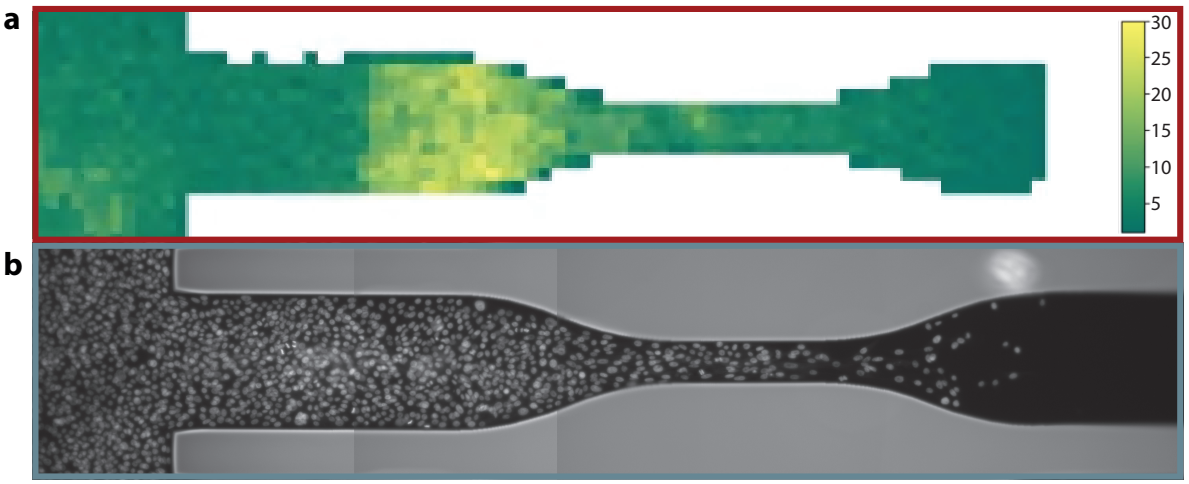

Figure 7.6.: Cell density throughout the channel. **(a)** Simulated by a CPM. High densities left in front of the constriction. Image courtesy of Felix Kempf. **(b)** Cell nuclei visualized by a DAPI stain on fixed MCF10A cells. High densities in the whole cell sheet before the constriction.

In simulation, cell numbers are highly increased before the constriction. Inside the constriction and in the reservoir, cells are a little more compacted than in the rest of the sheet, but this effect only seems minor. In comparison, the stained cell nuclei in experiment show that cells are most dense before the constriction as well and even show three dimensional stacking. In the constriction, cells are already less dense than left of it and density even further decreases after it, similarly to simulation. From the density profile inside the channel with high density in front of the constriction, reduced cell velocities can be expected caused by cell jamming. The observed densities also could explain why the drop in velocity profiles in front of the constriction only emerges after the cells have invaded much further into the channel, as only now density in front of the constriction is explicitly higher than inside the constriction and behind it. However, so far we can only speculate that the evolved density profile is caused mainly by cell-cell adhesion compressing cells, as it is quite well reproduced by the CPM which includes no more advanced cell-cell interaction terms such as for instance cell stresses communicated over several cells contracting the whole sheet.

Flow Velocities inside the Channel

As elucidated by Fig 7.4, a key feature of collective migration through a constriction in experiment is the plateau of reduced velocity before the constriction that emerges when the cell front has reached far into the channel. Fig. 7.7 depicts heatmaps of velocities parallel to the channel for simulation (a) and experiment (b).

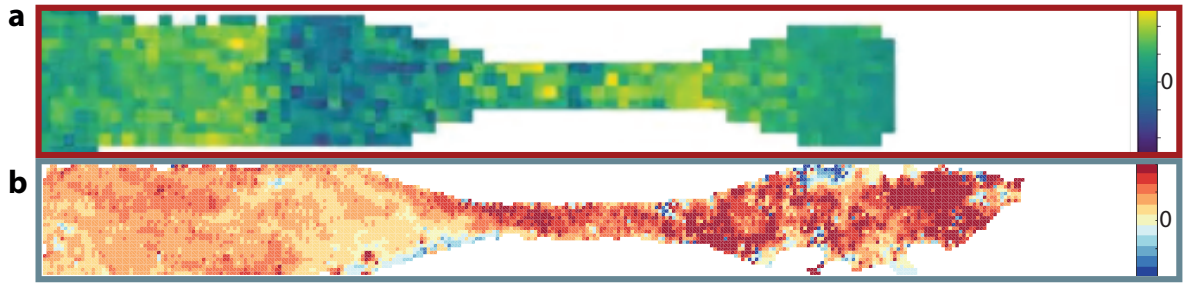

Figure 7.7.: Magnitude of velocity component of cells parallel to the channel. **(a)** Simulated by a CPM. Region of backflow left of the constriction, smaller velocities right of it. Image courtesy of Felix Kempf. **(b)** Heatmap of MCF10A cells. No wide prominent regions of strong backflow but overall higher velocities inside and right of the constriction. Image courtesy of Matthias Zorn, adapted with permission from [117].

Interestingly, CPM and experiment paint a very different picture in terms of velocity. For the simulation, in front of the constriction maximal velocity amplitudes are observed with cells displaying strong backflow in the narrowing channel section and high velocities in main movement direction in the region of full width. Inside the constriction, cells still migrate in both directions at high velocities. After the constriction, cells advance at homogeneous intermediate velocity into main movement direction. In contrast, in experiment cells display the previously described velocity profile with smaller velocities before the constriction and increasing velocity from constriction entrance to cell front. The backflow observed in simulation in front of the constriction is only present at the very side of the narrowing segment in this explicit experiment displayed and probably not a common reproducible feature. Inside the constriction, behaviour of simulation and experiment is the most similar, as cells migrate at increased velocities. After the constriction, cells in experiment show inhomogeneous migration at high velocity in all directions whereas in simulation cells immediately slow down and migrate very cohesively at medium speed. This presents a fundamental difference.

7.3. Discussion

In this chapter, collective migration through constrictions has been explored experimentally and compared to simulations with a CPM. In experiment, cells show a plateau of reduced velocity in front of the constriction that only evolves after the cell front has already left the constriction and moved 250 μm further into the channel. Starting roughly from the constriction, increasing velocities towards the front are observed. These dynamics are stable over different constriction widths as well as different lengths of the constriction. Cell density seems to coincide with reduced velocity, indicating jamming as a possible explanation for the velocity plateau, as observed in [214]. This would also explain the delayed onset of reduced velocity, as cells need to jam up in front of the constriction first.

In simulation, cell distribution and density is quite well comparable to experiment although cells are a little smaller in simulation and no cells escape the cell sheet. This may indicate cell-cell adhesion to be stronger than in experiment. However, when comparing cell velocities fundamental deviations of simulation from experiment indicate intrinsic differences. While densely packed cells in experiment show reduced speeds, the opposite holds true for simulation where velocity amplitudes are higher in more dense parts of the cell sheet. Especially right in front of the constriction where cells are most tightly jammed in simulation even a high velocity backflow is observed over the whole width of the channel. Cells in simulation do not show any slowing at higher confinement which is a strong contrast to biological observations and other implementations of the model [132]. Kempf *et al.* show, however, that for a different set of parameters and a comparable geometry they do observe a plateau of reduced velocity in front of the constriction [137]. They do not see the characteristic monotonous speeding of cells through the constriction to up the cell front as in experiments but an immediate speeding inside the constriction followed by a sharp drop at widening of the channel.

For better comparability between experiment and simulation, as a first step, cell size in simulation could be adjusted to fit the experimental relative confinement sizes of about 15 cells in the wide part of the channel and at most 5 cells inside the constriction. Also cell-cell adhesion could be varied in simulation until cells are as loosely connected as in experiment with single cells detaching from the front sometimes. This could also lead to a less ordered invasion after the constriction as it is observed in experiment. It could be worth attempting to determine all parameters via the stepwise calibration method proposed in chapter 4 supplemented by two cells on a dumbbell to access adhesion between cells, as applied in chapter 6. In experiment, a stable nucleus label could allow much better monitoring of cell densities during the measurement than a simple fixation and staining at the end. Furthermore, targeting cell-cell contacts by antibodies or knockouts of cell-cell-interaction proteins, e.g. E-Cadherin or ephrin-A2 as investigated in chapter 6, could allow further investigation of communication pathways in jamming.

Another interesting aspect for comparison could be cell size and shape, as Atia *et al.* find that cell shape and variability seem constrained by an universal geometrical relation only [215]. For simulations, this observable is easily extractable, whereas in experiment a cell membrane marker would be needed. Testing this hypothesis for cells migrating through constrictions could add further insight into the universality of this phenomenon and presents an additional aspect for comparison.

In conclusion, upon introduction of a constriction into the straight channel the description of an invading cell sheet by classic hydrodynamic laws breaks down and we observe a characteristic velocity profile along the channel that is robust against variations in geometry but seems to be density dependent. Furthermore, collective migration of cells presents characteristic dynamics which could not yet be described by the active nematic model or CPM presented here and thus require further fine-tuning.

8. Conclusion and Future Prospects

In this thesis, cell migration on micropatterns was studied. Cell polarization and resulting morphodynamics have been quantitatively compared to models. Cells were shown to exhibit distinct types of motion depending on the confining geometry. By accessing cell position by tracking of the cell nucleus, cell movement was observed for up to 72 hours allowing the observation of emergent migratory phenomena provoked by geometric constraints.

At the confinement of cellular motion to stripes of finite length in chapter 3, repeated quenching and re-establishment of migration was observed. We found this phenomenon of quasi-oscillatory motion to be stable over various lengths of stripes. Here, the time spent in the cell tip during turning as well as the migratory speed at the tip centre were not influenced by overall stripe length. For differently curved tips of stripes (concave, convex, blunt and pointed) neither velocities nor reversal times changed either. Our study showed the reversal time at a dead end of cell migration to have a duration conserved over various changes in geometric details making it a suitable basis for model testing. We compared our experimental findings with a cellular Potts model (CPM). Although stochasticity in distributions of velocity and reversal times was greatly reduced, the model was capable to nicely reproduce the insensitivity to geometric detail. Taking a look at the spatial distribution of actin during quenching of polarization, we found experiments to show a geometry-dependent pattern that could not be fully captured by the model.

Intrigued by the versatility of CPMs [33, 134, 216, 31] and the possibility to extract hallmarks of cellular behaviour from carefully chosen micro-confinements [36, 26, 162, 136], we successively calibrated a CPM to mimic cellular behaviour in chapter 4. Our study showed a rational approach to link computational parameters to experimental observables by confinement to geometries with orthogonal properties. Thus, the high dimensional optimization problem can be reduced to distinct linear distances that by stepwise revision yield a fully calibrated set of CPM parameters. This model is capable to reproduce all experiments used for parameter determination and furthermore shows predictive capability on novel geometries. Thereby, we showed that on a mesoscale cellular behaviour can be abstracted to a scalar polarization field with symmetric feedback upon retraction and protrusion without the explicit implementation of biochemical signalling pathways.

Given the quantitative differences in prediction, an explicit inclusion of cellular regulatory mechanisms into the CPM could further improve the accuracy. Promising networks that govern cellular behaviour are the adhesion to the substrate and the Rho GTPase network of polarization. For correct implementation, we started to investigate the visualization of polarization by fluorescent labelling of early markers of polarization, e.g. Rac1 and Vasp, as shown in Fig 8.1. Further and more thorough collaboration with a biological department could provide a stable cell line expressing a Förster res-

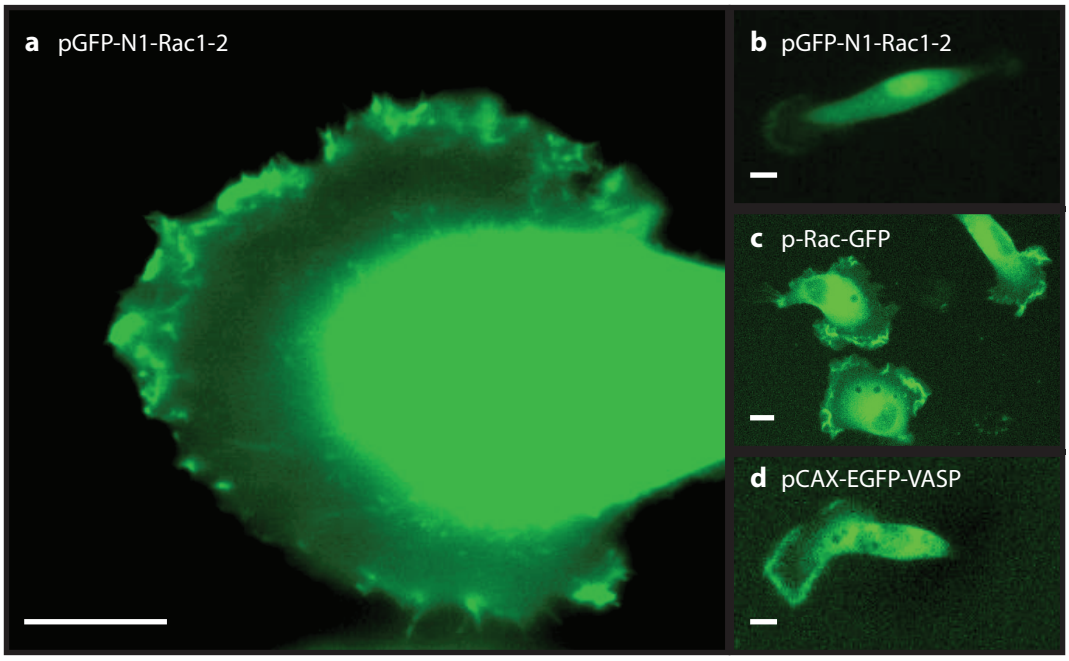

Figure 8.1.: Fluorescent markers for early polarization in MDA-MB-231. **(a)** and **(b)** show cells expressing a pGFP-N1-Rac1-2 in house cloned plasmid. **(c)** shows a cell expressing a p-Rac-GFP plasmid, kind gift of the group of Stefan Zahler, Department of Pharmacy at LMU. **(d)** depicts a cell transfected with a pCAX-EGFP-Vasp plasmid, kind gift of the group of Michael Sixt at IST-Austria. Scale bar = 10 μm.

onance energy transfer (FRET) sensor for Rac1 activity to help elucidate its exact spatio-temporal contribution in the different confining geometries. This knowledge together with more information on the adhesion regulation could provide enough detail for the implementation of two distinct fields in the CPM, one for substrate adhesion and one for polarization. A biologically more accurate representation could lead to a more quantitative than qualitative accuracy of the model and could allow for the comparison of different cell lines or mutants thus providing a platform to conclude from differences in gene expression levels to changes in migratory behaviour.

Another feature of cell migration we investigated in chapter 5 of this study is the movement of cells through mazes. Here, cellular motion is simplified into discrete left-right decisions and compared to stochastic models in chapter 5. This simplification of cellular motion from a persistent random walk process to discrete outcomes opens up the whole field of Bernoulli models for comparison that commonly have variables that are interpretable in a very intuitive fashion. Our study showed that migration through mazes is no independent unbiased decision process but can be described by a model including a proportional change in decision probability and a temporal degradation thereof.

Combining our finding with a close spatio-temporal analysis of the decision process, deeper elucidation on the dynamics that leads to taking a left or right turn could be obtained. Labelling various components of cell machinery known for polarization

signalling, e.g. Rac1, or the cytoskeletal machinery, e.g. the microtubuli organizing centre, could help to further understand how cells decide for a direction. Combination of this geometry with experiments on a lane of finite length as in chapter 3 might allow insights into the process of cell reversal and redirection of polarization. This experimental setup could be further used to characterize the role of various components of the molecular machinery in migration and reversal. A molecular motor of interest could be MyosinVI (myo6), located at the leading edge of a cell. We studied the localization of this motor on a dumbbell with nano-rippels, as shown in Fig 8.2.

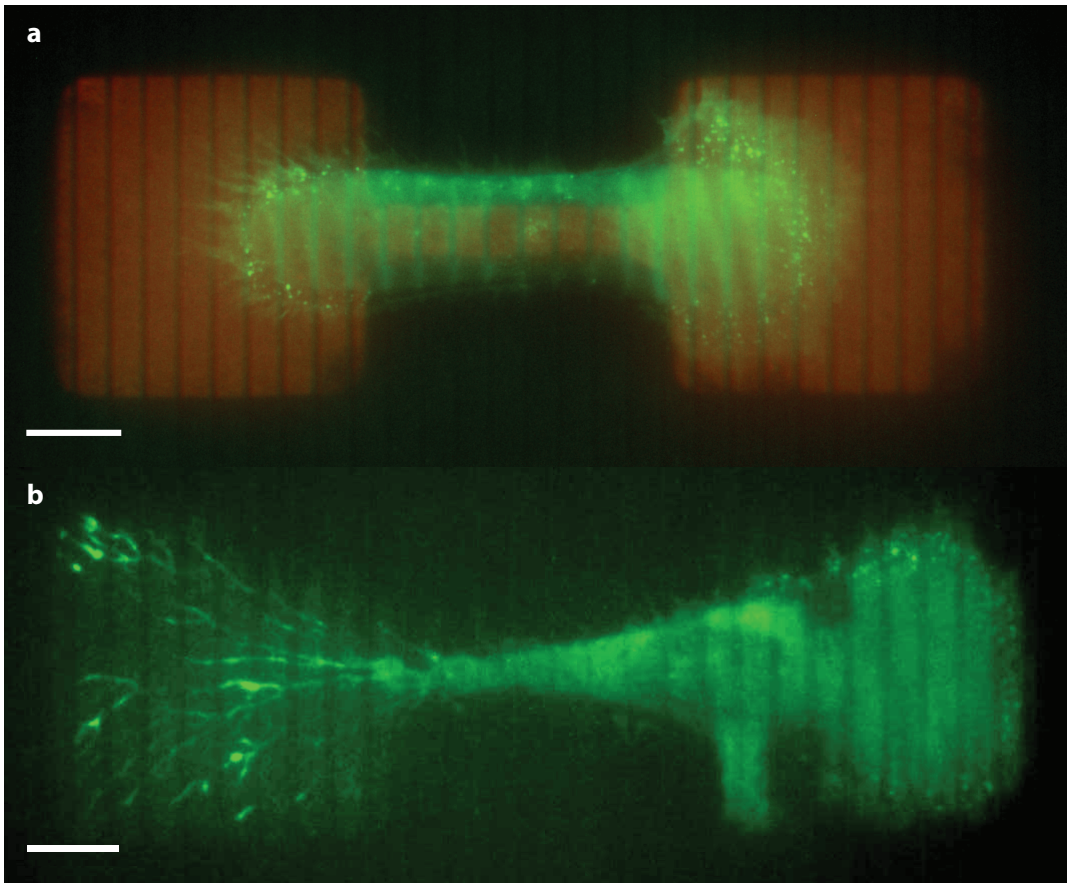

Figure 8.2.: MyosinVI-GFP expressing RPE cell on dumbbell with 60 nm rippels. Pattern visualized by Alexa647-labelled fibronectin. Scale bar = 10 μm. **(a)** Fluorescence microscopic image of a cell transitioning from one adhesive site to the other. **(b)** TIRF image of a transitioning cell shows spreading of filopodia over the whole pattern with enhanced MyosinVI activity. Cells were a gift from the group of Claudia Veigel at the Biomedical Center Munich, LMU.

Although we could not determine the effect of myo6 on transition of cells from one side of the dumbbell to the other, we expect the maze and finite lane geometries to be far more suited to investigate the myo6 localization during redirection or quenching of polarization. In combination with a knockout mutant of myo6, comparison of cellular behaviour of wildtype and knockout combined with the knowledge of localization of myo6, gained by the myo6-GFP mutant, could help to better understand its role in

migration.

As myo6 is known to form a complex with β catenin and E-Cadherin, the experimental setup described in chapter 6 could be used to investigate its role in cell-cell communication. Applying the previously proposed "cell collider", our study showed E-Cadherin to be of great importance for cell-cell communication. Non-cancerogenic cells, MCF10As, were treated with a functional E-Cadherin antibody blocking cell-cell contacts based on E-Cadherin. We could show that the two-cell dynamics on a dumbbell evolved to become more similar to a highly invasive, cancerous cell line, namely MDA-MB-231. Our study thus provides evidence for the crucial role of E-Cadherin in maintaining a non-cancerous migratory phenotype for the two cell lines compared here. For Ephrin A2, we could observe a even more invasive behaviour in the cancerous cell line upon addition of the Ephrin A2 antibody.

This setup could provide a platform to quantitatively screen the role of various proteins involved in cell-cell communication in a high-throughput fashion. Further proteins of interest could be of the Rho GTPase family regulating polarization, e.g. ROCK, or the cytoskeletal machinery, e.g. myo6. Furthermore, heterotypic experiments of two different cell types could allow the observation of a minimal invasion interaction of one malignant, cancerous cell and a cell of the surrounding tissue in a repeated, well defined and reproducible fashion.

Not only can cell-cell communication dependent on mechanical or biochemical signalling be investigated, but also the dependence of cell dynamics on the substrate. A suitable platform to generate variations of the same confining structure is photolithography, e.g. Laser-Assisted Protein Adsorption by Photobleaching (LAPAP), as shown in Fig 8.3. Structuring surfaces with LAPAP achieved good results for single exposure patterns. Using an alignment frame and suitable markers for position, two successive steps in patterning can be achieved and thus the possibility to link two different adhesion sequences is given. Also first trials on the structuring of non-rigid surfaces with LAPAP have been performed. Here, surface chemistry and stickiness have to be improved to allow for non-deformed patterns with a high signal to noise ratio.

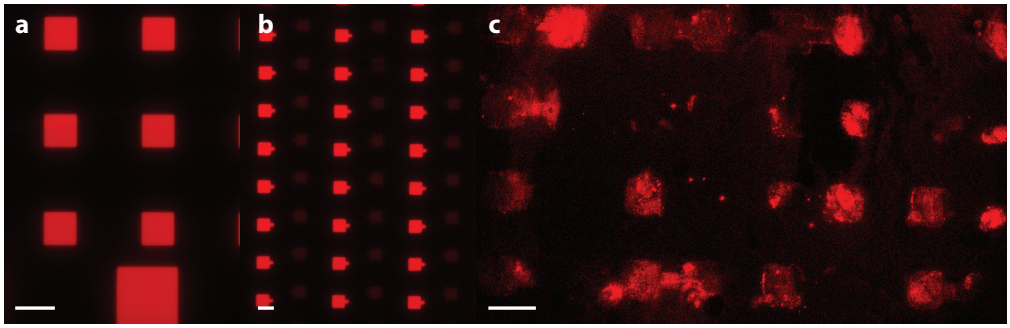

Figure 8.3.: Various structures produced with LAPAP. Scale bar = 50 μm. **(a)** Squares of different sizes. **(b)** Half a dumbbell and dark shadow of another half dumbbell. **(c)** First tries on dumbbells on SoftPDMS, protocol by Aurélie Dupont, Laboratoire interdisciplinaire de Physique, Université Grenoble Alpes [217].

Taking cellular interaction to a bigger scale in chapter 7, we investigated collective migration through a constriction and found that neither a phase-field model nor a CPM were capable to reproduce the characteristic velocity profile throughout the channel. For future experiments, the dependence of jamming on cell density could be further explored by performing time-lapse measurements of cells with a nucleus label. Futhermore, the density evolution inside the channel could be further investigated whether cell division or influx from the reservoir are the driving force.

All in all, the results of this thesis contribute to deepening the understanding of cellular migration and signalling. We have shown how confinement of cells to microstructures provides a versatile platform to easily access different aspects of cell migration in a well-defined and reproducible manner. Our proposed platforms for further investigation of biochemical networks can help to unravel a part of the highly complex regulatory mechanism that governs cytoskeletal dynamics during cell migration and that has been subject to researchers from various fields for a long time.

> *Es ist ein wesentlicher Vorzug unseres Zeitalters, dafs die einzelnen Disziplinen der Naturwissenschaften in immer innigere Vereinigung miteinander treten, und gerade dieser wechselseitigen Durchdringung und Ergänzung verdanken wir einen grofsen Theil der Fortschritte, welche die Naturwissenschaften in der neuesten Zeit gemacht haben.*
>
> Theodor Schwann
> "Mikroskopische Untersuchungen über die Uebereinstimmung in der Struktur und dem Wachsthum der Thiere und Pflanzen"
> Berlin, 1839

A. Materials and Methods

This section will give a short overview of the protocols and cells used in this thesis. Table A.1 shows a overview of cell lines, microstructuring methods, microscopes, experimental details and image analysis used in each chapter of this thesis and further elaborated in the following sections.

Table A.1.: Overview of cell lines, patterning, microscopes, experimental details and image analysis.

Chapter	Cell Lines	Patterning	Microscope	Specifics	Image Analysis
3	MDA-MB-231	μCP	see Zhou *et al.* [136]		
4, free cell	MDA-MB-436	none	Nikon Ti	yes, see below	see B.2
4, stripe	MDA-MB-436	μCP	Nikon Ti	-	see B.1
4, donut	MDA-MB-436	μCP	see Schreiber *et al.* [162]		
4, gap	MDA-MB-436	μCP	see Schreiber *et al.* [162]		
4, dumbbell	MDA-MB-436	μPIPP	as in Fink *et al.* [163]		
5	MDA-MB-231	μCP	Nikon Ti	-	see B.3
6	MDA-MB-231	μPIPP	as in Brückner *et al.* [34]		
7	MCF10A	3D moulding	see Zorn [117]		
8	MDA-MB-231, RPE	μCP, LAPAP	Nikon Ti	yes, see below	-

A.1. Cell Confinement

As described in section 2.4, there are various possibilities to confine cells to geometric shapes of choice, of which four have been used in this thesis. Two confinement approaches, microscale plasma-initiated protein patterning (μPIPP) and microcontact printing (μCP) restrict single cells to 2D micropatterns by a fibronectin coated, thus adhesive area and a PLL-PEG coated, cell repellent surrounding. The two approaches differ in two details: First, for μPIPP the microstructure is afterwards visible in phase contrast microscopy whereas for μCP a part of the fibronectin has to be labelled by a fluorophore to ensure position and quality. Second, μPIPP cannot be used for closed structures such as a ring-shaped geometry as the centre part would not be passivated resulting in a circle instead of a ring. However, for only qualitative confinement of cells to micropatterns no difference between these two methods has been observed. The protocols for fabrication can be found in Segerer *et al.* [150] for μPIPP and Schreiber *et al.* [162] for μCP. For multicellular experiments, cell were confined to three dimensional structures cast from a PDMS stamp using PEG-DMA and a cell-adhesive dish [168]. The exact protocol can be found in detail in Zorn [117]. The fourth approach for cell confinement is Laser-Assisted Protein Adsorption by Photobleaching (LAPAP). There, a chrome mask is used for spatially defined photobleaching and adsorption of a fluorophore to a cell-repellent surface. A click-chemistry anchor allows covalent binding of RGD-sequences as described by Bélisle *et al.* [151]. So far, there is no standard protocol as the patterns shown here still are subject to optimization.

A.2. Cell Lines and Culture

Throughout this thesis, different cell lines are used as shown in Table A.1 and briefly described below.

Cell Culture

All cell lines were kept at cultivating conditions annotated to their brief profiles and passaged every 2-3 days. If not stated otherwise, cells were washed with PBS, detached using Accutase and incubated at 37°C until they rounded up (for most cell lines used this takes 2 min, for MCF10A >15min). Afterwards the culture flask was gently patted to detach the cells, resuspended with 2 ml culture medium and the flask was thoroughly rinsed with the cell suspension to detach all remaining cells. During centrifugation for 3 min at 800 rcf the cell number was determined using a Neubauer counting chamber. The supernatant was carefully aspirated and the cell pellet was resuspended in 3 ml culture medium. Then, cells were seeded in the amount stated in their profiles.

Cell Lines

- MDA-MB-231
  - Cellosaurus Identifier: CVCL_0062
  - Short Description: highly invasive breast cancer cell line
  - Culture Medium: L15 with 10% fetal bovine serum (FBS)
  - Culture Conditions: 37°C and 0% CO_2
  - Average Generation Time: 30 hours
  - Seeding number in T25 for 2 / 3 days: $3.5 \cdot 10^5$ / $2.25 \cdot 10^5$
  - Typical Morphology, 5x and 20x phase contrast

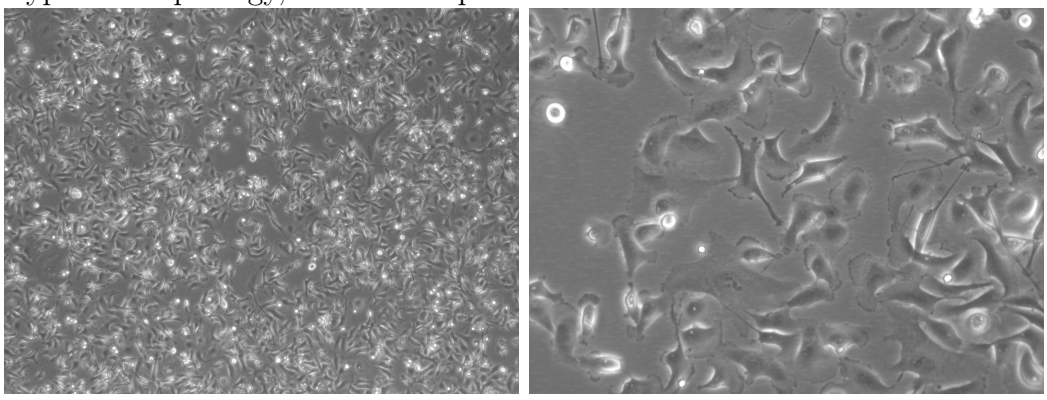

- MDA-MB-436
  - Cellosaurus Identifier: CVCL_0623
  - Short Description: invasive breast cancer cell line
  - Culture Medium: L15 with 10% FBS
  - Culture Conditions: 37°C and 5% CO_2, one week in same flask

- Average Generation Time: 60 hours
- Seeding number in T25 for 2 / 3 days: $4.2 \cdot 10^5$ / $3.7 \cdot 10^5$
- Typical Morphology, 5x and 20x phase contrast

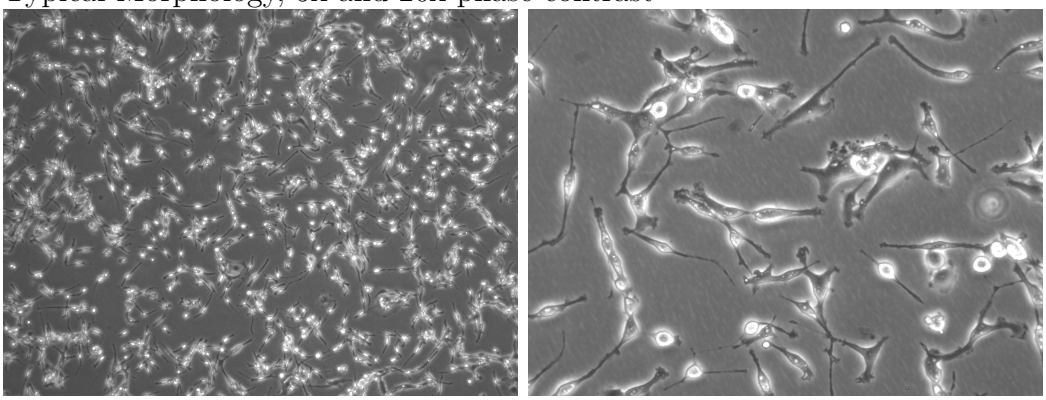

- MCF10A
  - Cellosaurus Identifier: CVCL_0598
  - Short Description: Fibroblastic disease cell line
  - Culture Medium: DMEM:F12 with 5% horse serum, $10\frac{\mu g}{ml}$ insulin, $20\frac{ng}{ml}$ hEGF, $0.5\ \frac{\mu g}{ml}$ hydrocortison, $100\frac{ng}{ml}$ cholera toxin
  - Culture Conditions: 37°C and 5% CO_2
  - Average Generation Time: 48 hours
  - Seeding number in T25 for 2 / 3 days: $5.1 \cdot 10^5$ / $4.3 \cdot 10^5$
  - Typical Morphology, 5x and 20x phase contrast

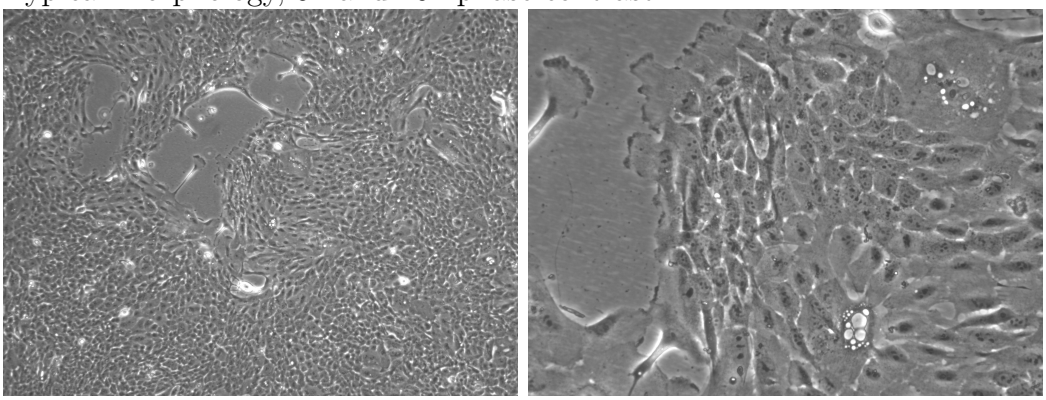

- RPE
  - Cellosaurus Identifier: CVCL_0145
  - Short Description: Human Retinal Epithelium cell line
  - Culture Medium: DMEM:F12 with 10% FBS
  - Culture Conditions: 37°C and 5% CO_2
  - Average Generation Time: 24 hours
  - Seeding number in T25 for 2 / 3 days: $3.5 \cdot 10^5$ / $2.0 \cdot 10^5$

- Typical Morphology, 5x and 20x phase contrast

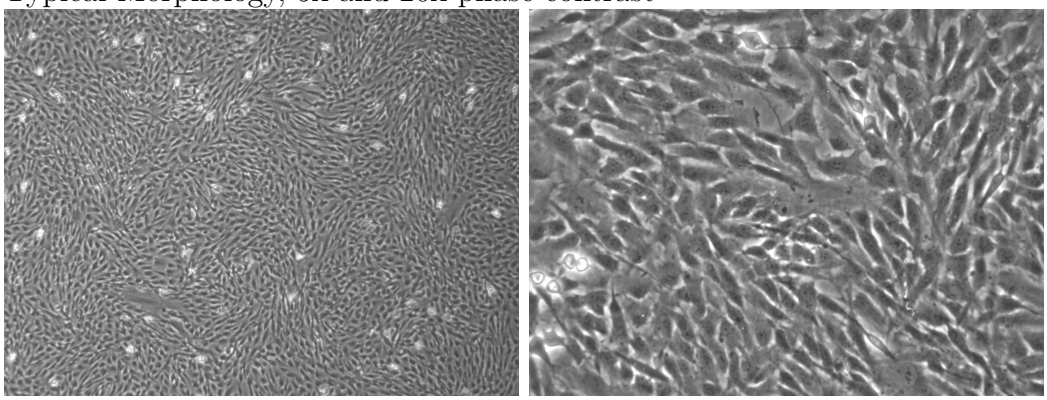

A.3. Microscopes

If not indicated otherwise, all experiments were performed on a Nikon Ti Eclipse setup with 10x and 20x Nikon phase-contrast objectives or a 60x Nikon oil immersion TIRF objective and a Lumencor Spectra-X or Nikon mercury fibre illuminator as fluorescence excitation source. The microscopes were equipped with a pco.edge 4.2 LT sCMOS camera and a large Okolab10 incubation box with gas mixer. For the recording of the fluorescence of the stained cell nuclei, images were recorded at 2x2 binning to reduce photo damage by enabling shorter exposure times. To record many cells in parallel, automated scanning time-lapse measurements were performed at an imaging rate of 10 min in phase contrast and cell fluorescence. Experiments were performed for a duration of 24 to 72 hours and about a hundred positions were imaged. For experiments in chapters 4 and 5, fluorescent micropatterns were recorded once at the beginning of the measurement. Exposure times were chosen such that cells still were vital at the end of the measurement.

A.4. Experimental Procedure

If not indicated otherwise, all experiments were performed in L15 without phenol red supplemented with 10% FBS, at 0% CO_2 and 37°C, except for experiments involving MCF10A that were performed in the medium composition for MCF10A without phenol red at 10% CO_2 and 37°C. After cell passaging, the remaining cell suspension was used to seed about 7500 cells onto the microstructures fabricated the day before and stored over night under PBS at 4°C. The PBS was removed and 1 ml of cell culture medium was added to the 60μ ibidi dishes the cell suspension was distributed equally over the dish and swayed in a eight-shape to ensure even cell distribution. Cells were allowed to adhere to the pattern for about 3 hours under cultivation conditions. Afterwards, the medium was very carefully exchanged for the imaging medium and a cell stain could be added, see next section. Cells were carefully transferred to the preheated microscope, allowed to equilibrate for one hour and the measurement was set up.

A.5. Labelling and Transfection

For chapter 5, a MDA-MB-231 cell line stably expressing a H2B-mcherry marker was used, so no additional nucleus stain was needed. All other single cell experiments in chapters 3 to 6 were conducted with an addition of a final concentration of 25nM Hoechst 33342 to the imaging medium leading to a fluorescence signal of the nuclei within 1 hour after medium exchange. The antibodies used in chapter 5 were added with the imaging medium at 5 $\frac{\mu g}{ml}$ for CD324 (E-Cadherin) Monoclonal Antibody (DECMA-1) and 1 $\frac{\mu g}{ml}$ for Ephrin A2 Monoclonal Antibody (OTI3E3).

For the transfection of the polarization markers in chapter 8, MDA-MB-231 cells were seeded two days prior to the experiment into a 60μ ibidi dish to be 70% confluent the next day in culturing conditions and medium. DNA plasmids were transfected using Lipofectamine2000 and Opti-MEM medium without any supplements. For lipoplex formation, 2 μl Lipofectamine2000 are diluted in 100 μl Opti-MEM. Then, 1 μg DNA is diluted in 100 μl Opti-MEM, added to the Lipo-mix and mixed well by pipetting. The lipoplexes are allowed to form for 5 minutes during which the cells are washed once with 1 ml PBS and covered in 300 μl Opti-MEM. The Lipo-DNA mix is evenly distributed over the cells and they are incubated for 6 hours at 37°C and 5% CO_2. Afterwards, the medium is exchanged for the usual cultivation medium and cells are allowed to recover over night. The next day, a cell suspension is fabricated analogously to passaging and seeded onto the structures of choice.

B. Image Processing

During the course of this thesis, routines for image analysis were developed that will be explained in the following.

B.1. Single Cell Geometries

For single cells on small micropatterns, a fully automated script for image analysis and nucleus tracking was established in python. First, the fluorescent image of the micropattern of a position is used to access the orientation of the structures and detect the exact positions of the single patterns. Second, the angle of orientation and exact positions are transferred to the fluorescent image of the cell nuclei and used to crop the position into single substructures, e.g. single stripes. On these single stripes, the number of nuclei is determined and if there is only one nucleus present, the centred coordinates are written to a .csv file. Last, the bright-field images are rotated and cropped accordingly to allow for manual validation of the tracking. The code was designed to run as robustly as possible compromising for sensitivity. Although almost all experiments could be analysed with the same set of parameters, for some positions a slight parameter adjustment was needed.

B.1.1. Pattern Recognition

The general workflow for first part of the analysis is depicted using an exemplary position in Fig B.1. Briefly summarized, the workflow uses several predefined functions of the image processing library OpenCV, version 3.2.0 [218].

The original image is background corrected by using the OpenCV fast denoising algorithm and a threshold is applied to cut off very bright inhomogeneities in the pattern. To improve contrast and brightness, a local histogram normalization of the image is applied by the CLAHE (Contrast Limited Adaptive Histogram Equalization) function of OpenCV. To detect the outlines of the structures, the Canny edge detection of OpenCV is applied that was first proposed by John Canny in 1986 [219]. On the detected edges, a Hough transform is used for the extraction of the overall rotation of the micropatterns. Now the main orientation axis of the structures is known, the image is rotated by the previously computed angle. As the image is now rotated, a previously prepared template of the single substructure, e.g. a stripe, is loaded and checked for matches using the OpenCV ”matchTemplate“ function. An area of interest around each possible stripe detection is set and all the marked areas are checked for matching with the template under the restriction of only one appearance. The centre of each stripe is calculated, plotted and annotated with the stripe number for later validation.

After the pattern image, we transfer the rotation and the localization of the stripes to the fluorescent images of the nucleus and the bright-field images of the cells.

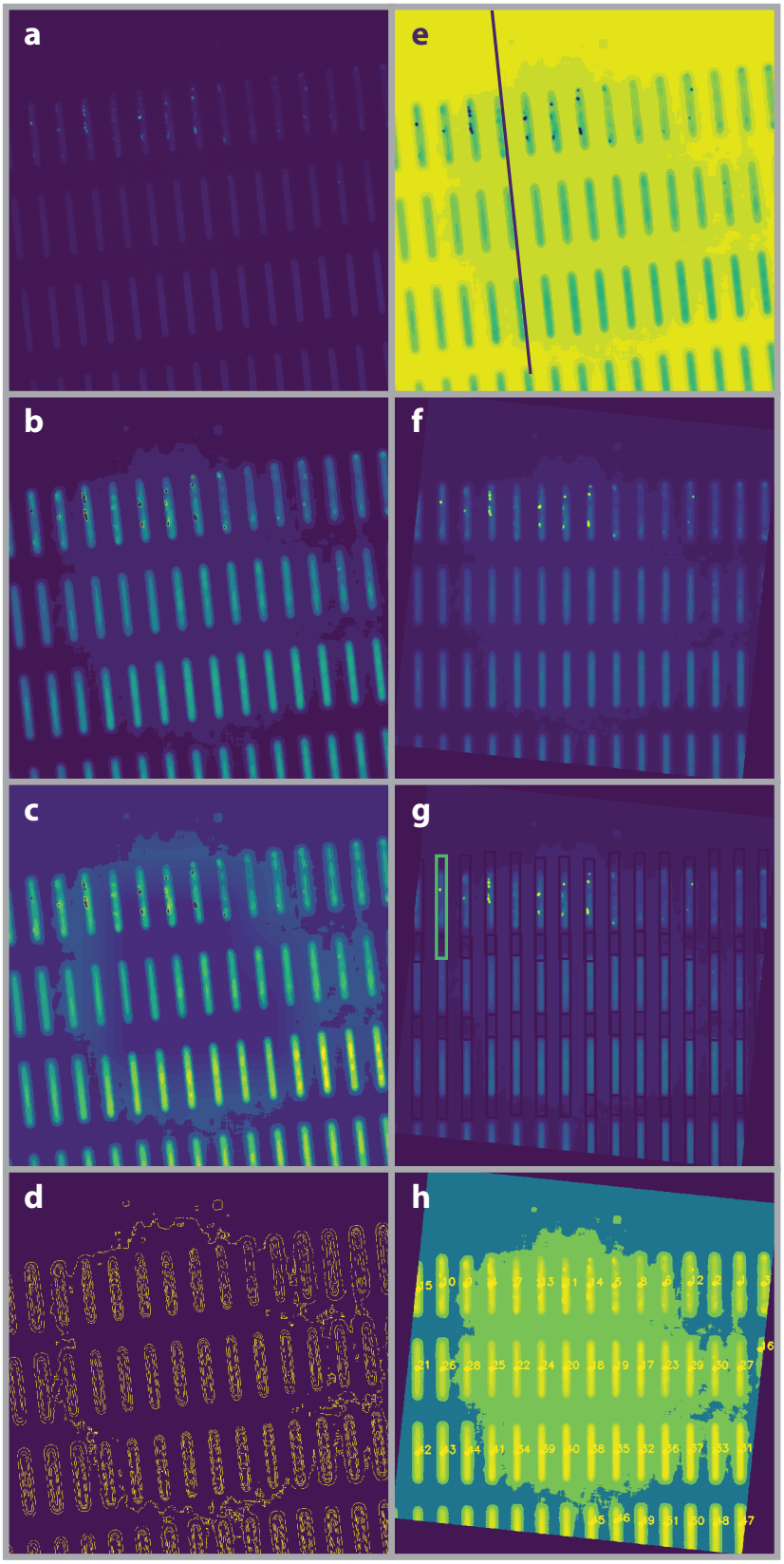

Figure B.1.: Workflow of image analysis for single pattern recognition. **(a)** Original image. **(b)** Threshold to reduce over-bright spots. **(c)** CLAHE improved image. **(d)** Canny edge detection. **(e)** Hough line transformation shows pattern direction by purple line. **(f)** Rotated image. **(g)** Detected single structures with region of interest, exemplarily coloured green. **(h)** Detected and numbered stripes.

B.1.2. Nucleus Tracking

The fluorescent image stacks of the cell nuclei are cropped into single stripes and processed subsequently. For each stripe position and time point, the Otsu method of thresholding is applied to binarize the image into pixels of nuclei and other. The number of unconnected nuclei islands is determined and for only one present nucleus, the centre of mass coordinates are written into a csv file. The cropped original fluorescence image and the binarized one are both saved for manual validation of the recognition process. Thus, all time points, single stripes and positions are analysed. The bright-field images is cropped and saved in the same directory that contains a unique identifier for position and single stripe.

For later analysis, for each position all stripes not fully in the field of view or stripes showing inhomogeneous fluorescence are excluded by denoting their number identifier in a separate file. For instance, in Fig B.1h the stripe numbers 1 to 16 and 45 to 51 would be excluded due to their position at the edge of the microstructured area or their being cut off.

Further analysis was performed with the software R that was used for trajectory filtering and all following data processing and visualization [220]. All trajectories containing a single nucleus were manually verified by looking at respective bright-field and nucleus image stacks to rule out mistakes in classification.

B.2. Cell Area and Perimeter

To determine the area and perimeter of freely moving cells, cells were transfected with a cytosol marker and imaged in the according fluorescence channel. These images were manually segmented into single cells. For the determination of the cell areas, a python script with a graphical user interface was programmed allowing for manual thresholding and automated image looping. The threshold for the fluorescent image was set to capture the whole cell body without the background and noise. All unconnected islands of pixels were determined and the biggest one was further regarded as cell body. Potential holes in the cell were closed using the morphological closing library of OpenCV and the obtained cell area was converted to μm^2 and saved. The perimeter was determined using the ”findContours“ function of OpenCV and the number of pixels of the unreduced contour was converted to μm and saved as perimeter. The next image was opened automatically saving a picture of the previous thresheld cell and final area and perimeter as shown in Fig B.2.

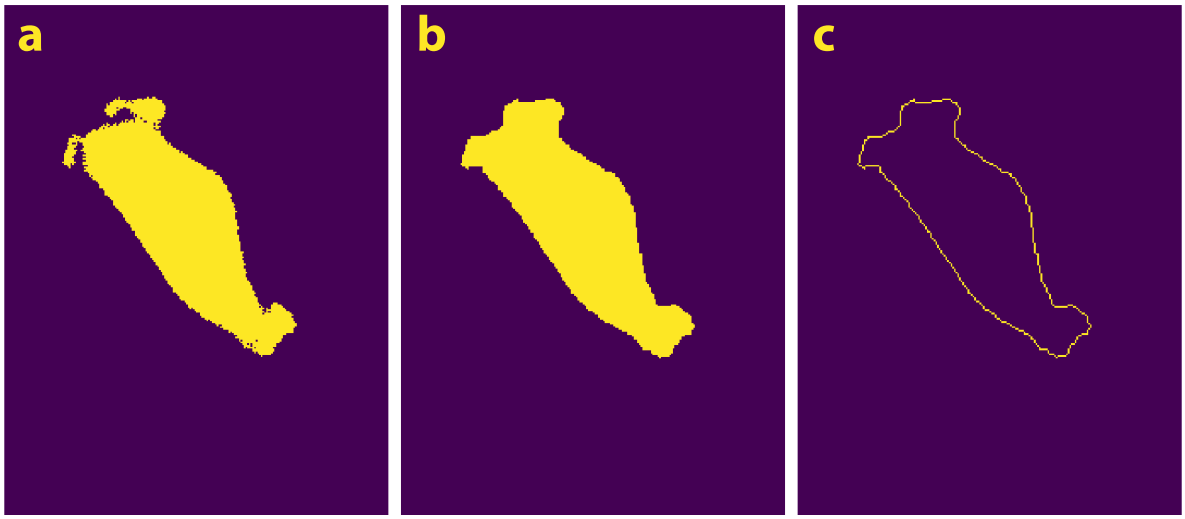

Figure B.2.: Area and Perimeter extraction from Fluorescence Images. **(a)** Thresheld image of the cell body. **(b)** Closed image and resulting area. **(c)** Extracted contour and resulting perimeter.

B.3. Mazes

The code for image analysis was implemented by Theresa-Maja E. Reitz as part of her Bachelor's thesis and was further refined during an employment as student assistant. The workflow is depicted in Fig B.3. For the analysis of cell migration through mazes, the cell nuclei were tracked using TrackMate, a plugin for Fiji [187, 221]. The obtained trajectories were interpolated to have connected paths of pixels and matched with a binarized image of the maze micropattern at this position. The orientation and change in angle of the pattern were determined by eye and lines for further automated processing were drawn as shown in Fig B.3b. The green line determines a left edge of the unit cells the pattern is subdivided into. The yellow line indicates the change in opening angle where the trajectories were reset. The blue line determines a right edge of the unit cells. Red and purple line indicate upper and lower edge of a unit cell. As the dimensions of the structures are known the pattern can be subdivided into unit cells with the help of the previously marked lines. Numbering the unit cells as shown in Fig B.3d, the trajectories can be analysed in terms of the unit cells they pass, compare Fig 5.2. A list of discrete left-right decisions is obtained for each trajectory.

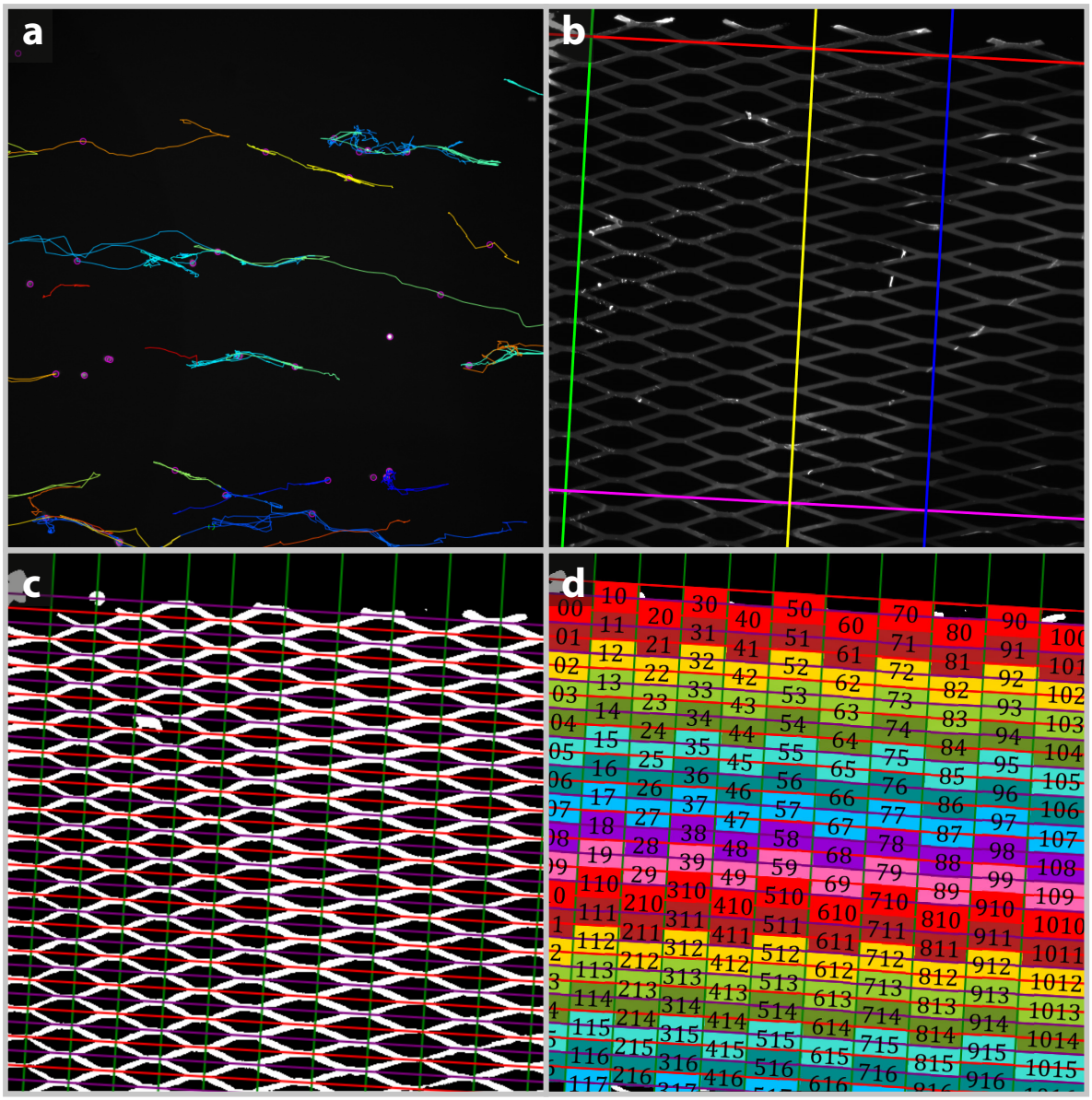

Figure B.3.: Workflow of image analysis for cell migration through mazees. **(a)** Trajectories obtained by TrackMate, colours indicate different cells. **(b)** Manual segmentation of micropattern for further automated analysis. **(c)** Automated image segmentation into unit cells. **(d)** Numbered and color coded unit cells for discretization of trajectories into decisions.

Bibliography

[1] Robert Hooke. *Micrographia or Some Physiological Descriptions of Minute Bodies Made by Magnifying Glasseswith Observations and Inquiries Thereupon.* Royal Society of London, 1665.

[2] Theodor Schwann. *Mikroskopische Untersuchungen über die Ubereinstimmung in der Struktur und dem Wachsthum der Tiere und Pflanzen.* Verlag der Sander'schen Buchhandlung (GE Reimer), 1839.

[3] Joseph-Claude-Anthelme Récamier. *Recherches sur le traitement du cancer, par la compression méthodique simple ou combinée, et sur l'histoire générale de la même maladie: suivies de notes, 1. sur les forces de la dynamétrie vitales; 2. sur l'nflammation de l'etat fébrile*, volume 2. Gabon, 1829.

[4] Melanie Rodrigues, Nina Kosaric, Clark A. Bonham, and Geoffrey C. Gurtner. Wound healing: A cellular perspective. *Physiological Reviews*, 99(1):665–706, jan 2019. doi:10.1152/physrev.00067.2017.

[5] Petra Kameritsch and Jörg Renkawitz. Principles of leukocyte migration strategies. *Trends in Cell Biology*, 30(10):818–832, oct 2020. doi:10.1016/j.tcb.2020.06.007.

[6] Jeffrey A. Farrell, Yiqun Wang, Samantha J. Riesenfeld, Karthik Shekhar, Aviv Regev, and Alexander F. Schier. Single-cell reconstruction of developmental trajectories during zebrafish embryogenesis. *Science*, 360(6392):eaar3131, apr 2018. doi:10.1126/science.aar3131.

[7] Gaorav P. Gupta and Joan Massagué. Cancer metastasis: Building a framework. *Cell*, 127(4):679–695, nov 2006. doi:10.1016/j.cell.2006.11.001.

[8] Statistisches Bundesamt (Destatis), February 2021. URL: https://www.destatis.de/DE/Presse/Pressemitteilungen/2021/02/PD21_N010_231.html.

[9] Peter Friedl and Stephanie Alexander. Cancer invasion and the microenvironment: Plasticity and reciprocity. *Cell*, 147(5):992–1009, nov 2011. doi:10.1016/j.cell.2011.11.016.

[10] A. J. Ridley. Cell migration: Integrating signals from front to back. *Science*, 302(5651):1704–1709, dec 2003. doi:10.1126/science.1092053.

[11] A. Hall. Rho GTPases and the actin cytoskeleton. *Science*, 279(5350):509–514, jan 1998. doi:10.1126/science.279.5350.509.

[12] Campbell D. Lawson and Anne J. Ridley. Rho GTPase signaling complexes in cell migration and invasion. *Journal of Cell Biology*, 217(2):447–457, dec 2017. doi:10.1083/jcb.201612069.

[13] Olga Ilina, Pavlo G. Gritsenko, Simon Syga, Jürgen Lippoldt, Caterina A. M. La Porta, Oleksandr Chepizhko, Steffen Grosser, Manon Vullings, Gert-Jan Bakker, Jörn Starruß, Peter Bult, Stefano Zapperi, Josef A. Käs, Andreas Deutsch, and Peter Friedl. Cell–cell adhesion and 3d matrix confinement determine jamming transitions in breast cancer invasion. *Nature Cell Biology*, 22(9):1103–1115, aug 2020. doi:10.1038/s41556-020-0552-6.

[14] Anna-Kristina Marel, Matthias Zorn, Christoph Klingner, Roland Wedlich-Söldner, Erwin Frey, and Joachim O. Rädler. Flow and diffusion in channel-guided cell migration. *Biophysical Journal*, 107(5):1054–1064, sep 2014. doi:10.1016/j.bpj.2014.07.017.

[15] Andrea J. Liu and Sidney R. Nagel. The jamming transition and the marginally jammed solid. *Annual Review of Condensed Matter Physics*, 1(1):347–369, aug 2010. doi:10.1146/annurev-conmatphys-070909-104045.

[16] Sriram Ramaswamy. The mechanics and statistics of active matter. *Annual Review of Condensed Matter Physics*, 1(1):323–345, aug 2010. doi:10.1146/annurev-conmatphys-070909-104101.

[17] S. R. K. Vedula, M. C. Leong, T. L. Lai, P. Hersen, A. J. Kabla, C. T. Lim, and B. Ladoux. Emerging modes of collective cell migration induced by geometrical constraints. *Proceedings of the National Academy of Sciences*, 109(32):12974–12979, jul 2012. doi:10.1073/pnas.1119313109.

[18] S. Tlili, M. Durande, C. Gay, B. Ladoux, F. Graner, and H. Delanoë-Ayari. Migrating epithelial monolayer flows like a maxwell viscoelastic liquid. *Physical Review Letters*, 125(8):088102, aug 2020. doi:10.1103/physrevlett.125.088102.

[19] M. Théry, V. Racine, M. Piel, A. Pepin, A. Dimitrov, Y. Chen, J.-B. Sibarita, and M. Bornens. Anisotropy of cell adhesive microenvironment governs cell internal organization and orientation of polarity. *Proceedings of the National Academy of Sciences*, 103(52):19771–19776, dec 2006. doi:10.1073/pnas.0609267103.

[20] Fabrice Senger, Amandine Pitaval, Hajer Ennomani, Laetitia Kurzawa, Laurent Blanchoin, and Manuel Théry. Spatial integration of mechanical forces by α-actinin establishes actin network symmetry. *Journal of Cell Science*, jan 2019. doi:10.1242/jcs.236604.

[21] Paolo Maiuri, Jean-François Rupprecht, Stefan Wieser, Verena Ruprecht, Olivier Bénichou, Nicolas Carpi, Mathieu Coppey, Simon De Beco, Nir Gov, Carl-Philipp

Heisenberg, Carolina Lage Crespo, Franziska Lautenschlaeger, Maël Le Berre, Ana-Maria Lennon-Dumenil, Matthew Raab, Hawa-Racine Thiam, Matthieu Piel, Michael Sixt, and Raphaël Voituriez. Actin flows mediate a universal coupling between cell speed and cell persistence. *Cell*, 161(2):374–386, apr 2015. doi:10.1016/j.cell.2015.01.056.

[22] A. J. Lomakin, C. J. Cattin, D. Cuvelier, Z. Alraies, M. Molina, G. P. F. Nader, N. Srivastava, P. J. Sáez, J. M. Garcia-Arcos, I. Y. Zhitnyak, A. Bhargava, M. K. Driscoll, E. S. Welf, R. Fiolka, R. J. Petrie, N. S. De Silva, J. M. González-Granado, N. Manel, A. M. Lennon-Duménil, D. J. Müller, and M. Piel. The nucleus acts as a ruler tailoring cell responses to spatial constraints. *Science*, 370(6514):eaba2894, oct 2020. doi:10.1126/science.aba2894.

[23] X. Jiang, D. A. Bruzewicz, A. P. Wong, M. Piel, and G. M. Whitesides. Directing cell migration with asymmetric micropatterns. *Proceedings of the National Academy of Sciences*, 102(4):975–978, jan 2005. doi:10.1073/pnas.0408954102.

[24] Goher Mahmud, Christopher J. Campbell, Kyle J. M. Bishop, Yulia A. Komarova, Oleg Chaga, Siowling Soh, Sabil Huda, Kristiana Kandere-Grzybowska, and Bartosz A. Grzybowski. Directing cell motions on micropatterned ratchets. *Nature Physics*, 5(8):606–612, jun 2009. doi:10.1038/nphys1306.

[25] David Caballero, Raphaël Voituriez, and Daniel Riveline. Protrusion fluctuations direct cell motion. *Biophysical Journal*, 107(1):34–42, jul 2014. doi:10.1016/j.bpj.2014.05.002.

[26] David B. Brückner, Alexandra Fink, Christoph Schreiber, Peter J. F. Röttgermann, Joachim O. Rädler, and Chase P. Broedersz. Stochastic nonlinear dynamics of confined cell migration in two-state systems. *Nature Physics*, 15(6):595–601, mar 2019. doi:10.1038/s41567-019-0445-4.

[27] Mcolisi Dlamini, Timothy E. Kennedy, and David Juncker. Combinatorial nanodot stripe assay to systematically study cell haptotaxis. *Microsystems & Nanoengineering*, 6(1), dec 2020. doi:10.1038/s41378-020-00223-0.

[28] Philipp J. Albert and Ulrich S. Schwarz. Modeling cell shape and dynamics on micropatterns. *Cell Adhesion & Migration*, 10(5):516–528, mar 2016. doi:10.1080/19336918.2016.1148864.

[29] Daniel M. Sussman, M. Paoluzzi, M. Cristina Marchetti, and M. Lisa Manning. Anomalous glassy dynamics in simple models of dense biological tissue. *EPL (Europhysics Letters)*, 121(3):36001, feb 2018. doi:10.1209/0295-5075/121/36001.

[30] Elizabeth Lawson-Keister and M. Lisa Manning. Jamming and arrest of cell motion in biological tissues, 2021. arXiv:2102.11255.

[31] Athanasius F. M. Marée, Alexandra Jilkine, Adriana Dawes, Verônica A. Grieneisen, and Leah Edelstein-Keshet. Polarization and movement of keratocytes: A multiscale modelling approach. *Bulletin of Mathematical Biology*, 68(5):1169–1211, jun 2006. doi:10.1007/s11538-006-9131-7.

[32] Philipp J. Albert and Ulrich S. Schwarz. Dynamics of cell ensembles on adhesive micropatterns: Bridging the gap between single cell spreading and collective cell migration. *PLOS Computational Biology*, 12(4):e1004863, apr 2016. doi:10.1371/journal.pcbi.1004863.

[33] Florian Thüroff, Andriy Goychuk, Matthias Reiter, and Erwin Frey. Bridging the gap between single-cell migration and collective dynamics. *eLife*, 8, dec 2019. doi:10.7554/elife.46842.

[34] David B. Brückner, Nicolas Arlt, Alexandra Fink, Pierre Ronceray, Joachim O. Rädler, and Chase P. Broedersz. Learning the dynamics of cell-cell interactions in confined cell migration. *Proceedings of the National Academy of Sciences*, 118(7):e2016602118, feb 2021. doi:10.1073/pnas.2016602118.

[35] Douglas A Lauffenburger and Alan F Horwitz. Cell migration: A physically integrated molecular process. *Cell*, 84(3):359–369, feb 1996. doi:10.1016/s0092-8674(00)81280-5.

[36] Paolo Maiuri, Emmanuel Terriac, Perrine Paul-Gilloteaux, Timothée Vignaud, Krista McNally, James Onuffer, Kurt Thorn, Phuong A. Nguyen, Nefeli Georgoulia, Daniel Soong, Asier Jayo, Nina Beil, Jürgen Beneke, Joleen Chooi Hong Lim, Chloe Pei-Ying Sim, Yeh-Shiu Chu, Andrea Jiménez-Dalmaroni, Jean-François Joanny, Jean-Paul Thiery, Holger Erfle, Maddy Parsons, Timothy J. Mitchison, Wendell A. Lim, Ana-Maria Lennon-Duménil, Matthieu Piel, and Manuel Théry. The first world cell race. *Current Biology*, 22(17):R673–R675, sep 2012. doi:10.1016/j.cub.2012.07.052.

[37] Shiladitya Banerjee, Margaret L. Gardel, and Ulrich S. Schwarz. The actin cytoskeleton as an active adaptive material. *Annual Review of Condensed Matter Physics*, 11(1):421–439, mar 2020. doi:10.1146/annurev-conmatphys-031218-013231.

[38] Thomas D. Pollard and John A. Cooper. Actin, a central player in cell shape and movement. *Science*, 326(5957):1208–1212, nov 2009. doi:10.1126/science.1175862.

[39] Benjamin Geiger, Alexander Bershadsky, Roumen Pankov, and Kenneth M. Yamada. Transmembrane crosstalk between the extracellular matrix and the cytoskeleton. *Nature Reviews Molecular Cell Biology*, 2(11):793–805, nov 2001. doi:10.1038/35099066.

[40] Patricia M. Davidson and Bruno Cadot. Actin on and around the nucleus. *Trends in Cell Biology*, dec 2020. doi:10.1016/j.tcb.2020.11.009.

[41] Jan Mueller, Gregory Szep, Maria Nemethova, Ingrid de Vries, Arnon D. Lieber, Christoph Winkler, Karsten Kruse, J. Victor Small, Christian Schmeiser, Kinneret Keren, Robert Hauschild, and Michael Sixt. Load adaptation of lamellipodial actin networks. *Cell*, 171(1):188–200.e16, sep 2017. doi:10.1016/j.cell.2017.07.051.

[42] Matthew D. Welch and R. Dyche Mullins. Cellular control of actin nucleation. *Annual Review of Cell and Developmental Biology*, 18(1):247–288, nov 2002. doi:10.1146/annurev.cellbio.18.040202.112133.

[43] Kate M. Byrne, Naser Monsefi, John C. Dawson, Andrea Degasperi, Jimi-Carlo Bukowski-Wills, Natalia Volinsky, Maciej Dobrzyński, Marc R. Birtwistle, Mikhail A. Tsyganov, Anatoly Kiyatkin, Katarzyna Kida, Andrew J. Finch, Neil O. Carragher, Walter Kolch, Lan K. Nguyen, Alex von Kriegsheim, and Boris N. Kholodenko. Bistability in the rac1, PAK, and RhoA signaling network drives actin cytoskeleton dynamics and cell motility switches. *Cell Systems*, 2(1):38–48, jan 2016. doi:10.1016/j.cels.2016.01.003.

[44] Keith Burridge and Krister Wennerberg. Rho and rac take center stage. *Cell*, 116(2):167–179, jan 2004. doi:10.1016/s0092-8674(04)00003-0.

[45] L. Petitjean, M. Reffay, E. Grasland-Mongrain, M. Poujade, B. Ladoux, A. Buguin, and P. Silberzan. Velocity fields in a collectively migrating epithelium. *Biophysical Journal*, 98(9):1790–1800, may 2010. doi:10.1016/j.bpj.2010.01.030.

[46] Benoit Rogez, Laeschkir Würthner, Anastasiia B. Petrova, Felix B. Zierhut, Dario Saczko-Brack, Maria-Ana Huergo, Christopher Batters, Erwin Frey, and Claudia Veigel. Reconstitution reveals how myosin-VI self-organises to generate a dynamic mechanism of membrane sculpting. *Nature Communications*, 10(1), jul 2019. doi:10.1038/s41467-019-11268-9.

[47] Henry Harris. Chemotaxis. *Experimental Cell Research*, 8:199–208, jan 1961. doi:10.1016/0014-4827(61)90349-4.

[48] David Ellison, Andrew Mugler, Matthew D. Brennan, Sung Hoon Lee, Robert J. Huebner, Eliah R. Shamir, Laura A. Woo, Joseph Kim, Patrick Amar, Ilya Nemenman, Andrew J. Ewald, and Andre Levchenko. Cell–cell communication enhances the capacity of cell ensembles to sense shallow gradients during morphogenesis. *Proceedings of the National Academy of Sciences*, 113(6):E679–E688, jan 2016. doi:10.1073/pnas.1516503113.

[49] ChunMin Lo, HongBei Wang, Micah Dembo, and Yu li Wang. Cell movement is guided by the rigidity of the substrate. *Biophysical Journal*, 79(1):144–152, jul 2000. doi:10.1016/s0006-3495(00)76279-5.

[50] S. B. Carter. Principles of cell motility: The direction of cell movement and cancer invasion. *Nature*, 208(5016):1183–1187, dec 1965. doi:10.1038/2081183a0.

[51] Anne J. Ridley and Alan Hall. The small GTP-binding protein rho regulates the assembly of focal adhesions and actin stress fibers in response to growth factors. *Cell*, 70(3):389–399, aug 1992. doi:10.1016/0092-8674(92)90163-7.

[52] Anne J. Ridley, Hugh F. Paterson, Caroline L. Johnston, Dagmar Diekmann, and Alan Hall. The small GTP-binding protein rac regulates growth factor-induced membrane ruffling. *Cell*, 70(3):401–410, aug 1992. doi:10.1016/0092-8674(92)90164-8.

[53] Johannes L. Bos, Holger Rehmann, and Alfred Wittinghofer. GEFs and GAPs: Critical elements in the control of small g proteins. *Cell*, 129(5):865–877, jun 2007. doi:10.1016/j.cell.2007.05.018.

[54] Richard G. Hodge and Anne J. Ridley. Regulating rho GTPases and their regulators. *Nature Reviews Molecular Cell Biology*, 17(8):496–510, jun 2016. doi:10.1038/nrm.2016.67.

[55] Elisabeth M. Gardiner, Kersi N. Pestonjamasp, Benjamin P. Bohl, Chester Chamberlain, Klaus M. Hahn, and Gary M. Bokoch. Spatial and temporal analysis of rac activation during live neutrophil chemotaxis. *Current Biology*, 12(23):2029–2034, dec 2002. doi:10.1016/s0960-9822(02)01334-9.

[56] David Pruyne and Anthony Bretscher. Polarization of cell growth in yeast. i. establishment and maintenance of polarity states. *Journal of cell science*, 113(3):365–375, 2000.

[57] R Kozma, S Sarner, S Ahmed, and L Lim. Rho family GTPases and neuronal growth cone remodelling: relationship between increased complexity induced by cdc42hs, rac1, and acetylcholine and collapse induced by RhoA and lysophosphatidic acid. *Molecular and Cellular Biology*, 17(3):1201–1211, mar 1997. doi:10.1128/mcb.17.3.1201.

[58] Sandrine Etienne-Manneville and Alan Hall. Integrin-mediated activation of cdc42 controls cell polarity in migrating astrocytes through PKCζ. *Cell*, 106(4):489–498, aug 2001. doi:10.1016/s0092-8674(01)00471-8.

[59] Alexander F. Palazzo, Tiffani A. Cook, Arthur S. Alberts, and Gregg G. Gundersen. mDia mediates rho-regulated formation and orientation of stable microtubules. *Nature Cell Biology*, 3(8):723–729, jul 2001. doi:10.1038/35087035.

[60] Matthias Machacek, Louis Hodgson, Christopher Welch, Hunter Elliott, Olivier Pertz, Perihan Nalbant, Amy Abell, Gary L. Johnson, Klaus M. Hahn, and Gaudenz Danuser. Coordination of rho GTPase activities during cell protrusion. *Nature*, 461(7260):99–103, aug 2009. doi:10.1038/nature08242.

[61] Sandrine Etienne-Manneville and Alan Hall. Rho GTPases in cell biology. *Nature*, 420(6916):629–635, dec 2002. doi:10.1038/nature01148.

[62] O. Pertz. Spatio-temporal rho GTPase signaling - where are we now? *Journal of Cell Science*, 123(11):1841–1850, may 2010. doi:10.1242/jcs.064345.

[63] Christophe Guilluy, Rafael Garcia-Mata, and Keith Burridge. Rho protein crosstalk: another social network? *Trends in Cell Biology*, 21(12):718–726, dec 2011. doi:10.1016/j.tcb.2011.08.002.

[64] Jon S. Zawistowski, Mohsen Sabouri-Ghomi, Gaudenz Danuser, Klaus M. Hahn, and Louis Hodgson. A RhoC biosensor reveals differences in the activation kinetics of RhoA and RhoC in migrating cells. *PLoS ONE*, 8(11):e79877, nov 2013. doi:10.1371/journal.pone.0079877.

[65] Anne J Ridley. Rho GTPase signalling in cell migration. *Current Opinion in Cell Biology*, 36:103–112, oct 2015. doi:10.1016/j.ceb.2015.08.005.

[66] Marie Evangelista, Sally Zigmond, and Charles Boone. Formins: signaling effectors for assembly and polarization of actin filaments. *Journal of Cell Science*, 116(13):2603–2611, jul 2003. doi:10.1242/jcs.00611.

[67] Yangmi Lim, Ssang-Taek Lim, Alok Tomar, Margaret Gardel, Joie A. Bernard-Trifilo, Xiao Lei Chen, Sean A. Uryu, Rafaela Canete-Soler, Jinbin Zhai, Hong Lin, William W. Schlaepfer, Perihan Nalbant, Gary Bokoch, Dusko Ilic, Clare Waterman-Storer, and David D. Schlaepfer. PyK2 and FAK connections to p190rho guanine nucleotide exchange factor regulate RhoA activity, focal adhesion formation, and cell motility. *Journal of Cell Biology*, 180(1):187–203, jan 2008. doi:10.1083/jcb.200708194.

[68] Shujie Wang, Takashi Watanabe, Kenji Matsuzawa, Akira Katsumi, Mai Kakeno, Toshinori Matsui, Feng Ye, Kazuhide Sato, Kiyoko Murase, Ikuko Sugiyama,

Kazushi Kimura, Akira Mizoguchi, Mark H. Ginsberg, John G. Collard, and Kozo Kaibuchi. Tiam1 interaction with the PAR complex promotes talin-mediated rac1 activation during polarized cell migration. *Journal of Cell Biology*, 199(2):331–345, oct 2012. doi:10.1083/jcb.201202041.

[69] Chetan K Rane and Audrey Minden. P21 activated kinases. *Small GTPases*, 5(1):e28003, jan 2014. doi:10.4161/sgtp.28003.

[70] Matthias Krause and Alexis Gautreau. Steering cell migration: lamellipodium dynamics and the regulation of directional persistence. *Nature Reviews Molecular Cell Biology*, 15(9):577–590, aug 2014. doi:10.1038/nrm3861.

[71] Sonja Kühn and Matthias Geyer. Formins as effector proteins of rho GTPases. *Small GTPases*, 5(3):e983876, jul 2014. doi:10.4161/sgtp.29513.

[72] X. Cao, C. Voss, B. Zhao, T. Kaneko, and S. S.-C. Li. Differential regulation of the activity of deleted in liver cancer 1 (DLC1) by tensins controls cell migration and transformation. *Proceedings of the National Academy of Sciences*, 109(5):1455–1460, jan 2012. doi:10.1073/pnas.1114368109.

[73] Xuan Cao, Tomonori Kaneko, Jenny S. Li, An-Dong Liu, Courtney Voss, and Shawn S. C. Li. A phosphorylation switch controls the spatiotemporal activation of rho GTPases in directional cell migration. *Nature Communications*, 6(1), jul 2015. doi:10.1038/ncomms8721.

[74] K. Kimura, M. Ito, M. Amano, K. Chihara, Y. Fukata, M. Nakafuku, B. Yamamori, J. Feng, T. Nakano, K. Okawa, A. Iwamatsu, and K. Kaibuchi. Regulation of myosin phosphatase by rho and rho-associated kinase (rho-kinase). *Science*, 273(5272):245–248, jul 1996. doi:10.1126/science.273.5272.245.

[75] Francisco M. Vega, Gilbert Fruhwirth, Tony Ng, and Anne J. Ridley. RhoA and RhoC have distinct roles in migration and invasion by acting through different targets. *Journal of Cell Biology*, 193(4):655–665, may 2011. doi:10.1083/jcb.201011038.

[76] Tony Hodge, M. Jamie, and T. V. Cope. A myosin family tree. *Journal of cell science*, 113(19):3353–3354, 2000.

[77] Amber L. Wells, Abel W. Lin, Li-Qiong Chen, Daniel Safer, Shane M Cain, Tama Hasson, Bridget O Carragher, Ronald A Milligan, and H Lee Sweeney. Myosin vi is an actin-based motor that moves backwards. *Nature*, 401(6752):505–508, 1999. doi:https://doi-org.emedien.ub.uni-muenchen.de/10.1038/46835.

[78] James R Sellers. Myosins: a diverse superfamily. *Biochimica et Biophysica Acta (BBA) - Molecular Cell Research*, 1496(1):3–22, mar 2000. doi:10.1016/s0167-4889(00)00005-7.

[79] Enrique M. De la Cruz, E. Michael Ostap, and H. Lee Sweeney. Kinetic mechanism and regulation of myosin vi. *Journal of Biological Chemistry*, 276(34):32373–32381, 2001. doi:https://doi.org/10.1074/jbc.M104136200.

[80] Folma Buss, Susan D Arden, Margaret Lindsay, J Paul Luzio, and John Kendrick-Jones. Myosin VI isoform localized to clathrin-coated vesicles with a role in clathrin-mediated endocytosis. *The EMBO Journal*, 20(14):3676–3684, jul 2001. doi:10.1093/emboj/20.14.3676.

[81] Folma Buss, John Kendrick-Jones, Corinne Lionne, Alex E. Knight, Graham P. Côté, and J. Paul Luzio. The localization of myosin VI at the golgi complex and leading edge of fibroblasts and its phosphorylation and recruitment into membrane ruffles of a431 cells after growth factor stimulation. *Journal of Cell Biology*, 143(6):1535–1545, dec 1998. doi:10.1083/jcb.143.6.1535.

[82] Elisa Magistrati and Simona Polo. Myomics: myosin VI structural and functional plasticity. *Current Opinion in Structural Biology*, 67:33–40, apr 2021. doi:10.1016/j.sbi.2020.09.005.

[83] Laura Aschenbrenner, TinThu Lee, and Tama Hasson. Myo6 facilitates the translocation of endocytic vesicles from cell peripheries. *Molecular Biology of the Cell*, 14(7):2728–2743, jul 2003. doi:10.1091/mbc.e02-11-0767.

[84] Rhys Roberts, Ida Lister, Stephan Schmitz, Matthew Walker, Claudia Veigel, John Trinick, Folma Buss, and John Kendrick-Jones. Myosin vi: cellular functions and motor properties. *Philosophical Transactions of the Royal Society of London. Series B: Biological Sciences*, 359(1452):1931–1944, dec 2004. doi:10.1098/rstb.2004.1563.

[85] Karen B. Avraham, Tama Hasson, Karen P. Steel, David M. Kingsley, Liane B. Russell, Mark S. Mooseker, Neal G. Copeland, and Nancy A. Jenkins. The mouse snell's waltzer deafness gene encodes an unconventional myosin required for structural integrity of inner ear hair cells. *Nature Genetics*, 11(4):369–375, dec 1995. doi:10.1038/ng1295-369.

[86] Claire L Warner, Abigail Stewart, J Paul Luzio, Karen P Steel, Richard T Libby, John Kendrick-Jones, and Folma Buss. Loss of myosin VI reduces secretion and the size of the golgi in fibroblasts from snell's waltzer mice. *The EMBO Journal*, 22(3):569–579, feb 2003. doi:10.1093/emboj/cdg055.

[87] I. Lister, R. Roberts, S. Schmitz, M. Walker, J. Trinick, C. Veigel, F. Buss, and J. Kendrick-Jones. Myosin VI: a multifunctional motor. *Biochemical Society Transactions*, 32(5):685–688, oct 2004. doi:10.1042/bst0320685.

[88] Erika R. Geisbrecht and Denise J. Montell. Myosin vi is required for e-cadherin-mediated border cell migration. *Nature Cell Biology*, 4(8):616–620, jul 2002. doi:10.1038/ncb830.

[89] Mijo Simunovic, Gregory A. Voth, Andrew Callan-Jones, and Patricia Bassereau. When physics takes over: BAR proteins and membrane curvature. *Trends in Cell Biology*, 25(12):780–792, dec 2015. doi:10.1016/j.tcb.2015.09.005.

[90] R. Sunyer, V. Conte, J. Escribano, A. Elosegui-Artola, A. Labernadie, L. Valon, D. Navajas, J. M. Garcia-Aznar, J. J. Munoz, P. Roca-Cusachs, and X. Trepat. Collective cell durotaxis emerges from long-range intercellular force transmission. *Science*, 353(6304):1157–1161, sep 2016. doi:10.1126/science.aaf7119.

[91] Xavier Trepat and Erik Sahai. Mesoscale physical principles of collective cell organization. *Nature Physics*, 14(7):671–682, jul 2018. doi:10.1038/s41567-018-0194-9.

[92] Benoit Ladoux and René-Marc Mège. Mechanobiology of collective cell behaviours. *Nature Reviews Molecular Cell Biology*, 18(12):743–757, nov 2017. doi:10.1038/nrm.2017.98.

[93] Peter Friedl and Roberto Mayor. Tuning collective cell migration by cell–cell junction regulation. *Cold Spring Harbor Perspectives in Biology*, 9(4):a029199, jan 2017. doi:10.1101/cshperspect.a029199.

[94] Roberto Mayor and Sandrine Etienne-Manneville. The front and rear of collective cell migration. *Nature Reviews Molecular Cell Biology*, 17(2):97–109, jan 2016. doi:10.1038/nrm.2015.14.

[95] Mirjam M Zegers and Peter Friedl. Rho GTPases in collective cell migration. *Small GTPases*, 5(3):e983869, jul 2014. doi:10.4161/sgtp.28997.

[96] Peter Friedl and Darren Gilmour. Collective cell migration in morphogenesis, regeneration and cancer. *Nature reviews Molecular cell biology*, 10(7):445–457, 2009. doi:10.1038/nrm2720.

[97] Elsa Bazellières, Vito Conte, Alberto Elosegui-Artola, Xavier Serra-Picamal, María Bintanel-Morcillo, Pere Roca-Cusachs, José J. Muñoz, Marta Sales-Pardo, Roger Guimerà, and Xavier Trepat. Control of cell–cell forces and collective cell dynamics by the intercellular adhesome. *Nature Cell Biology*, 17(4):409–420, mar 2015. doi:10.1038/ncb3135.

[98] Xavier Trepat, Michael R. Wasserman, Thomas E. Angelini, Emil Millet, David A. Weitz, James P. Butler, and Jeffrey J. Fredberg. Physical forces during collective cell migration. *Nature Physics*, 5(6):426–430, may 2009. doi:10.1038/nphys1269.

[99] Xiaobo Wang, Li He, Yi I. Wu, Klaus M. Hahn, and Denise J. Montell. Light-mediated activation reveals a key role for rac in collective guidance of cell movement in vivo. *Nature Cell Biology*, 12(6):591–597, may 2010. doi:10.1038/ncb2061.

[100] René Marc Mège and Noboru Ishiyama. Integration of cadherin adhesion and cytoskeleton at adherens junctions. *Cold Spring Harbor Perspectives in Biology*, 9(5):a028738, jan 2017. doi:10.1101/cshperspect.a028738.

[101] L. Shapiro and W. I. Weis. Structure and biochemistry of cadherins and catenins. *Cold Spring Harbor Perspectives in Biology*, 1(3):a003053–a003053, aug 2009. doi:10.1101/cshperspect.a003053.

[102] Antonis Kourtidis, Ruifeng Lu, Lindy J. Pence, and Panos Z. Anastasiadis. A central role for cadherin signaling in cancer. *Experimental Cell Research*, 358(1):78–85, sep 2017. doi:10.1016/j.yexcr.2017.04.006.

[103] Marta Canel, Alan Serrels, Derek Miller, Paul Timpson, Bryan Serrels, Margaret C. Frame, and Valerie G. Brunton. Quantitative in vivo imaging of the effects of inhibiting integrin signaling via src and FAK on cancer cell movement: Effects on e-cadherin dynamics. *Cancer Research*, 70(22):9413–9422, nov 2010. doi:10.1158/0008-5472.can-10-1454.

[104] Rizwan Farooqui and Gabriel Fenteany. Multiple rows of cells behind an epithelial wound edge extend cryptic lamellipodia to collectively drive cell-sheet movement. *Journal of Cell Science*, 118(1):51–63, dec 2004. doi:10.1242/jcs.01577.

[105] E. Anon, X. Serra-Picamal, P. Hersen, N. C. Gauthier, M. P. Sheetz, X. Trepat, and B. Ladoux. Cell crawling mediates collective cell migration to close undamaged epithelial gaps. *Proceedings of the National Academy of Sciences*, 109(27):10891–10896, jun 2012. doi:10.1073/pnas.1117814109.

[106] Naël Osmani, Nicolas Vitale, Jean-Paul Borg, and Sandrine Etienne-Manneville. Scrib controls cdc42 localization and activity to promote cell polarization during astrocyte migration. *Current Biology*, 16(24):2395–2405, dec 2006. doi:10.1016/j.cub.2006.10.026.

[107] S. Etienne-Manneville. Cdc42 - the centre of polarity. *Journal of Cell Science*, 117(8):1291–1300, mar 2004. doi:10.1242/jcs.01115.

[108] Ricard Alert and Xavier Trepat. Physical models of collective cell migration. *Annual Review of Condensed Matter Physics*, 11(1):77–101, mar 2020. doi:10.1146/annurev-conmatphys-031218-013516.

[109] Gaudenz Danuser, Jun Allard, and Alex Mogilner. Mathematical modeling of eukaryotic cell migration: Insights beyond experiments. *Annual Review of Cell and Developmental Biology*, 29(1):501–528, oct 2013. doi:10.1146/annurev-cellbio-101512-122308.

[110] Ulrich S. Schwarz and Samuel A. Safran. Physics of adherent cells. *Reviews of Modern Physics*, 85(3):1327–1381, aug 2013. doi:10.1103/revmodphys.85.1327.

[111] Matthew L. Blow, Sumesh P. Thampi, and Julia M. Yeomans. Biphasic, lyotropic, active nematics. *Physical Review Letters*, 113(24):248303, dec 2014. doi:10.1103/physrevlett.113.248303.

[112] David Oriola, Ricard Alert, and Jaume Casademunt. Fluidization and active thinning by molecular kinetics in active gels. *Physical Review Letters*, 118(8):088002, feb 2017. doi:10.1103/physrevlett.118.088002.

[113] John Toner and Yuhai Tu. Long-range order in a two-dimensional DynamicalXY-Model: How birds fly together. *Physical Review Letters*, 75(23):4326–4329, dec 1995. doi:10.1103/physrevlett.75.4326.

[114] Tamás Vicsek, András Czirók, Eshel Ben-Jacob, Inon Cohen, and Ofer Shochet. Novel type of phase transition in a system of self-driven particles. *Physical Review Letters*, 75(6):1226–1229, aug 1995. doi:10.1103/physrevlett.75.1226.

[115] M. C. Marchetti, J. F. Joanny, S. Ramaswamy, T. B. Liverpool, J. Prost, Madan Rao, and R. Aditi Simha. Hydrodynamics of soft active matter. *Reviews of Modern Physics*, 85(3):1143–1189, jul 2013. doi:10.1103/revmodphys.85.1143.

[116] Thuan Beng Saw, Amin Doostmohammadi, Vincent Nier, Leyla Kocgozlu, Sumesh Thampi, Yusuke Toyama, Philippe Marcq, Chwee Teck Lim, Julia M. Yeomans, and Benoit Ladoux. Topological defects in epithelia govern cell death and extrusion. *Nature*, 544(7649):212–216, apr 2017. doi:10.1038/nature21718.

[117] Matthias Lawrence Zorn. *Towards cellular hydrodynamics: Collective migration in artificial microstructures*. PhD thesis, Ludwig-Maximilians-Universität München, 2018.

[118] Felix Kempf, Romain Mueller, Erwin Frey, Julia M. Yeomans, and Amin Doostmohammadi. Active matter invasion. *Soft Matter*, 15(38):7538–7546, 2019. doi:10.1039/c9sm01210a.

[119] Makiko Nonomura. Study on multicellular systems using a phase field model. *PLoS ONE*, 7(4):e33501, apr 2012. doi:10.1371/journal.pone.0033501.

[120] Juliane Zimmermann, Brian A. Camley, Wouter-Jan Rappel, and Herbert Levine. Contact inhibition of locomotion determines cell–cell and cell–substrate forces in tissues. *Proceedings of the National Academy of Sciences*, 113(10):2660–2665, feb 2016. doi:10.1073/pnas.1522330113.

[121] Robert Chojowski, Ulrich S. Schwarz, and Falko Ziebert. Reversible elastic phase field approach and application to cell monolayers. *The European Physical Journal E*, 43(10), oct 2020. doi:10.1140/epje/i2020-11988-1.

[122] B A Camley and W-J Rappel. Physical models of collective cell motility: from cell to tissue. *Journal of Physics D: Applied Physics*, 50(11):113002, feb 2017. doi:10.1088/1361-6463/aa56fe.

[123] Néstor Sepúlveda, Laurence Petitjean, Olivier Cochet, Erwan Grasland-Mongrain, Pascal Silberzan, and Vincent Hakim. Collective cell motion in an epithelial sheet can be quantitatively described by a stochastic interacting particle model. *PLoS Computational Biology*, 9(3):e1002944, mar 2013. doi:10.1371/journal.pcbi.1002944.

[124] A. M. Menzel and T. Ohta. Soft deformable self-propelled particles. *EPL (Europhysics Letters)*, 99(5):58001, sep 2012. doi:10.1209/0295-5075/99/58001.

[125] Dapeng Bi, Xingbo Yang, M. Cristina Marchetti, and M. Lisa Manning. Motility-driven glass and jamming transitions in biological tissues. *Physical Review X*, 6(2):021011, apr 2016. doi:10.1103/physrevx.6.021011.

[126] David B. Brückner, Pierre Ronceray, and Chase P. Broedersz. Inferring the dynamics of underdamped stochastic systems. *Physical Review Letters*, 125(5):058103, jul 2020. doi:10.1103/physrevlett.125.058103.

[127] M. S. Steinberg. ON THE MECHANISM OF TISSUE RECONSTRUCTION BY DISSOCIATED CELLS, i. POPULATION KINETICS, DIFFERENTIAL ADHESIVENESS, AND THE ABSENCE OF DIRECTED MIGRATIONOn the mechanism of tissue reconstruction. *Proceedings of the National Academy of Sciences*, 48(9):1577–1582, sep 1962. doi:10.1073/pnas.48.9.1577.

[128] François Graner and James A. Glazier. Simulation of biological cell sorting using a two-dimensional extended potts model. *Physical Review Letters*, 69(13):2013–2016, sep 1992. doi:10.1103/physrevlett.69.2013.

[129] James A. Glazier and François Graner. Simulation of the differential adhesion driven rearrangement of biological cells. *Physical Review E*, 47(3):2128–2154, mar 1993. doi:10.1103/physreve.47.2128.

[130] A Szabó, R Ünnep, E Méhes, W O Twal, W S Argraves, Y Cao, and A Czirók. Collective cell motion in endothelial monolayers. *Physical Biology*, 7(4):046007, nov 2010. doi:10.1088/1478-3975/7/4/046007.

[131] Alexandre J. Kabla. Collective cell migration: leadership, invasion and segregation. *Journal of The Royal Society Interface*, 9(77):3268–3278, jul 2012. doi:10.1098/rsif.2012.0448.

[132] M. Chiang and D. Marenduzzo. Glass transitions in the cellular potts model. *EPL (Europhysics Letters)*, 116(2):28009, oct 2016. doi:10.1209/0295-5075/116/28009.

[133] Felix J. Segerer, Florian Thüroff, Alicia Piera Alberola, Erwin Frey, and Joachim O. Rädler. Emergence and persistence of collective cell migration on small circular micropatterns. *Physical Review Letters*, 114(22):228102, jun 2015. doi:10.1103/physrevlett.114.228102.

[134] Philipp J. Albert and Ulrich S. Schwarz. Dynamics of cell shape and forces on micropatterned substrates predicted by a cellular potts model. *Biophysical Journal*, 106(11):2340–2352, jun 2014. doi:10.1016/j.bpj.2014.04.036.

[135] Andriy Goychuk, David B. Brückner, Andrew W. Holle, Joachim P. Spatz, Chase P. Broedersz, and Erwin Frey. Morphology and motility of cells on soft substrates. 2018. URL: https://arxiv.org/abs/1808.00314, arXiv:1808.00314.

[136] Fang Zhou, Sophia A. Schaffer, Christoph Schreiber, Felix J. Segerer, Andriy Goychuk, Erwin Frey, and Joachim O. Rädler. Quasi-periodic migration of single cells on short microlanes. *PLOS ONE*, 15(4):e0230679, apr 2020. doi:10.1371/journal.pone.0230679.

[137] Felix Maria Kempf. *Invasion of soft active matter into capillaries*. PhD thesis, Ludwig-Maximilians-Universität München, 2021.

[138] Andrew Gelman, John B. Carlin, Hal S. Stern, Donald B. Rubin, and David B. Dunson. *Bayesian Data Analysis*. Taylor & Francis Ltd., 2013.

[139] Athanasius F. M. Marée, Verônica A. Grieneisen, and Leah Edelstein-Keshet. How cells integrate complex stimuli: The effect of feedback from phosphoinositides and cell shape on cell polarization and motility. *PLoS Computational Biology*, 8(3):e1002402, mar 2012. doi:10.1371/journal.pcbi.1002402.

[140] Raj Kumar Sadhu, Samo Penič, Aleš Iglič, and Nir S. Gov. Modelling cellular spreading and emergence of motility in the presence of curved membrane proteins and active cytoskeleton forces. 2021. URL: https://arxiv.org/abs/2101.00313, arXiv:2101.00313.

[141] Alfonso Bolado-Carrancio, Oleksii S Rukhlenko, Elena Nikonova, Mikhail A Tsyganov, Anne Wheeler, Amaya Garcia-Munoz, Walter Kolch, Alex von Kriegsheim, and Boris N Kholodenko. Periodic propagating waves coordinate RhoGTPase network dynamics at the leading and trailing edges during cell migration. *eLife*, 9, jul 2020. doi:10.7554/elife.58165.

[142] Jonathan E. Ron, Pascale Monzo, Nils C. Gauthier, Raphael Voituriez, and Nir S. Gov. One-dimensional cell motility patterns. *Physical Review Research*, 2(3):033237, aug 2020. doi:10.1103/physrevresearch.2.033237.

[143] Christoph Schreiber, Behnam Amiri, Johannes C. J. Heyn, Joachim O. Rädler, and Martin Falcke. On the adhesion–velocity relation and length adaptation of motile cells on stepped fibronectin lanes. *Proceedings of the National Academy of Sciences*, 118(4):e2009959118, jan 2021. doi:10.1073/pnas.2009959118.

[144] Joseph d'Alessandro, Alex Barbier-Chebbah, Victor Cellerin, Olivier Bénichou, René-Marc Mège, Raphaël Voituriez, and Benoît Ladoux. Cell migration driven by long-lived spatial memory. jan 2021. doi:10.1101/2021.01.05.425035.

[145] Pierre Sens. Stick–slip model for actin-driven cell protrusions, cell polarization, and crawling. *Proceedings of the National Academy of Sciences*, 117(40):24670–24678, sep 2020. doi:10.1073/pnas.2011785117.

[146] Milan Mrksich and George M. Whitesides. Patterning self-assembled monolayers using microcontact printing: A new technology for biosensors? *Trends in Biotechnology*, 13(6):228–235, jun 1995. doi:10.1016/s0167-7799(00)88950-7.

[147] Younan Xia and George M. Whitesides. SOFT LITHOGRAPHY. *Annual Review of Materials Science*, 28(1):153–184, aug 1998. doi:10.1146/annurev.matsci.28.1.153.

[148] Tobias Kaufmann and Bart Jan Ravoo. Stamps, inks and substrates: polymers in microcontact printing. *Polymer Chemistry*, 1(4):371–387, 2010. doi:10.1039/b9py00281b.

[149] M. Théry and M. Piel. Adhesive micropatterns for cells: A microcontact printing protocol. *Cold Spring Harbor Protocols*, 2009(7):pdb.prot5255–pdb.prot5255, jul 2009. doi:10.1101/pdb.prot5255.

[150] Felix Jakob Segerer, Peter Johan Friedrich Röttgermann, Simon Schuster, Alicia Piera Alberola, Stefan Zahler, and Joachim Oskar Rädler. Versatile method to generate multiple types of micropatterns. *Biointerphases*, 11(1):011005, mar 2016. doi:10.1116/1.4940703.

[151] Jonathan M. Bélisle, James P. Correia, Paul W. Wiseman, Timothy E. Kennedy, and Santiago Costantino. Patterning protein concentration using laser-assisted adsorption by photobleaching, LAPAP. *Lab on a Chip*, 8(12):2164, 2008. doi:10.1039/b813897d.

[152] Jan Schwarz and Michael Sixt. Quantitative analysis of dendritic cell haptotaxis. pages 567–581, 2016. doi:10.1016/bs.mie.2015.11.004.

[153] H.K. Kleinman, L. Luckenbill-Edds, F.W. Cannon, and G.C. Sephel. Use of extracellular matrix components for cell culture. *Analytical Biochemistry*, 166(1):1–13, oct 1987. doi:10.1016/0003-2697(87)90538-0.

[154] Manuel Théry. Micropatterning as a tool to decipher cell morphogenesis and functions. *Journal of Cell Science*, 123(24):4201–4213, dec 2010. doi:10.1242/jcs.075150.

[155] Fabian Fröhlich, Anita Reiser, Laura Fink, Daniel Woschée, Thomas Ligon, Fabian Joachim Theis, Joachim Oskar Rädler, and Jan Hasenauer. Multi-experiment nonlinear mixed effect modeling of single-cell translation kinetics after transfection. *npj Systems Biology and Applications*, 4(1), dec 2018. doi:10.1038/s41540-018-0079-7.

[156] A. Reiser, D. Woschée, N. Mehrotra, R. Krzysztoń, H. H. Strey, and J. O. Rädler. Correlation of mRNA delivery timing and protein expression in lipid-based transfection. *Integrative Biology*, 11(9):362–371, sep 2019. doi:10.1093/intbio/zyz030.

[157] Herbert B. Schiller, Michaela-Rosemarie Hermann, Julien Polleux, Timothée Vignaud, Sara Zanivan, Caroline C. Friedel, Zhiqi Sun, Aurelia Raducanu, Kay-E. Gottschalk, Manuel Théry, Matthias Mann, and Reinhard Fässler. β_1- and α_v-class integrins cooperate to regulate myosin II during rigidity sensing of fibronectin-based microenvironments. *Nature Cell Biology*, 15(6):625–636, may 2013. doi:10.1038/ncb2747.

[158] Alexandra Murschhauser, Peter J. F. Röttgermann, Daniel Woschée, Martina F. Ober, Yan Yan, Kenneth A. Dawson, and Joachim O. Rädler. A high-throughput microscopy method for single-cell analysis of event-time correlations in nanoparticle-induced cell death. *Communications Biology*, 2(1), jan 2019. doi:10.1038/s42003-019-0282-0.

[159] Jane James, Edgar D. Goluch, Huan Hu, Chang Liu, and Milan Mrksich. Subcellular curvature at the perimeter of micropatterned cells influences lamellipodial distribution and cell polarity. *Cell Motility and the Cytoskeleton*, 65(11):841–852, nov 2008. doi:10.1002/cm.20305.

[160] Elena Kassianidou, Christoph A. Brand, Ulrich S. Schwarz, and Sanjay Kumar. Geometry and network connectivity govern the mechanics of stress fibers. *Proceedings of the National Academy of Sciences*, 114(10):2622–2627, feb 2017. doi:10.1073/pnas.1606649114.

[161] François Pouthas, Philippe Girard, Virginie Lecaudey, Thi Bach Nga Ly, Darren Gilmour, Christian Boulin, Rainer Pepperkok, and Emmanuel G. Reynaud. In migrating cells, the golgi complex and the position of the centrosome depend on geometrical constraints of the substratum. *Journal of Cell Science*, 121(14):2406–2414, jul 2008. doi:10.1242/jcs.026849.

[162] Christoph Schreiber, Felix J. Segerer, Ernst Wagner, Andreas Roidl, and Joachim O. Rädler. Ring-shaped microlanes and chemical barriers as a platform for probing single-cell migration. *Scientific Reports*, 6(1), may 2016. doi:10.1038/srep26858.

[163] Alexandra Fink, David B. Brückner, Christoph Schreiber, Peter J.F. Röttgermann, Chase P. Broedersz, and Joachim O. Rädler. Area and geometry dependence of cell migration in asymmetric two-state micropatterns. *Biophysical Journal*, 118(3):552–564, feb 2020. doi:10.1016/j.bpj.2019.11.3389.

[164] Kevin Doxzen, Sri Ram Krishna Vedula, Man Chun Leong, Hiroaki Hirata, Nir S. Gov, Alexandre J. Kabla, Benoit Ladoux, and Chwee Teck Lim. Guidance of collective cell migration by substrate geometry. *Integrative Biology*, 5(8):1026, 2013. doi:10.1039/c3ib40054a.

[165] Enoch Kim, Younan Xia, and George M. Whitesides. Polymer microstructures formed by moulding in capillaries. *Nature*, 376(6541):581–584, aug 1995. doi:10.1038/376581a0.

[166] Hyun-Woo Shim, Ji-Hye Lee, Taek-Sung Hwang, Young Woo Rhee, Yun Mi Bae, Joon Sig Choi, Jongyoon Han, and Chang-Soo Lee. Patterning of proteins and cells on functionalized surfaces prepared by polyelectrolyte multilayers and micromolding in capillaries. *Biosensors and Bioelectronics*, 22(12):3188–3195, jun 2007. doi:10.1016/j.bios.2007.02.016.

[167] Hwan-Moon Song and Chang-Soo Lee. Simple fabrication of functionalized surface with polyethylene glycol microstructure and glycidyl methacrylate moiety for the selective immobilization of proteins and cells. *Korean Journal of Chemical Engineering*, 25(6):1467–1472, nov 2008. doi:10.1007/s11814-008-0241-9.

[168] Anna-Kristina Marel, Susanne Rappl, Alicia Piera Alberola, and Joachim Oskar Rädler. Arraying cell cultures using PEG-DMA micromolding in standard culture dishes. *Macromolecular Bioscience*, 13(5):595–602, mar 2013. doi:10.1002/mabi.201200400.

[169] Qingzong Tseng, Irene Wang, Eve Duchemin-Pelletier, Ammar Azioune, Nicolas Carpi, Jie Gao, Odile Filhol, Matthieu Piel, Manuel Théry, and Martial Balland. A new micropatterning method of soft substrates reveals that different tumorigenic signals can promote or reduce cell contraction levels. *Lab on a Chip*, 11(13):2231, 2011. doi:10.1039/c0lc00641f.

[170] Timothée Vignaud, Hajer Ennomani, and Manuel Théry. Polyacrylamide hydrogel micropatterning. pages 93–116, 2014. doi:10.1016/b978-0-12-417136-7.00006-9.

[171] Soo-Hong Lee, James J. Moon, and Jennifer L. West. Three-dimensional micropatterning of bioactive hydrogels via two-photon laser scanning photolithography for guided 3d cell migration. *Biomaterials*, 29(20):2962–2968, jul 2008. doi:10.1016/j.biomaterials.2008.04.004.

[172] Joseph C. Hoffmann and Jennifer L. West. Three-dimensional photolithographic micropatterning: a novel tool to probe the complexities of cell migration. *Integrative Biology*, 5(5):817, 2013. doi:10.1039/c3ib20280a.

[173] Miriam Dietrich, Hugo Le Roy, David B. Brückner, Hanna Engelke, Roman Zantl, Joachim O. Rädler, and Chase P. Broedersz. Guiding 3d cell migration in deformed synthetic hydrogel microstructures. *Soft Matter*, 14(15):2816–2826, 2018. doi:10.1039/c8sm00018b.

[174] Franziska Lautenschläger and Matthieu Piel. Microfabricated devices for cell biology: all for one and one for all. *Current Opinion in Cell Biology*, 25(1):116–124, feb 2013. doi:10.1016/j.ceb.2012.10.017.

[175] Naoyuki Nishiya, William B. Kiosses, Jaewon Han, and Mark H. Ginsberg. An α_4 integrin–paxillin–arf-GAP complex restricts rac activation to the leading edge of migrating cells. *Nature Cell Biology*, 7(4):343–352, mar 2005. doi:10.1038/ncb1234.

[176] Geonhui Lee, Seong-Beom Han, and Dong-Hwee Kim. Cell-ECM contact-guided intracellular polarization is mediated via lamin a/c dependent nucleus-cytoskeletal connection. *Biomaterials*, 268:120548, jan 2021. doi:10.1016/j.biomaterials.2020.120548.

[177] Brian A. Camley, Yanxiang Zhao, Bo Li, Herbert Levine, and Wouter-Jan Rappel. Periodic migration in a physical model of cells on micropatterns. *Physical Review Letters*, 111(15):158102, oct 2013. doi:10.1103/physrevlett.111.158102.

[178] Sonja Kühn, Constanze Erdmann, Frieda Kage, Jennifer Block, Lisa Schwenkmezger, Anika Steffen, Klemens Rottner, and Matthias Geyer. The

structure of FMNL2–cdc42 yields insights into the mechanism of lamellipodia and filopodia formation. *Nature Communications*, 6(1), may 2015. doi:10.1038/ncomms8088.

[179] F. N. Fritsch and R. E. Carlson. Monotone piecewise cubic interpolation. *SIAM Journal on Numerical Analysis*, 17(2):238–246, apr 1980. doi:10.1137/0717021.

[180] Torsten Hothorn, Peter Buehlmann, Thomas Kneib, Matthias Schmid, and Benjamin Hofner. *mboost: Model-Based Boosting*, 2020. R package version 2.9-4. URL: https://CRAN.R-project.org/package=mboost.

[181] Relda Cailleau, Matilde Olivé, and Quita V. J. Cruciger. Long-term human breast carcinoma cell lines of metastatic origin: Preliminary characterization. *In Vitro*, 14(11):911–915, nov 1978. doi:10.1007/bf02616120.

[182] Hiroyuki Shima. *Functional Analysis for Physics and Engineering*. Taylor & Francis Ltd., 2016.

[183] Bernd Bischl, Jakob Richter, Jakob Bossek, Daniel Horn, Janek Thomas, and Michel Lang. mlrmbo: A modular framework for model-based optimization of expensive black-box functions, 2018. arXiv:1703.03373.

[184] Hélène D. Moreau, Matthieu Piel, Raphaël Voituriez, and Ana-Maria Lennon-Duménil. Integrating physical and molecular insights on immune cell migration. *Trends in Immunology*, 39(8):632–643, aug 2018. doi:10.1016/j.it.2018.04.007.

[185] Aglaja Kopf, Jörg Renkawitz, Robert Hauschild, Irute Girkontaite, Kerry Tedford, Jack Merrin, Oliver Thorn-Seshold, Dirk Trauner, Hans Häcker, Klaus-Dieter Fischer, Eva Kiermaier, and Michael Sixt. Microtubules control cellular shape and coherence in amoeboid migrating cells. *Journal of Cell Biology*, 219(6), may 2020. doi:10.1083/jcb.201907154.

[186] Theresa-Maja E. Reitz. Stochastic analysis of cell-trajectories on branched micropatterns. Bachelor's Thesis at the Faculty of Physics at Ludwig-Maximilians-Universität, Munich, October 2020.

[187] Jean-Yves Tinevez, Nick Perry, Johannes Schindelin, Genevieve M. Hoopes, Gregory D. Reynolds, Emmanuel Laplantine, Sebastian Y. Bednarek, Spencer L. Shorte, and Kevin W. Eliceiri. TrackMate: An open and extensible platform for single-particle tracking. *Methods*, 115:80–90, feb 2017. doi:10.1016/j.ymeth.2016.09.016.

[188] Francis Galton. *Natural inheritance*. Macmillan and Company, 1889. URL: https://galton.org/books/natural-inheritance/pdf/galton-nat-inh-1up-clean.pdf.

[189] Veena Padmanaban, Ilona Krol, Yasir Suhail, Barbara M. Szczerba, Nicola Aceto, Joel S. Bader, and Andrew J. Ewald. E-cadherin is required for metastasis in multiple models of breast cancer. *Nature*, 573(7774):439–444, sep 2019. doi:10.1038/s41586-019-1526-3.

[190] Elena Scarpa, Alice Roycroft, Eric Theveneau, Emmanuel Terriac, Matthieu Piel, and Roberto Mayor. A novel method to study contact inhibition of locomotion using micropatterned substrates. *Biology Open*, 2(9):901–906, jul 2013. doi:10.1242/bio.20135504.

[191] Daniel F. Milano, Nicholas A. Ngai, Senthil K. Muthuswamy, and Anand R. Asthagiri. Regulators of metastasis modulate the migratory response to cell contact under spatial confinement. *Biophysical Journal*, 110(8):1886–1895, apr 2016. doi:10.1016/j.bpj.2016.02.040.

[192] David B. Brückner, Alexandra Fink, Joachim O. Rädler, and Chase P. Broedersz. Disentangling the behavioural variability of confined cell migration. *Journal of The Royal Society Interface*, 17(163):20190689, feb 2020. doi:10.1098/rsif.2019.0689.

[193] Udo Jeschke, Ioannis Mylonas, Christina Kuhn, Naim Shabani, Christiane Kunert-Keil, Christian Schindlbeck, Bernd Gerber, and Klaus Friese. Expression of e-cadherin in human ductal breast cancer carcinoma in situ, invasive carcinomas, their lymph node metastases, their distant metastases, carcinomas with recurrence and in recurrence. *Anticancer research*, 27(4A):1969–1974, 2007.

[194] Akihiko Fukagawa, Hiroki Ishii, Keiji Miyazawa, and Masao Saitoh. δEF1 associates with DNMT1 and maintains DNA methylation of the e-cadherin promoter in breast cancer cells. *Cancer Medicine*, 4(1):125–135, oct 2014. doi:10.1002/cam4.347.

[195] Nair Lopes, Joana Carvalho, Cecilia Duraes, Barbara Sousa, Madalena Gomes, Jose Luis Costa, Carla Oliveira, Joana Paredes, and Fernando Schmitt. 1alpha, 25-dihydroxyvitamin d3 induces de novo e-cadherin expression in triple-negative breast cancer cells by cdh1-promoter demethylation. *Anticancer research*, 32(1):249–257, 2012.

[196] Augustine Chen, Henry Beetham, Michael A Black, Rashmi Priya, Bryony J Telford, Joanne Guest, George A R Wiggins, Tanis D Godwin, Alpha S Yap, and Parry J Guilford. E-cadherin loss alters cytoskeletal organization and adhesion in non-malignant breast cells but is insufficient to induce an epithelial-mesenchymal transition. *BMC Cancer*, 14(1), jul 2014. doi:10.1186/1471-2407-14-552.

[197] G M Nagaraja, M Othman, B P Fox, R Alsaber, C M Pellegrino, Y Zeng, R Khanna, P Tamburini, A Swaroop, and R P Kandpal. Gene expression signatures and biomarkers of noninvasive and invasive breast cancer cells: comprehensive profiles by representational difference analysis, microarrays and proteomics. *Oncogene*, 25(16):2328–2338, nov 2005. doi:10.1038/sj.onc.1209265.

[198] Michael J Pishvaian, Carolyn M Feltes, Patrick Thompson, Marion J Bussemakers, Jack A Schalken, and Stephen W Byers. Cadherin-11 is expressed in invasive breast cancer cell lines. *Cancer research*, 59(4):947–952, 1999.

[199] Renping Zhou. The eph family receptors and ligands. *Pharmacology & Therapeutics*, 77(3):151–181, mar 1998. doi:10.1016/s0163-7258(97)00112-5.

[200] Ilias Nikas, Han Suk Ryu, and Stamatios Theocharis. Viewing the eph receptors with a focus on breast cancer heterogeneity. *Cancer Letters*, 434:160–171, oct 2018. doi:10.1016/j.canlet.2018.07.030.

[201] K. K. Murai. `eph'ective signaling: forward, reverse and crosstalk. *Journal of Cell Science*, 116(14):2823–2832, jul 2003. doi:10.1242/jcs.00625.

[202] Alice Davy and Philippe Soriano. Ephrin signaling in vivo: Look both ways. *Developmental Dynamics*, 232(1):1–10, 2004. doi:10.1002/dvdy.20200.

[203] Erika Gucciardo, Nami Sugiyama, and Kaisa Lehti. Eph- and ephrin-dependent mechanisms in tumor and stem cell dynamics. *Cellular and Molecular Life Sciences*, 71(19):3685–3710, may 2014. doi:10.1007/s00018-014-1633-0.

[204] Dana M. Brantley-Sieders, Aixiang Jiang, Krishna Sarma, Akosua Badu-Nkansah, Debra L. Walter, Yu Shyr, and Jin Chen. Eph/ephrin profiling in human breast cancer reveals significant associations between expression level and clinical outcome. *PLoS ONE*, 6(9):e24426, sep 2011. doi:10.1371/journal.pone.0024426.

[205] Victoria M. Youngblood, Laura C. Kim, Deanna N. Edwards, Yoonha Hwang, Pranav R. Santapuram, Steven M. Stirdivant, Pengcheng Lu, Fei Ye, Dana M. Brantley-Sieders, and Jin Chen. The ephrin-a1/EPHA2 signaling axis regulates glutamine metabolism in HER2-positive breast cancer. *Cancer Research*, 76(7):1825–1836, feb 2016. doi:10.1158/0008-5472.can-15-0847.

[206] Katsuaki Ieguchi and Yoshiro Maru. Roles of EphA1/a2 and ephrin-a1 in cancer. *Cancer Science*, 110(3):841–848, feb 2019. doi:10.1111/cas.13942.

[207] Theobald Lohmüller, Qian Xu, and Jay T. Groves. Nanoscale obstacle arrays frustrate transport of EphA2–ephrin-a1 clusters in cancer cell lines. *Nano Letters*, 13(7):3059–3064, jun 2013. doi:10.1021/nl400874v.

[208] Yao Zhao, Chenchen Cai, Miaomiao Zhang, Lubing Shi, Jiwei Wang, Haoliang Zhang, Ping Ma, and Shibao Li. Ephrin-a2 promotes prostate cancer metastasis by enhancing angiogenesis and promoting EMT. *Journal of Cancer Research and Clinical Oncology*, mar 2021. doi:10.1007/s00432-021-03618-2.

[209] Zhaohua Richard Huang, Suresh Kumar Tipparaju, Dmitri B. Kirpotin, Christine Pien, Tad Kornaga, Charles O. Noble, Alexander Koshkaryev, Jimmy Tran, Walid S. Kamoun, and Daryl C. Drummond. Formulation optimization of an ephrin a2 targeted immunoliposome encapsulating reversibly modified taxane prodrugs. *Journal of Controlled Release*, 310:47–57, sep 2019. doi:10.1016/j.jconrel.2019.08.006.

[210] Mariana Lucero, Jaspreet Thind, Jaqueline Sandoval, Shayan Senaati, Belinda Jimenez, and Raj P. Kandpal. Stem-like cells from invasive breast carcinoma cell line MDA-MB-231 express a distinct set of eph receptors and ephrin ligands. *Cancer Genomics - Proteomics*, 17(6):729–738, 2020. doi:10.21873/cgp.20227.

[211] Jonathan W. Astin, Jennifer Batson, Shereen Kadir, Jessica Charlet, Raj A. Persad, David Gillatt, Jon D. Oxley, and Catherine D. Nobes. Competition amongst eph receptors regulates contact inhibition of locomotion and invasiveness in prostate cancer cells. *Nature Cell Biology*, 12(12):1194–1204, nov 2010. doi:10.1038/ncb2122.

[212] Mariafrancesca Cascione, Valeria De Matteis, Chiara Cristina Toma, Paolo Pellegrino, Stefano Leporatti, and Rosaria Rinaldi. Morphomechanical and structural changes induced by ROCK inhibitor in breast cancer cells. *Experimental Cell Research*, 360(2):303–309, nov 2017. doi:10.1016/j.yexcr.2017.09.020.

[213] Matthias L. Zorn, Anna-Kristina Marel, Felix J. Segerer, and Joachim O. Rädler. Phenomenological approaches to collective behavior in epithelial cell migration. *Biochimica et Biophysica Acta (BBA) - Molecular Cell Research*, 1853(11):3143–3152, nov 2015. doi:10.1016/j.bbamcr.2015.05.021.

[214] T. E. Angelini, E. Hannezo, X. Trepat, M. Marquez, J. J. Fredberg, and D. A. Weitz. Glass-like dynamics of collective cell migration. *Proceedings of the National Academy of Sciences*, 108(12):4714–4719, feb 2011. doi:10.1073/pnas.1010059108.

[215] Lior Atia, Dapeng Bi, Yasha Sharma, Jennifer A. Mitchel, Bomi Gweon, Stephan A. Koehler, Stephen J. DeCamp, Bo Lan, Jae Hun Kim, Rebecca Hirsch, Adrian F. Pegoraro, Kyu Ha Lee, Jacqueline R. Starr, David A. Weitz, Adam C. Martin, Jin-Ah Park, James P. Butler, and Jeffrey J. Fredberg. Geometric constraints during epithelial jamming. *Nature Physics*, 14(6):613–620, apr 2018. doi:10.1038/s41567-018-0089-9.

[216] Inge M. N. Wortel, Ioana Niculescu, P. Martijn Kolijn, Nir Gov, Rob J. de Boer, and Johannes Textor. Actin-inspired feedback couples speed and persistence in a cellular potts model of cell migration. jun 2018. doi:10.1101/338459.

[217] Cécile M. Bidan, Mario Fratzl, Alexis Coullomb, Philippe Moreau, Alain H. Lombard, Irène Wang, Martial Balland, Thomas Boudou, Nora M. Dempsey, Thibaut Devillers, and Aurélie Dupont. Magneto-active substrates for local mechanical stimulation of living cells. *Scientific Reports*, 8(1), jan 2018. doi:10.1038/s41598-018-19804-1.

[218] G. Bradski. The OpenCV Library. *Dr. Dobb's Journal of Software Tools*, 2000.

[219] John Canny. A computational approach to edge detection. *IEEE Transactions on Pattern Analysis and Machine Intelligence*, PAMI-8(6):679–698, nov 1986. doi:10.1109/tpami.1986.4767851.

[220] R Core Team. *R: A Language and Environment for Statistical Computing*. R Foundation for Statistical Computing, Vienna, Austria, 2020. URL: https://www.R-project.org/.

[221] Johannes Schindelin, Ignacio Arganda-Carreras, Erwin Frise, Verena Kaynig, Mark Longair, Tobias Pietzsch, Stephan Preibisch, Curtis Rueden, Stephan Saalfeld, Benjamin Schmid, Jean-Yves Tinevez, Daniel James White, Volker Hartenstein, Kevin Eliceiri, Pavel Tomancak, and Albert Cardona. Fiji: an open-source platform for biological-image analysis. *Nature Methods*, 9(7):676–682, jun 2012. doi:10.1038/nmeth.2019.

Danksagung

An dieser Stelle ein herzlicher Dank an alle, die mir während meiner Promotion zur Seite standen und mich unterstützt haben. Insbesondere gilt mein Dank:

Prof. Joachim Rädler für die Möglichkeit an diesem Lehrstuhl zu promovieren. Vielen Dank für die Betreuung dieser Arbeit und die Möglichkeit mich in so viele Projekte einzuarbeiten. Ich habe in den Jahren am Lehrstuhl sehr viel gelernt.

Meinen Kollaborationspartnern aus der Theorie: Andriy Goychuk für die Beantwortung von Detailfragen zur CPM Implementierung, Felix Kempf für interessante Diskussionen über kollektive Migration bei Keksen und David Brückner für perfekt geplante und dadurch sehr effiziente Meetings zur Zellbewegung auf Dumbbells.

Den Studenten, die ich betreuen durfte und deren Arbeit ebenfalls in dieser Dissertation steckt: Konstantin Steppe für einen ersten Vergleich des CPMs mit experimentellen Daten, Anastasia Reinl für erste Untersuchungen der RPEs auf Dumbbells, Theresa Reitz für ihre großartige Arbeit an Zellen in Labyrinthen und Georg Ladurner für die unendlich vielen Messungen der Zwei-Zell-Interaktion, die es jetzt nur zum Teil in diese Arbeit geschafft haben.

Dem gesamten Lehrstuhl Rädler mit seinen vielen Mitgliedern über die letzten Jahre: Madeleine, durch deren Vorlesung ich erst auf Biophysik gestoßen bin und deren super Betreuung in Bachelor- und Masterarbeit mich für eine Promotion in der Biophysik begeistert hat, Sonja für die unvergleichlichen Pilatesstunden, Alex G., die immer ein offenes Ohr und zwei hilfsbereite Hände hatte und allen Bürokollegen die das Büro über die Jahre immer zu einem Anker im stürmischen Laboralltag gemacht haben: Tobi für die IT Unterstützung, Bene für großen Spaß mit der Boss-Trafo und einen Gegenpol zur Ökobewegung, Matthias für die ausgezeichnete Büroleitung und den Image of the Month Kontest, Christoph für unendliche Ratschläge und manche Gaudi, Alexandra für mehr Gemütlichkeit und gute Laune, Judith für einen Ruhepol mit messerscharfem Blick, Miriam für lustige Pubquiz-Abende, Anita für mehr Power im Büro und Ordnung in der Zellkultur, Kilian für Gesellschaft wann auch immer man im Büro vorbeischneit, Julian für irrwitzige Gespräche beim Mittagessen und Johannes für einen netten Ratsch zwischendurch.

Gerlinde und Charlott, die dafür sorgen, dass das Labor überhaupt funktioniert.

Meinen fleißigen Korrekturlesern: Almond, Anita, Tobi, Matthias und Hanna.

Allen Freunden, die mich durch diese Zeit begleitet haben und die dafür gesorgt haben, dass auch der Spaß nicht zu kurz kommt: Anita und Basti, Tobi und Judith, David und Yingxin, Matthias und allen anderen.

Meiner Familie, die mich immer nach Kräften unterstützt hat und vor allem Almond, der die Arbeit mit seiner Kritik immer wieder verbessert hat und der ein steter Ruhepol an meiner Seite ist.